The effect of Mg^{2+} and Ni^{2+} on the kinetics and thermodynamics of ATP-binding, catalysis, and stability of *Klebsiella pneumoniae* nicotinate nucleotide adenylyltransferase

by

Reabetswe Maake

(1480907)

Dissertation

Submitted in fulfilment of the requirements for the degree

Master of Science

in

Molecular and Cell Biology

in the Faculty of Science, University of the Witwatersrand, Johannesburg, South Africa

Supervisor: Dr Ikechukwu A. Achilonu

June 2022

Declaration

I declare that this dissertation is my own, unaided work. It is being submitted for the Degree of Master of Science at the University of the Witwatersrand, Johannesburg. It has not been submitted before for any degree or examination at any other University.

.

Reabetswe Maake

Publications

In addition to my research studies, I contributed to two peer-reviewed publications listed below:

1. Jeje, Olamide; **Maake, Reabetswe**; van Deventer, Ruan; Esau, Veruschka; Iwuchukwu, Emmanuel Amarachi; Meyer, Vanessa; Khoza, Thandeka; Achilonu, Ikechukwu; Effect of Divalent Metal Ion on the Structure, Stability and Function of *Klebsiella pneumoniae* Nicotinate-Nucleotide Adenylyltransferase: Empirical and Computational Studies, ***International journal of molecular sciences***, 23(116), 2022 MDPI.

2. Daya, Tasvi; Jeje, Olamide; **Maake, Reabetswe**; Aloke, Chinyere; Khoza, Thandeka; Achilonu, Ikechukwu; Expression, Purification, and Biophysical Characterization of *Klebsiella Pneumoniae* Nicotinate Nucleotide Adenylyltransferase: ***The Protein Journal*** 16-Jan 2022, Springer

Abstract

Hospital-acquired infections (HAIs) have become a burden to the healthcare system with a global impact of 19.1% and 7.5% in developing and developed nations, respectively. Bacteria associated with HAIs are referred to as ESKAPE pathogens. They are multidrug resistant and *Klebsiella pneumoniae* is one of those pathogens. The bacterium has also shown to inherit heat resistance from a heat shock protein. Thus, becoming a double threat. The therapeutic approach to combat HAIs would be to target NAD^+ synthesis because it is vital in the survival of prokaryotes. The focus would be to inhibit nicotinate nucleotide adenylyltransferase (NNAT) which is essential in NAD^+ formation. Inhibiting the enzyme would decrease the NAD^+ pool and eliminate the bacterium. NNATs are metal binding proteins and have selective preference for metal ions. Mg^{2+} has been the preferred metal ion and in some species Ni^{2+} being the favoured metal ion. The aim was to assess the influence of Mg^{2+} or Ni^{2+} on the structure, kinetics and ATP binding. The objectives are to express and purify *Kp*NNAT with a pET expression system and nickel affinity chromatography, followed by functional characterisation with an ADH-mediated dual assay. Structural characterisation with far-UV circular dichroism (cd), fluorescence spectroscopy and size exclusion-high performance liquid chromatography. Thermostability with far-UV cd and thermal shift assay with a SYPRO orange dye. Isothermal titration calorimetry to assess ATP binding and obtain kinetics parameters. The pET expression system and nickel affinity chromatography were effective in expressing and purifying *Kp*NNAT. The protein has 0.09 $\mu mole \cdot min^{-1} \cdot mg^{-1}$ increase in pseudo specific activity in the presence of Mg^{2+} and maximal activity compared to Ni^{2+}. Far-UV cd suggest that the protein is α-helical in the presence of Mg^{2+} while there is observed loss of α-helical content in the presence of Ni^{2+}. The protein is thermally stable in the presence of Mg^{2+} as opposed to Ni^{2+}. The protein adopts a compact conformation in the presence of Mg^{2+}. Fluorescence studies suggest that Mg^{2+} creates a polar environment in the hydrophobic pocket for ATP binding. While a hydrophobic environment is promoted in the presence of Ni^{2+}. ATP binding is weak in the presence of Mg^{2+} and no binding is observed in the presence of Ni^{2+}. NMN binds with a low affinity in the presence of Mg^{2+}, thus suggesting that it is not the preferred mononucleotide substrate. Furthermore, in the absence of cations and presence of Ni^{2+} the reaction was endothermic and in the presence of Mg^{2+} the reaction is exothermic, entropically favourable, and spontaneous. To conclude, the difference in the activity, structure and binding in the presence of metal ion suggests that Mg^{2+} is the preferred divalent metal ion for

*Kp*NNAT catalysis. Therefore, this study contributes to better understanding the enzyme to subsequently improve administered antibiotics for HAIs.

Acknowledgements

I would like to thank my supervisor Dr Ikechukwu A. Achilonu for his incessant support, guidance and patience throughout my degree. Your contribution, and zest towards science continues to inspire me. The information that you have taught me in this field is invaluable and will aspire to transfer the knowledge as you have encouraged me to do so.

To the past and current members of the Protein-Structure Function Research Unit, most notably Aasiya, Blessing, Mpho, Neo, Olamide, Ruan and Verushka. I am grateful for all of the aid and wisdom that you have imparted to me. Dr Thulo for assisting me with ITC.

To the Department of Water and Sanitation for their financial support.

And a special thanks to my family and friends, I am grateful for the encouragement, love and support throughout this journey of my MSc. Your constant support was a driving factor as it inspired me to pursue my dreams.

Table of content

List of Figures

List of Tables

List of Abbreviations

ADH: Alcohol dehydrogenase

ANS: 8-Anilino-1-naphthalenesulfonic acid

APS: Ammonium persulfate

ATP: Adenosine triphosphate

CAUTI: Catheter associated urinary tract infection

CD: Circular dichroism

ClpK: Chaperone ATPase

CRBSI: Catheter related bloodstream infection

CVCs: Central venous catheters

$[E]_T$ is the total concentration of the active enzyme

E. coli: *Escherichia coli*

*Ec*NNAT: *E. coli* nicotinate nucleotide adenylyltransferase

EDTA: Ethylenediaminetetraacetic acid

ESBL: Extended-spectrum β-lactamase

ESKAPE: *Enterococcus faecium*, *Staphylococcus aureus*, *Klebsiella pneumoniae*, *Acinetobacter baumannii*, *Pseudomonas aeruginosa*, and *Enterobacter species*

$\Delta G°$ change in Gibbs free energy in standard conditions

$\Delta H°$ change in enthalpy in standard conditions

ΔH_{app} the apparent change in enthalpy

HAIs: Hospital-acquired infections

His: Histidine

*h*NNAT: *Human* nicotinate nucleotide adenylyltransferase

ICU: Intensive care unit

IDA: Iminodiacetic acid

IFE: Inner filter effect

IMAC: Immobilised metal affinity chromatography

IPTG: Isopropyl-β-D-thiogalactoside

ITC: Isothermal titration calorimetry

kDa: Kilodaltons

$K_{d:}$ Dissociation constant

K. pneumoniae: *Klebsiella pneumoniae*

*Kp*NNAT: *Klebsiella pneumoniae* nicotinate nucleotide adenylyltransferase

K_m which is the Michaelis-Menten constant

k_2 is k_{cat} it is the rate constant

mant-ATP: 2'/3'-O-(N-Methylanthraniloyl) adenosine-5'-triphosphate

MDR: Multidrug resistance

MRSA: Methicillin resistant *S. aureus*

n is the stoichiometry

NaAD: Nicotinic acid adenine dinucleotide

NaMN: Nicotinic acid mononucleotide

NAD^+: Nicotinamide adenine dinucleotide

NadD: Nicotinate nucleotide adenylyltransferase

NadE: NAD synthase

NADH: Nicotinamide adenine dinucleotide hydrogen

NadR: NAD^+ biosynthesis/regulator protein

NMN: Nicotinamide mononucleotide

NNAT: Nicotinate nucleotide adenylyltransferase

NTA: Nitrilotriacetic acid

OD_{600}: Optical density at 600 nm

ORF: Open reading frame

PCR: Polymerase chain reaction

PDB: Protein Data Bank

pET: Plasmid for expression by T7 RNA polymerase

pI: Isoelectric point

R is the gas constant 8.3145 $J \cdot mol^{-1} \cdot K^{-1}$

R_f: Relative migration distance

RMSD: Root means square deviation

rpm: Revolution per minute

$[S]_t$ is the free substrate concentration

$\Delta S°$ change in entropy in standard conditions

SDS-PAGE: Sodium dodecyl sulfate-polyacrylamide gel electrophoresis

SE-HPLC: Size exclusion-high performance liquid chromatography

SSI: Surgical site infection

T the absolute temperature in K

T_m: Melting temperature

TCEP: Tris(2-carboxyethyl) phosphine

TEMED: N, N, N'N'-tetramethylethylethylenediamine

TSA: Thermal shift assay

UV-vis: Ultraviolet-visible

$v_{max:}$ Maximum velocity

VAP: Ventilator associated pneumonia

VRE: Vancomycin resistant *E. faecium*

$d[P]/dt$ is the rate of reaction

$(dQ_{reaction})/dt)$ is the rate of heat production over time

θ is ellipticity

[θ] mean residue ellipticity

The amino acids were named in accordance with the IUPAC one and three letter codes.

Chapter 1

Introduction

1.1. Problem Statement

Nosocomial infections or hospital-acquired infections (HAIs) have become an economic and healthcare affliction. The economic impact from HAIs results from a prolonged stay in a healthcare facility, subsequently causing elevated medical costs (Bagheri-Nejad *et al.*, 2011). HAIs are absent before a patient's admission (Revelas, 2012) and are apparent 48 hours after a patient's admittance to a healthcare facility (Monegro *et al.*, 2020). Medical instruments such as ventilators or catheters harbour pathogens linked to HAIs (Khan *et al.*, 2017). Pathogens associated with HAIs include bacteria, fungal parasites, and viruses, with bacteria being the predominant causative agent of HAIs. The exact global prevalence of HAIs is unknown, but estimates of 5.7-19.1% and 5.7-7.5% in developing and developed countries, respectively, have been recorded (Saleem *et al.*, 2022). In sub-Sahara Africa, the prevalence was 28-45.8% (Bagheri Nejad *et al.*, 2011; Rothe *et al.*, 2013). Intensive care units (ICU) and neonates are prone to HAIs. In 291 459 ICU patients, 19.5% had HAI (Stiller *et al.*, 2017). HAIs account for 40% of neonates' mortalities in developing countries (Zaidi *et al.*, 2005).

The excessive administration of antibiotics to healthcare patients has produced multidrug-resistant (MDR) pathogens. Rice (2008) associated MDR pathogens with HAIs and dubbed them ESKAPE pathogens. ESKAPE is an acronym for *Enterococcus faecium*, *Staphylococcus aureus*, *Klebsiella pneumoniae*, *Acinetobacter baumannii*, *Pseudomonas aeruginosa* and *Enterobacter species* (Santajit and Indrawattana, 2016). It was reported that the ESKAPE pathogens contribute to 75% of HAIs (El-Mahallawy *et al.*, 2016). These pathogens are known to evade the biocidal activity of antibiotics, thus making them difficult to combat. *Enterococcus faecium* (*E. faecium*) and *Staphylococcus aureus* (*S. aureus*) are both gram-positive and have acquired resistance for vancomycin (VRE) and methicillin (MRSA), respectively (Hassoun *et al.*, 2017; Wang *et al.*, 2013). *Klebsiella pneumoniae* (*K. pneumoniae*) is a gram-negative bacterium. This bacterium causes ventilator-associated pneumonia, which occurs within two days following the trachea

infection and is common in ICU patients (Chi *et al.*, 2012; Hunter, 2006). Ventilator-associated pneumonia is responsible for 86 % of HAIs pneumonia (Koenig and Truwit, 2006). *K. pneumoniae* is resistant to β-lactam antibiotics, fluoroquinolones and aminoglycosides (Ferreira *et al.*, 2019). Carbapenems form part of the β-lactam antibiotics and are the first response mode to *K. pneumoniae* extended-spectrum β-lactamase (ESBL) (Ferreira *et al.*, 2019). Resistance to carbapenems by *K. pneumoniae* ESBL has been reported (Nordmann *et al.*, 2009).

ClpK is a novel chaperone protein discovered in a heat-resistant *K. pneumoniae* strain (Bojer *et al.*, 2013). This heat-resistant strain is thought to have acquired the clpk gene that encodes for ClpK (Bojer *et al*., 2010). It was discovered that the source of this heat-resistant strain is in its endoscopes, and it was also related to nosocomial infections (Jørgensen *et al.*, 2016). Hence, resulting in the emergence of a novel *K. pneumoniae* strain that is not only multidrug-resistant but also heat-resistant.

1.2. Rationale

The rise in HAIs in conjunction with the excessive administration of antibiotics has resulted in the rise of multidrug-resistant (MDR) pathogenic bacteria. The increase in multidrug-resistant pathogenic bacteria has caused a global burden to the healthcare system. Approaches that have been designed to combat MDR bacteria include antibiotics, combination therapy, bacteriocins, phage or bacteriophage therapy and nano therapy. Combination therapy which describes the use of two or more antibiotics, has been suggested as an approach to targeting Gram-negative MDR bacteria (Tamma *et al.*, 2012). Bacteriocins are an alternative to antibiotics. They are peptides or proteins produced by a strain of bacteria to inhibit the growth of a closely related strain of bacteria; they include colicins and microcins (Soltani *et al.*, 2021; Vivas *et al.*, 2019). A bacteriophage is a virus that infects a bacterium. Phage therapy involves using bacteriophages specific to a strain of bacteria, and they attack bacteria by cell lysis (Lin *et al.*, 2017). Nanoparticles are small materials, less than 1000 nm in size, with chemical and physical properties that are appealing for medical use (Medina *et al.*, 2007). Nanoparticles include silver and gold and are beneficial as they have been shown to enhance the function of antibiotics or bacteriocin and have bactericidal properties (Vivas *et al.*, 2019). Antibiotics have proven to effectively combat MDR bacteria, but the issue is the misuse or overuse of antibiotics, which has resulted in increased resistance to antibiotics. To tackle the raised issue, novel classes of antibiotics have been developed. Still, the problem is that the new classes of antibiotics that have been designed recently have proven to be ineffective for Gram-negative bacteria (Worthington and Melander, 2013). A novel therapeutic approach to

combat multi-drug and heat resistant *K. pneumoniae* caused by *K. pneumoniae* would target the biosynthesis of nicotinamide adenine dinucleotide (NAD^+). The reason for studying NAD^+ is that it is fundamental in the survival of prokaryotes (Santos *et al.*, 2020).

NAD^+ is a cofactor, including its reduced form NADH. It provides a fundamental component in the transfer of electrons from one reduction-oxidation reaction to the other and thus creates a balance in intracellular reduction-oxidation (Heux *et al.*, 2006; Nikiforov *et al.*, 2015; Rizzi and Schindelin, 2002). NAD^+ can be synthesised through two pathways *de novo* and the salvage pathway. The *de novo* pathway synthesises NAD^+ using the amino acids aspartate and tryptophan as precursors, and the salvage pathway uses substrates nicotinic acid mononucleotide (NaMN) or nicotinamide mononucleotide (NMN) (Gazzaniga *et al.*, 2009; Stancek *et al.*, 2005b). The salvage pathway requires the enzyme nicotinate nucleotide adenylyltransferase (NNAT) to convert the substrate NaMN/NMN to nicotinic acid adenine dinucleotide (NaAD)/NAD^+ (Stancek *et al.*, 2005b; Zhang *et al.*, 2002). It was shown that some gram-negative bacteria lack essential genes involved in the formation of NAD^+ through the *de novo* pathway, thus rendering the salvage pathway fundamental in the synthesis of NAD^+ (Roussin and Salcedo, 2021).

NNAT is an enzyme that produces NAD^+ or NaAD and an inorganic pyrophosphate from the transfer of an adenylyl group from adenosine triphosphate (ATP) to NMN or NaMN (Zhang *et al.*, 2002). NNAT can be found in eukaryotes and prokaryotes and is part of the nucleotidyltransferases (Magni *et al.*, 2004). NNAT serves as a putative drug target as essential in NAD^+ formation. This makes it critical in cell survival. In conjunction with the active site, the quaternary structure of prokaryotic NNAT is vastly different from human NNAT (Hughes *et al.*, 1983; Magni *et al.*, 2004). Bacteria favour NaMN as a substrate, and humans have an equal affinity for NaMN and NMN as a substrate (Zhang *et al.*, 2002). NNATs are metal-binding proteins. This sparks interest in understanding the influence of metal ions on the protein. Human NNAT exhibits a diverse specificity for different divalent metal ions. The isozyme forms of human NNAT are 1, 2, and 3. The isozyme forms 2 and 3 prefer Mg^{2+} as the divalent metal ion while 1 prefers Zn^{2+} as the metal ion (Sorci *et al.*, 2007). *E. coli* NAD^+ biosynthesis/regulator protein (NadR) is bifunctional and has NNAT activity. It was shown to increase activity when Ni^{2+} or Co^{2+} were used as divalent metal ions (Raffaelli *et al.*, 1999b). Extensive research on the influence of metal ions on NNAT has been done on human NNAT, but the same cannot be said about *K. pneumoniae*. The idea is to impede the function of NNAT, thus decreasing the NAD^+ pool and subsequently impeding the survival of the bacterium, *K. pneumoniae*.

To understand or use NNAT as a drug target, it is vital to express, purify, biophysically characterise, obtain thermostability information, thermodynamic parameters from ATP binding to the enzyme, and kinetic parameters all in the absence or presence of metal ions, Mg^{2+} or Ni^{2+}.

1.3. Aim and Objectives

The study aims to understand the influence of divalent metal ions, Mg^{2+} and Ni^{2+}, on the biophysical characterisation of *Kp*NNAT. Furthermore, to assess ATP binding to *Kp*NNAT and achieve a novel method of determining kinetic parameters by eliminating the ADH-mediated dual enzyme assay. This is achieved through empirical studies.

The following objectives were established to carry out the aim of the study:

- To overexpress *Kp*NNAT using the pET-28a expression system, purify the enzyme using immobilised metal affinity chromatography (IMAC), and assess the recombinant protein's purity using sodium dodecyl sulfate-polyacrylamide gel electrophoresis (SDS-PAGE).
- To assay the function of *Kp*NNAT with an ADH-mediated dual enzyme assay.
- To analyse the secondary, tertiary and quaternary structure of *Kp*NNAT using far-UV circular dichroism (CD) spectroscopy, fluorescence emission spectroscopy and size exclusion-high performance liquid chromatography (SE-HPLC).
- To gauge the thermal stability analysis using a combination of far-UV CD and thermal shift assay (TSA).
- To characterise the thermodynamics and kinetics of ATP utilisation of *Kp*NNAT using isothermal titration calorimetry (ITC) and subsequently obtain thermodynamic and kinetic parameters of the enzyme.

Chapter 2

Literature Review

2.1. Hospital-acquired infections

Hospital-acquired infections (HAIs) or nosocomial infections are infections that are absent at the time of admission of a patient, and the infection is displayed 48 hours after the admittance of a patient (Ducel *et al.*, 2002; Monegro *et al.*, 2020). The devastating outcome of HAIs on patients include morbidity, mortality and elevated healthcare costs due to a prolonged hospital stay (Worth *et al.*, 2009). It is estimated that the global impact of HAIs results in a prevalence rate of up to 15% of all hospitalised patients (Allegranzi *et al.*, 2011). In developed countries, the incidence rate of HAIs is 5%, while in developing countries, it was recorded to be 7.4% (Bagheri Nejad *et al.*, 2011; Scherbaum *et al.*, 2014). Intensive care units (ICU) and neonates are susceptible to these infections. It was reported that at least 50% of ICU in developed countries were infected with HAIs, and 4-56% of mortalities in neonates were a result of HAIs (Khan *et al.*, 2017; Scherbaum *et al.*, 2014). Ventilators and catheters are the source of these infections. HAIs are divided into catheter related bloodstream infection (CRBSI), catheter associated urinary tract infection (CAUTI), surgical site infection (SSI), and ventilator associated pneumonia (VAP) (Caselli *et al.*, 2018).

CRBSI is a bloodstream infection that originates from central venous catheters (CVCs) and are predominantly caused by gram-positive bacteria (Abd El-Hamid El-Kady *et al.*, 2021). They contribute up to 25% of mortalities due to HAIs (Maki *et al.*, 2006). CAUTI is caused by urinary catheters, Gram-negative bacteria and accounts for 40% of nosocomial infections (Maki and Tambyah, 2001; Perrin *et al.*, 2021). SSI are defined as infections that occur within 30 days following an operation and affect the operation site. They are the third leading cause of HAIs, following CAUTI. They attribute up to 16% of HAIs in hospitalised patients caused by *Staphylococcus aureus* (*S. aureus*) and *Enterococcus species* (Owens and Stoessel, 2008). VAP is common in ICU patients and results from pneumonia due to a patient's exposure to mechanical ventilation (Hunter, 2012). The infection appears 48 h following exposure to a ventilator (Papazian *et al.*, 2020). Gram-negative bacteria contribute to 60% of VAP, while *S. aureus* accounts for up

to 30% of VAP (Lobdell *et al.*, 2012). Microorganisms such as bacteria, fungal parasites and viruses cause HAIs, but bacteria are the primary causative agent. These bacteria encompass multidrug-resistant pathogens called ESKAPE pathogens.

2.2. ESKAPE pathogens

ESKAPE stands for *Enterococcus faecium*, *Staphylococcus aureus*, *Klebsiella pneumoniae*, *Acinetobacter baumannii*, *Pseudomonas aeruginosa* and *Enterobacter species*. ESKAPE was derived by Rice (2008) to describe pathogens that cause HAIs and are multidrug-resistant. MDR pathogens account for 15.5% of global HAIs (Mulani *et al.*, 2019). ESKAPE pathogens is a collective of gram-positive bacteria, *Enterococcus faecium* (*E. faecium*), *S. aureus* and gram-negative bacteria, *Klebsiella pneumoniae* (*K. pneumoniae*), *Acinetobacter baumannii* (*A. baumannii*), *Pseudomonas aeruginosa* (*P. aeruginosa*) and *Enterobacter species*.

In 1882, to isolate bacteria that caused pneumonia, Hans Christian Gram discovered a technique commonly referred to as gram staining (Bartholomew and Mittwer, 1952). The method employs several steps that included the fixation of a bacterial culture by heat onto a glass slide followed by the addition of the initial dye (crystal violet), then dye fixation with iodine, removal of the initial dye with a mixture of ethanol and acetone and finally the application of safranin, counterstain (Tripathi and Sapra, 2022). The technique categorises bacteria into two distinctive groups, gram-positive and gram-negative. Gram-positive are characterised by their thick cell wall formed from peptidoglycan. As a result, these bacteria take up the initial dye (crystal violet) and appear blue under a microscope (Sizar and Unakal, 2022). Gram-negative bacteria have a thin layer of peptidoglycan, and as a result, the bacterium cannot take up the initial stain. Instead, the counterstain is taken up; hence the bacterium appears pink under the microscope (Tripathi and Sapra, 2022). Figure 2.1 illustrates the ESKAPE pathogens depicted under a scanning electron microscope.

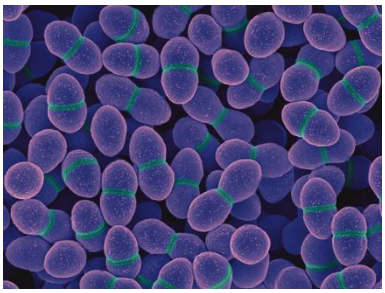

Enterococcus faecium

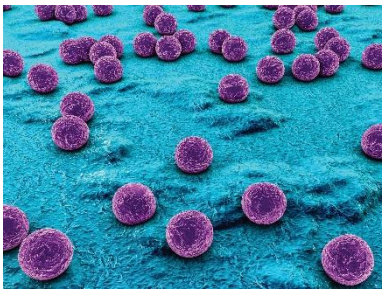

Staphylococcus aureus

Klebsiella pneumoniae

Acinetobacter baumannii

Pseudomonas aeruginosa

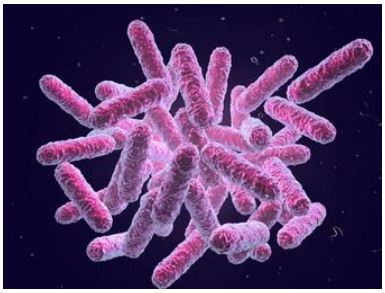

Enterobacter species

Figure 2.1. ESKAPE bacteria displayed under a scanning electron microscope.

E. faecium is the second gram-positive bacterium to cause HAIs, following *S. aureus*. The bacterium is resistant to vancomycin, thus producing vancomycin-resistant enterococci (VRE) strains (Miller *et al.*, 2014). *S. aureus* is resistant to methicillin. This has resulted in the emergence of methicillin-resistant *S. aureus* (MRSA), which have recently been shown to be resistant to vancomycin due to the transmission of vancomycin resistance from enterococci (Miller *et al.*, 2014).

Enterobacteriaceae is a family of gram-negative bacteria and includes ESKAPE pathogens, *K. pneumoniae* and *Enterobacter species* (Oliveira and Reygaert, 2022). Antibiotics administered for infections caused by *Enterobacteriaceae* include β-lactam extended-spectrum cephalosporins, carbapenems, fluoroquinolones and aminoglycosides (Teklu *et al.*, 2019). The consequence of the excessive administration of those antibiotics led to a new strain of *K. pneumoniae*, referred to as extended-spectrum β-lactamase (ESBL) *K. pneumoniae.* ESBL is an enzyme that confers bacteria resistance to cephalosporins (Teklu *et al.*, 2019). ESBL *K. pneumoniae* is fought by carbapenem antibiotics (Lee *et al.*, 2006). Carbapenem antibiotics are administered in excess to alleviate the resistance caused by cephalosporins; this has led to the formation of carbapenemases and the emergence of carbapenem-resistant *Klebsiella pneumoniae* strains. (Nordmann *et al.*, 2009).

2.3. Antibiotics and Antibiotic resistance

β-lactam antibiotics contain a β-lactam ring (Zeng and Lin, 2013). The mode of action by β-lactam is to prevent peptidoglycan synthesis, especially in the final step of peptidoglycan catalysed by transpeptidase. It does so by adding an acyl group to transpeptidase, which is involved in the cross-linking of peptides required for peptidoglycan formation (Pandey and Cascella, 2022). The outcome of β-lactam antibiotics leads to cell lysis. Antibiotic resistance is caused by β-lactamase production. β-lactamase functions by hydrolysing the β-lactam ring, thus neutralising the antibiotic's effect (Bush, 2018).

2.4. Heat resistance in *K. pneumoniae*

Clp ATPase may play a role in transferring heat resistance to *K. pneumoniae,* thus introducing heat as a problem in eliminating these multi-drug resistant pathogens (Bojer *et al.*, 2011). Clp ATPase is a family of chaperones that have a role in proteolysis (Hoskins *et al.*, 2001). They assist bacteria in responding to stressful environments. Gram-negative bacteria contain four types of Clp proteins: ClpA, ClpB, ClpP and ClpX, and their activities are well known in *Escherichia coli* (Bojer *et al.*, 2013). ClpP forms the central proteolytic hub that complexes with Clp A or Clp X and are the chaperones that perform proteolytic activities and the unfolding of proteins (Ortega *et al.*, 2004). ClpB does not complex with ClpP; instead, it is involved in the protein disaggregation (Parsell *et al.*, 1994). ClpK is a new chaperone protein isolated from a heat resistant *K. pneumoniae* (Bojer *et al.*, 2013). This heat-resistant strain is thought to have acquired the clpk gene that encodes for ClpK (Bojer *et al.*, 2010). It was shown by another study that the source of this heat resistant strain of *K. pneumoniae* was isolated in endoscopes and linked to nosocomial infections

(Jørgensen *et al.*, 2016). This has introduced a new strain of *K. pneumoniae* that may not only be multidrug-resistant but heat-resistant.

2.5. NAD^+ biosynthesis and biological role

Nicotinamide adenine dinucleotide (NAD^+) is a cofactor with its reduced form NADH. It functions to transfer electrons from one reduction-oxidation reaction to the other. This creates a balance in intracellular reduction-oxidation (Heux *et al.*, 2006; Nikiforov *et al.*, 2015; Rizzi and Schindelin, 2002). The reduction-oxidation balance allows the microorganism or an individual to grow and metabolise (Heux *et al.*, 2006). NAD^+ is a precursor of cyclic ADP-ribose, and it is involved in posttranslational modifications through ADP-ribosylation, catalysed by ADP-ribosyltransferase (Berger *et al.*, 2004; Ziegler, 2000). NAD^+ is involved in DNA repair through its affiliation with poly(ADP-ribose) polymerase and poly(ADP-ribosylation) (Herceg and Wang, 2001). In bacteria, NAD^+ interacts with DNA ligase and thus assists in DNA repair (Wilkinson *et al.*, 2001). NAD^+ can be biosynthesised through the *de novo* and salvage pathway. The *de novo* pathway synthesises NAD^+ using the amino acids aspartate and tryptophan as precursors while the salvage pathway uses substrates nicotinic acid mononucleotide (NaMN) or nicotinamide mononucleotide (NMN) (Gazzaniga *et al.*, 2009; Stancek *et al.*, 2005b). The salvage pathway requires the enzyme nicotinate nucleotide adenylyltransferase (NNAT) to convert the substrate NaMN/NMN to nicotinic acid adenine dinucleotide (NaAD)/NAD^+ and confers the enzyme pivotal in this pathway (Stancek *et al.*, 2005b; Zhang *et al.*, 2002). Figure 2.2 depicts a schematic of the *de novo* and salvage pathway for NAD^+ biosynthesis.

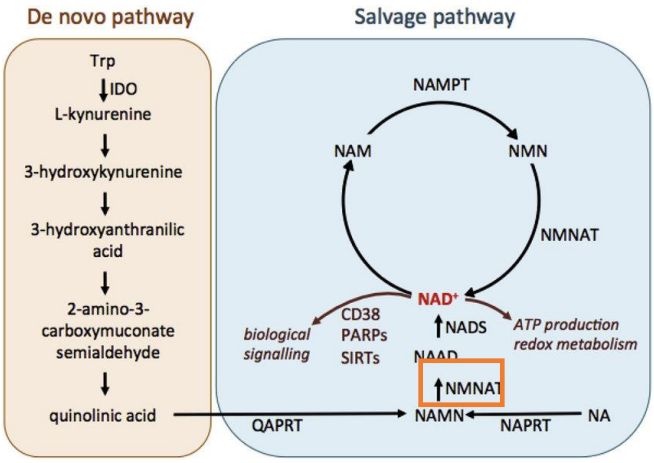

Figure 2.2. A schematic of the *de novo* and salvage pathway for the biosynthesis of NAD^+. The enzyme NNAT is depicted in an orange box (Nieborak and Schneider, 2018).

2.6. The enzyme NNAT

NNAT is encoded by the *nadD* gene and functions through a nucleophilic substitution by the 5'-phosphate of a mononucleotide (NMN or NaMN) on the α-phosphate of ATP thus yielding an inorganic pyrophosphate and a dinucleotide (NAD^+ or NaAD) (Bicknell *et al.*, 1982). Figure 2.3 shows the reaction catalysed by NNAT.

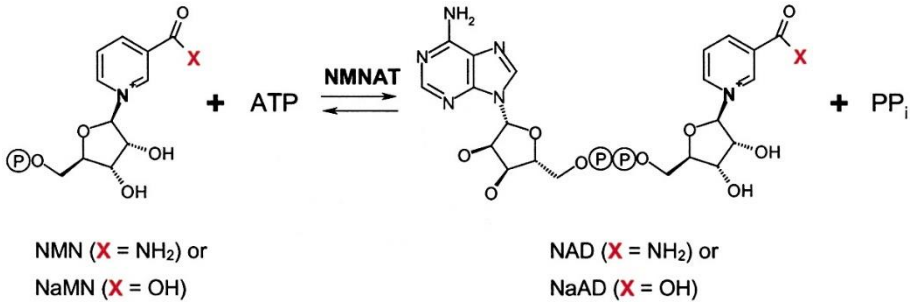

Figure 2.3. NNAT catalysed the reaction. NNAT facilitates the transfer of the adenylyl group from ATP to either NMN or NaMN to produce an inorganic pyrophosphate and either NAD^+ or NaAD, respectively (Zhang *et al.*, 2002).

The enzyme is classified as a transferase, specifically those that transfer a phosphorus-containing nucleotide group (nucleotidyltransferases), with an enzyme commission (EC) number of EC 2.7.7.1.8. The enzyme is crucial in the salvage pathway for the biosynthesis of NAD^+ in organisms and in prokaryotes the enzyme requires the salvage pathway due to the absence of genes that encompass the *de novo* pathway for the biosynthesis of NAD^+ (Hughes *et al.*, 1983; Roussin and Salcedo, 2021; Zhang *et al.*, 2002). This makes the enzyme pivotal in the survival of prokaryotes.

Nucleotidyltransferases are characterised by a Rossman-fold structure represented by alternating β-strands and α-helices. The fold constitutes a central β-sheet, formed by up to six hydrogen-bonded β-strands, surrounded by α-helices; this is depicted in Figure 2.4 (Saridakis and Pai, 2003). Furthermore, nucleotidyltransferases have a conserved ((T/H)XGH) motif (D'Angelo *et al.*, 2000). The presumed function of the motif is its involvement in ATP identification and binding (Lau *et al.*, 2009). Sequence alignment of members of the nucleotidyltransferases family has shown three conserved sequences in the active site, which are hG [GS], [DE]h[DE] and N-terminal h[DE]h, where h is a hydrophobic amino acid (Kuchta *et al.*, 2009). Figure 2.5 depicts the sequence alignment of members of the nucleotidyltransferases and the conserved sequences. The aspartate or glutamate function by directing divalent ions in the active site (Aravind and Koonin, 1999).

NNAT is omnipresent as it is found in both eukaryotes and prokaryotes. It is a globular protein that has an estimated molecular weight of 20-40 kDa, depending on the species (Lau *et al.*, 2009). *Ec*NNAT when complexed to NaAD had a predicted molecular weight of 25 kDa and it was suggested through gel filtration that the enzyme existed as a monomer (Zhang *et al.*, 2002). Figure 2.6 displays the predicted model of *Kp*NNAT.

In human NNAT, specifically the first isoform *h*NNAT-1, a hexameric state of the protein is observed. Furthermore, the first histidine amino acid in the conserved nucleotidyltransferases motif ((T/H)XGH) appears on prokaryotic and archaeal sequences but it is substituted by threonine in eukaryotes (Magni *et al.*, 2004). The third isoform of human NNAT *h*NNAT-3 is found in a tetrameric state and when bound to ligands there is minimal conformational change, relative to the apo state of the protein. This is different compared to *E. coli* which show a significant conformational change upon ligand binding (Zhang *et al.*, 2002).

NNATs exhibit differential substrate specificity across species. Bacteria prefer NaMN as opposed to NMN as a substrate, while human NNAT show preference for both NMN and NMN (D'Angelo *et al.*, 2000; Zhang *et al.*, 2002). The oxygens in the carboxylate group of NaMN interact with amides from tyrosine 118 and threonine 85 where one of the amino acids forms a hydrogen bond with water resulting in the interaction with amide in alanine 86 (Magni *et al.*, 2004). This results in an anion-binding pocket on the protein thus allowing the preference for NaMN in bacteria.

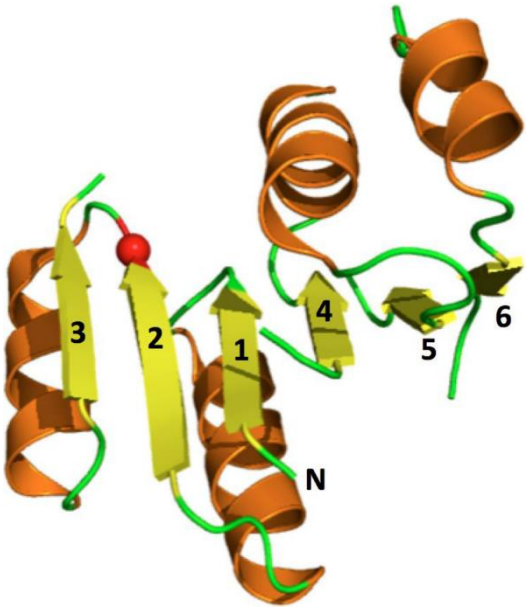

Figure 2.4. A schematic display of the Rossmann-fold. The central β-sheet (yellow), formed by six β-strands, surrounded by α-helices (orange) (Laurino *et al.*, 2016).

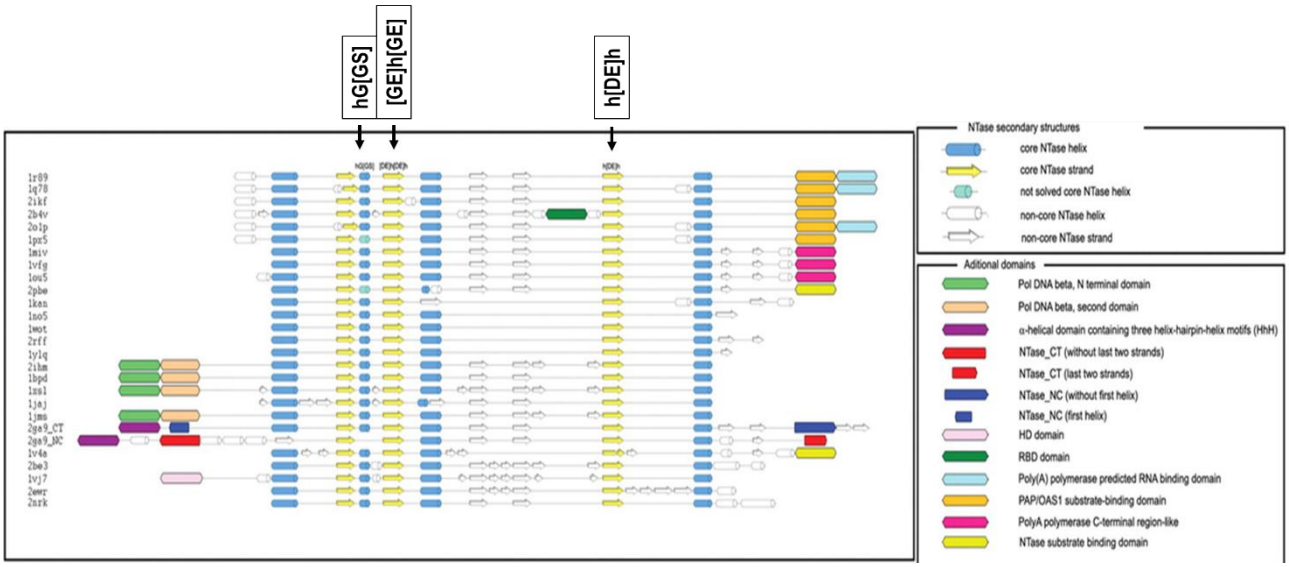

Figure 2.5. Sequence alignment of various members of nucleotidyltransferases. The alignment shows 3 conserved sequences in the active site which are hG [GS], [DE]h[DE] and h[DE]h and h represents the hydrophobic amino acids (Kuchta *et al.*, 2009).

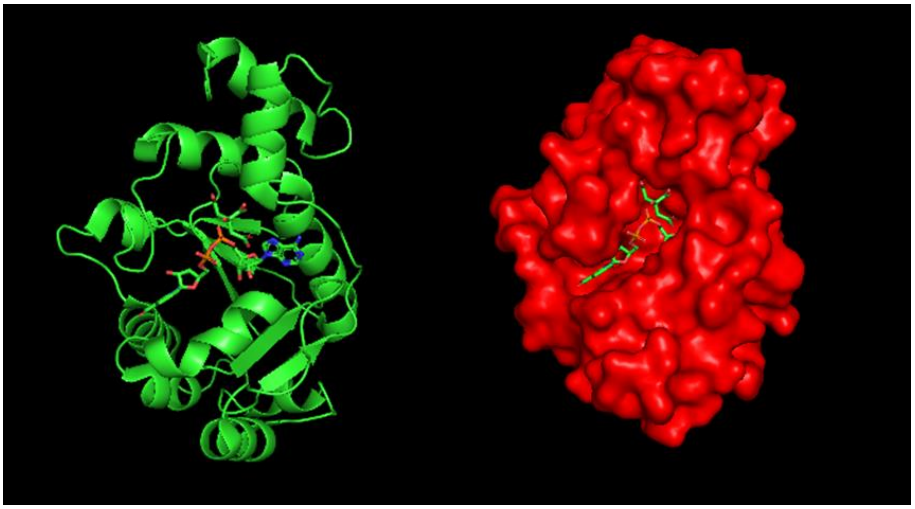

Figure 2.6. **A predicted model of *Kp*NNAT.** A ribbon structure (green) was used to illustrate 1K4M which is a predicted model from *Ec*NNAT. The surface structure (red) shows the binding site of ligand (NaAD) which is represented as sticks.

2.7. Influence of divalent metal ion on NNAT

Enzymes that are dependent on metal ions to function are referred to as metalloenzymes. Metal ions play a role in protein by either influencing the protein's structure or function (Chen *et al.*, 2019). They influence the protein's structure by affecting its folding (Laity *et al.*, 2001). Metal ions affect the protein's function as they influence the protein's active site and can be involved in biological processes such as transfer of electrons, catalysis, substrate binding, or recognition (Chen *et al.*, 2019). Metal ion bind to protein through the metal binding to a substrate to form a substrate-metal ion complex which then becomes the active substrate (Babor *et al.*, 2005). Magnesium is the preferred divalent metal ion to assist in the catalysis of NAD^+ synthesis (Raffaelli *et al.*, 2002). The isozyme of yeast NNAT favoured Ni^{2+} and Co^{2+} as the divalent metal ions (Magni *et al.*, 2004). *E. coli* NadR is bifunctional and has NNAT activity. It was shown to increase activity when Ni^{2+} or Co^{2+} were used as divalent metal ions (Raffaelli *et al.*, 1999b). NadM is an isozyme of NNAT and is found in archaea. It showed a preference for Ni^{2+} or Co^{2+} (Lau *et al.*, 2009). Human NNAT exhibits a diverse specificity for different divalent metal ions. The isozyme forms of human NNAT are 1, 2, and 3. The isozyme 1 prefers Zn^{2+} as the metal ion while isozyme 2 and 3 prefer Mg^{2+} as the divalent metal ion (Sorci *et al.*, 2007). Jeje *et al.* (2022) showed the importance of divalent metal ions enzyme activity of *E. faecium* and *K. pneumoniae* NNAT. It was observed that without metal ions there was no enzyme activity and elucidated that Mg^{2+} showed maximum enzyme activity followed by Ni^{2+} with a significant amount of activity.

2.8. Enzyme kinetics with isothermal titration calorimetry

Spectroscopic or chromatography techniques are used to obtain kinetic parameters by monitoring substrate depletion or product formation over time (Di Trani *et al.*, 2018). The problem with these techniques is that they may require substrate modification or multiple enzymes in an assay. The setback is that modified substrate may not have the same kinetic properties as the original substrate or dual enzyme assays may not yield true outcomes of the original reaction (Wang *et al.*, 2020b). The solution is to employ Isothermal titration calorimetry (ITC), which eliminates the chemical modification of a substrate or the use of dual enzyme assays as the technique measures heat signals produced in binding reactions and in real-time (Todd and Gomez, 2001).

The rate of heat production over time ($dQ_{reaction}/dt$) is directly proportional to the velocity of the reaction $d[P]/dt$. This relationship is depicted in Equation 1

$$\left(\frac{d[P]}{dt}\right)_t = \frac{\left(\frac{dQ_{reaction}}{dt}\right)_t}{\left(-V\Delta H_{app}\right)} \quad \textbf{(1)}$$

where V the volume of the reaction, and ΔH_{app} the change in enthalpy. Equation 2 then links the rate of the reaction from equation 1 with the kinetic parameters

$$\frac{\left(\frac{dQ_{reaction}}{dt}\right)_t}{\left(-V\Delta H_{app}\right)} = \frac{k_2[E_T][S]_t}{(K_m+[S]_t} \quad \textbf{(2)}$$

where k_2 is k_{cat} it is the rate constant, $[E]_T$ is the total concentration of the active enzyme, $[S]_t$ is the free substrate concentration, and K_m is the Michaelis-Menten constant. GraphPad Prism is then used to fit the data and obtain the kinetic parameters such as the v_{max} and the K_m.

The multiple injection method formally referred to as pseudo-first-order assay can obtain kinetic parameters from ITC. This technique was described by Todd and Gomez (2001). The experimental design requires low enzyme concentration, so that substrate depletion is minor. As a result, the rate of heat production stays constant, and the resulting isotherm resembles a sequence of steps with each injection (Wang *et al.*, 2020b). Figure 2.7 depicts an isotherm of the multiple injection method.

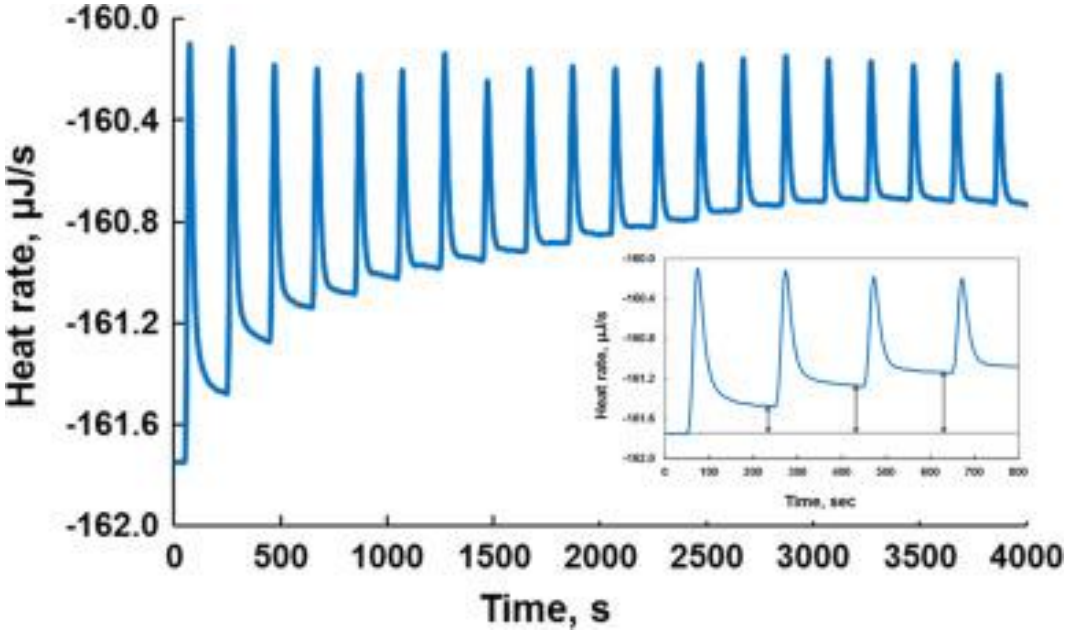

Figure 2.7. Isotherm depicting the successive injection substrate to protein and inset represents the first four injections. The arrows display the displacement of each step's rate of heat production relative to the initial baseline, indicated as a black horizontal line (Rana *et al.*, 2016).

Chapter 3

Expression and Purification of *Kp*NNAT

3.1. Introduction

The significance of recombinant protein expression is to yield copious amounts of the protein of interest. The principle of overexpression is to transfer a gene of interest into a self-replicating genetic structure vector (Prelich, 2012). It results in forming a vector construct, the combination of a vector and the gene of interest, which is then transformed into an expression host to produce a substantial amount of the protein of interest (Rosano and Ceccarelli, 2014). Primary studies that explored this technique focused on yeast transformation (Beggs, 1978; Hinnen *et al.*, 1978). Expression hosts are organisms that promote the expression of the recombinant protein. They include bacteria, yeast, plants and mammalian cells (Tripathi and Shrivastava, 2019). *E. coli* is commonly used as an expression host because it grows exponentially, as it was shown to have a doubling time of 20 min, under optimal conditions (Sezonov *et al.*, 2007). The plasmid for expression by the T7 RNA polymerase (pET) expression system is used to express the recombinant protein in *E. coli*. This system originates from the pBR322 plasmid and has a T7 promoter that binds to T7 RNA polymerase (Shilling *et al.*, 2020). The binding of T7 RNA polymerase to the T7 promoter drives the transcription of the desired gene. A chromosomal copy of the gene encoding for the T7 RNA polymerase is found in the expression host, and the transcription of this gene is under the control of the *lac*UV5 promoter (Mierendorf *et al.*, 1998). The pET expression system and the expression host contain a *lacI* gene that encodes for a Lac repressor protein (LacI) (Sørensen and Mortensen, 2005). The transcription of the T7 RNA polymerase gene is induced by isopropyl-β-D-thiogalactoside (IPTG). IPTG the *lac* operator and facilitates the release of LacI from the *lac* operator (Mierendorf *et al.*, 1998). The expression system contains an origin of replication (ori) which is the site of the initiation of replication by the plasmid and it influences the copy number of a plasmid (Baneyx, 1999). The copy number is the number of plasmid copies in a host cell. Selection markers form part of the expression system. They are pivotal in the selection of host that were successfully transformed with the vector-construct. These markers confer resistance to antibiotics (Goh and Good, 2008). Figure 3.1 depicts the pET-28a expression system, the nucleotide sequence of the gene encoding *Kp*NNAT, and the

amino acid sequence of the protein. The desired amino acid sequence of *Kp*NNAT used in this experiment has 219 amino acids, a molecular weight of ~25 kDa and a theoretical pI of 5.91. This information was obtained from the ProtParam ExPasy tool.

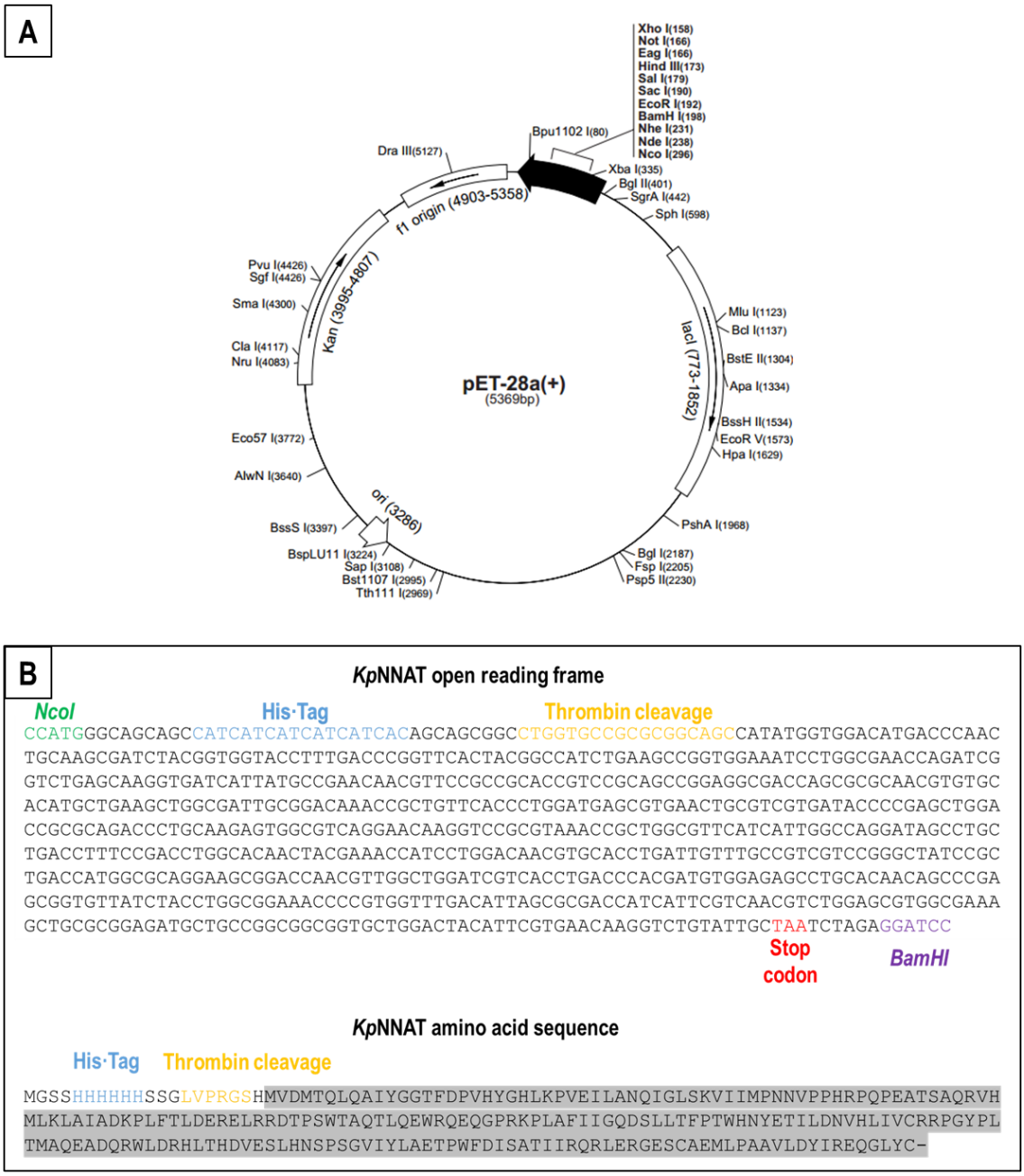

Figure 3.1. **A depiction of the vector construct of recombinant *Kp*NNAT and the pET-28a expression system. (**A) illustrates the map of the pET-28a expression system. It constitutes the restriction sites, ori, selection marker site and the *lacI* gene. The selection marker in the expression system is kanamycin. (B) illustrates the nucleotide sequence encoding *Kp*NNAT, which was inserted between the restriction sites, *NcoI* and *BamHI* and the resulting amino acid sequence. The protein sequence contains an N-terminal His·Tag, thrombin cleavage site and the target protein sequence depicted in grey.

3.1.1. Materials

All reagents, unless stated otherwise, were of analytical grade and purchased from Sigma-Aldrich (St Louis, MO, USA). The expression vector pET-28a-*Kp*NNAT was constructed by GenScript (Piscataway, NJ, USA).

3.1.2. Methods

3.1.2.1. Vector construction

The cDNA gene encoding *Kp*NNAT (Gene ID: 11846511) was cloned into a pET-28a expression vector. The open reading frame (ORF) sequence of *Kp*NNAT was inserted between the restriction sites, *Nco*I and *B*amHI, with the gene encoding an N-terminal His-tag. DNA sequencing was performed by Inqaba Biotec (Pretoria, RSA).

3.1.2.2. Expression

Competent *E. coli* T7 cells were transformed with the pET-28a-*Kp*NNAT construct. Following transformation, single colonies were selected from LB-agar, with the selective antibiotic 30 µg/mL of kanamycin and inoculated in 20 mL of 2×YT media containing 30 µg/mL of kanamycin. The concentration of kanamycin used was 30 µg/mL unless stated otherwise. The culture was incubated (37°C, 250 rpm for 16 h). From the culture, 1 mL of glycerol stocks were provided by Olamide Jeje (University of the Witwatersrand, Johannesburg, RSA). The overnight culture was made from 1 mL of the glycerol stock to 50 mL of 2×YT media containing kanamycin and incubated (37°C, 189 rpm for 16 h). The overnight culture was then diluted 1:50 with 2×YT media containing kanamycin, incubated (37°C, 210 rpm), until an OD_{600} of approximately 0.6 was reached. The culture was then subjected to cold shock and incubated at 4°C for 20 min. The expression of *Kp*NNAT was induced with 0.5 mM isopropyl-β-D-1-thiogalactopyranoside (IPTG), and the culture was incubated (30°C, 210 rpm, 6 h). The cells were harvested by centrifugation (5000 × g, 4°C for 15 min), and the pellet was resuspended with 20 mL of resuspension buffer [10 mM PBS, 0.02 % (*w/v)* NaN_3, pH 7.4] per 500 mL of culture. The resuspended pellet was stored at -80°C, overnight. The soluble fraction was harvested by first thawing the frozen cells then sonication (30 sec at 50 amplitudes) to facilitate cell lysis. The cell lysate was then centrifuged (18 000 × *g*, 4°C, 15 min). This process was performed to pellet cell debris and isolate the soluble cell fraction (supernatant).

3.2. Purification and SDS-PAGE Introduction

Immobilised metal affinity chromatography (IMAC) is a purification technique that separates proteins in solution based on histidine affinity to metal ions. The technique was discovered by Porath *et al.* (1975). The premise stems from the affinity between metal ions such as nickel, zinc, copper and cobalt to amino acids, histidine or cysteine (Block *et al.*, 2009). An IMAC column is designed in such a way that metal ions are immobilised to a resin through the process of chelation, and iminodiacetic acid (IDA) or nitrilotriacetic acid (NTA) are used as chelating agents (Glover and Tommos, 2019). When a histidine-tagged protein passes through a column, the imidazole group in histidine acts as an electron-pair donor under physiological conditions. It binds to the metal ion on the column (Block *et al.*, 2009). Hochuli *et al.* (1987) showed the effectiveness of using a Ni^{2+}-NTA adsorbent as opposed to the Ni^{2+}-IDA adsorbent proposed by Porath *et al.* (1975) because Ni^{2+} tends to leak. Ni^{2+} is commonly used because it effectively selects and interacts with proteins containing hexahistidine, thus making it efficient in protein purification (Valenti *et al.*, 2006). The elution of the desired protein can be achieved by lowering the buffer's pH, adding a competitive chelating agent such as ethylenediaminetetraacetic acid (EDTA) or the addition of free imidazole (Block *et al.*, 2009). Sodium dodecyl sulfate-polyacrylamide gel electrophoresis (SDS-PAGE) is a separation technique employed to separate macromolecules based on molecular weight. SDS is an anionic detergent used to denature protein by disrupting non-covalent bonds (Nowakowski *et al.*, 2014). It binds to proteins through a ratio of 1 SDS molecule per 2 amino acids and thus confers the protein with an overall negative net charge (Nowakowski *et al.*, 2014; Reynolds and Tanford, 1970). This allows for proteins to migrate to the anode in an electric field. Furthermore, reducing agents such as β-mercaptoethanol is used to disrupt disulfide bonds between cysteine residues in proteins (Shapiro and Maizel, 1969). This is done to further denature the protein. A discontinuous buffer system is used to separate proteins, depicted in Figure 3.2. The separating gel buffer and the stacking gel buffer constitutes of Tris-HCl at pH 8.8 and 6.8, respectively. The running gel buffer constitutes of Tris-HCl and glycine at pH 8.3. This system allows for the sandwiching of protein between Cl^- and glycine in the stacking gel before the protein enters the separating gel buffer (Davis, 1964; Ornstein, 1964). This system improves the resolution the samples.

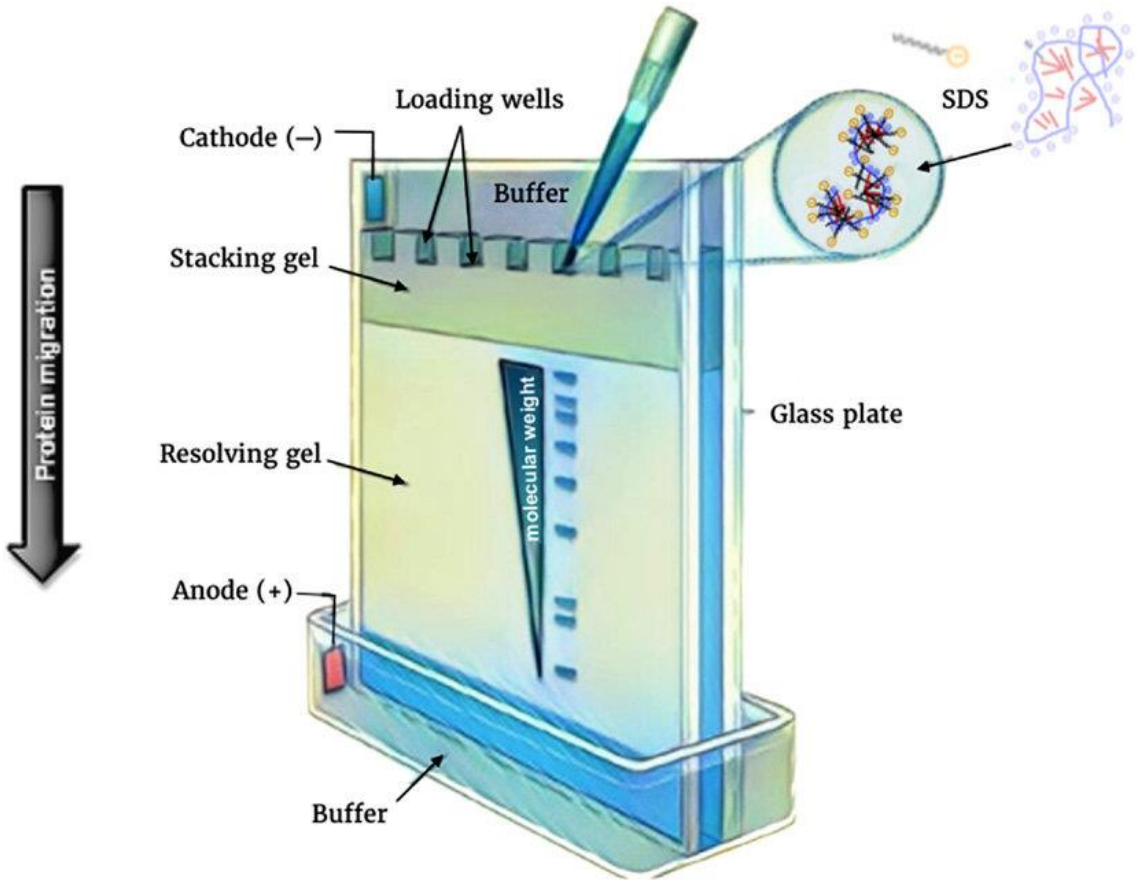

Figure 3.2. An illustration of a discontinuous SDS-PAGE system. The protein is loaded into a well, sandwiched in the stacking gel. Once stacked, it enters the resolving or separating gel. It migrates towards the anode and according to its molecular weight (Wangler and Bellen, 2017).

3.2.1. Purification of *Kp*NNAT

Immobilised metal affinity chromatography (IMAC) was employed to purify *Kp*NNAT, which exhibits the N-terminal His-tag on the vector construct. A BioLogic LP Low-Pressure Liquid Chromatography System (Bio-Rad, CA, USA) was used for purification. Approximately 8 mL of IMAC Sepharose 6 Fast Flow resin (GE Healthcare, Chicago, Illinois, USA) was added to an Econo-Column Chromatography column, 1.5 × 10 cm (Bio-Rad, CA, USA). The column was charged with 0.1 M $NiSO_4$ and equilibrated with 10 column volumes of equilibration buffer [10 mM PBS, 0.02 % (*w/v)* NaN_3, 25 mM imidazole, pH 7.2]. The flow rate of 4 mL/min was used unless stated otherwise. The supernatant was passed through the column followed by the equilibration buffer containing 0.01 % (*v/v*) Tween-20, then the wash buffer. The wash steps were necessary to minimise non-specifically bound proteins to the column. To displace the His-tagged *Kp*NNAT from the IMAC column, gradient elution was performed using the elution buffer [10

mM PBS, 0.02 % (*w/v*) NaN_3, 500 mM imidazole, pH 7.2]. Eluted fractions were collected by the Bio-Rad Model 2110 Fraction Collector (Bio-Rad, CA, USA) at a flow rate of 1 mL/min.

3.2.2. SDS-PAGE

The purity of the collected protein was analysed with a discontinuous glycine-SDS-PAGE (Laemmli, 1970). The gel was prepared using 12.5% (*w/v*) separating gel buffer and a 4% (*w/v*) stacking gel buffer depicted in table 2.1. The expression samples were prepared by collecting 100 µL of supernatant and pellet subjected to several wash steps. It entailed the pellet resuspension with 1 mL of MilliQ water followed by sonication (30 sec at 50 amplitudes) then centrifugation (13 000 × *g*, 20°C, 5 min). This wash step was performed three times. A 100 µL of the flowthrough, wash steps, and 4 elution fractions were collected. The expression and purification samples were diluted in a 1:1 ratio of reducing sample buffer [125 mM Tris-HCl, 4% (*w/v*) SDS, 20% (*v/v*) glycerol, 10% (*v/v*) β-mercaptoethanol, pH 6.8]. The samples were then incubated (100°C, 5 min) to denature the protein for SDS-PAGE. A total of 5 µL of the sample was loaded to each well, except for the molecular weight marker, BLUeye Prestained Protein Ladder (Sigma-Aldrich, St Louis, MO, USA), which was 2 µL. The gel was placed in a Mini-Protean Tetra cell (Bio-Rad, CA, USA) covered with tank buffer [250 mM Tris-HCl, 192 mM glycine, 0.1% (*w/v*) SDS, pH 8.3] and ran (160 V, 35 min). The gel was then stained with Coomassie stain [0.1% (*w/v*) Coomassie dye, in a 1:5:4 (*v/v/v*) ratio of acetic acid, methanol, water] for 2 h then destained with destaining solution [1:5:4 (*v/v/v*) acetic acid, methanol, water] overnight. The estimated molecular weight of the protein was determined by plotting a linear curve of the logarithm of the known molecular weights of the standards against the relative migration distance (R_f). The R_f values were obtained by using equation 3

$$R_f = \frac{Distance\ migration\ of\ the\ protein}{Distance\ migration\ of\ the\ dye\ front}. \quad \textbf{(3)}$$

Table 5. 3.1. A procedure on how to prepare 12.5% (*w*/v) separating gel and 4% (*w*/v) stacking gel.

	Separating gel	Stacking gel
	12.5%	4%
Monomer solution [30% (*w/v*) acrylamide, 0.8% (*w/v*) bis-acrylamide]	6.25 mL	940 µL
Separating gel [1.5 M Tris-HCl, pH 8.8]	3.75 mL	-
Stacking gel [500 mM Tris-HCl, pH 6.8]	-	1.75 mL
10% (*w/v*) SDS	150 µL	70 µL
Distilled water	4.75 mL	4.30 mL
10% (*w/v*) Ammonium persulfate (APS)	50 µL	35 µL
N,N,N'N'-tetramethylethylethylenediamine (TEMED)	7.50 µL	15 µL

3.3. Ultraviolet-visible (UV-vis) spectroscopy introduction

UV-vis spectroscopy is employed to measure the absorption of light by an analyte. The near-UV ranges from 150-400 nm, while visible light is from 400-800 nm (Schmid, 2001). It functions by measuring the intensity of light that has passed through an analyte (I) in relation to light that has passed through a blank (I_0). This relation is referred to as transmission; refer to equation 4

$$Transmission = \frac{I}{I_0} \quad \textbf{(4)}$$

and from the transmission, the absorbance (A) of light can be obtained. This relationship is depicted in equation 5

$$Absorbance = -\log T \quad \textbf{(5)}$$

where T is the transmission of light. The amount of light absorbed by an analyte is unique because it is dependent on its properties.

The application of UV-vis spectroscopy is to determine protein concentration (C) by applying the Beer-Lambert law, refer to equation 6, which states that the relationship between absorbance and concentration is directly proportional

$$A = C \times \varepsilon \times l \quad \textbf{(6)}$$

where Ɛ is the molar extinction coefficient, and *l* is the cuvette's path length. The molar extinction coefficient ($M^{-1} \cdot cm^{-1}$) reflects the ability of a substance to absorb light at a specific wavelength. The path length is measured in cm and represents the width or thickness of a cuvette. From this law, the protein concentration can be determined when the other parameters in equation 3 are known. Another function of UV-vis spectroscopy is to confirm whether the protein was isolated. This is done by analysing the absorbance of light by the protein at a range of wavelengths (250-600 nm) to generate an absorbance spectrum or by monitoring the reaction that the enzyme catalyses. The aromatic amino acid side chains such as phenylalanine, tryptophan and tyrosine contribute to the protein's ability to absorb UV light (Schmid, 2001). Tryptophan, tyrosine and phenylalanine absorb light at 280, 275 and 257 nm, respectively (Prasad *et al.*, 2017).

3.3.1. Elution profile, Protein concentration determination and UV-absorption spectrum

UV scan and protein concentration determination

A total of 30 of 1 mL elution fractions were collected and used to produce an elution profile. The NanoDrop (ThermoFisher Scientific, Waltham, MA, USA) was loaded with 2 µL of eluate. The absorbance was measured at 280 nm and corrected for light scattering caused by aggregation recorded at 340 nm. The elution profile was pivotal in identifying the elution fractions that had contained pure protein. Those fractions were pooled to create a concentrated protein sample used for subsequent analyses. A 1:20 dilution of protein to buffer [10 mM PBS, 0.02% (*w/v*) NaN_3, pH 7.2] was used to determine the concentration of the protein, depicted in Figure 3.3. The dilution series was used to produce a standard curve of the $A_{280\text{-}340}$ against the dilution factor.

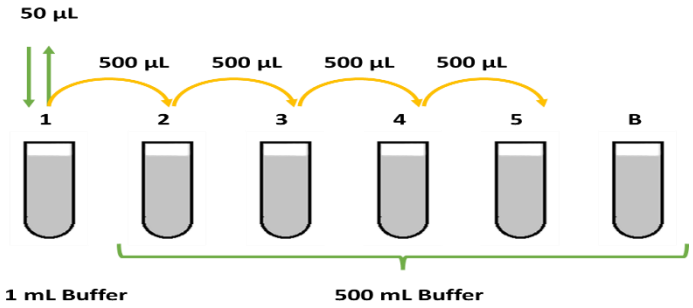

Figure 3.3. A dilution series, depicting the preparation of protein for concentration determination. Tube B represents the blank which was elution buffer.

The absorbance for each sample was measured with the Jasco V-630 spectrophotometer (Jasco, UK). The wavelengths were set at 280 nm and 340 nm. A total of 3 accumulations were taken.

The concentration was determined by substituting a molar extinction coefficient of 38 055 $M^{-1} \cdot cm^{-1}$, and the absorbance measurements observed in equation 7

$$C = \frac{A}{\varepsilon}. \quad \textbf{(7)}$$

The Jasco V-630 spectrophotometer (Jasco, UK) was employed for the UV scan. The sample was prepared by diluting 100 µL of protein to 400 µL of elution buffer, and the blank used was the elution buffer. A scanning speed of 100 nm/min, a data pitch of 0.5 min and a photometric mode of absorbance were used. The spectrum was measured from 240-380 nm, and three accumulations were taken.

3.4. Results

3.4.1. Expression and Purification

The recombinant *Kp*NNAT was expressed with a pET-28a expression system in T7 *E. coli* cells. The expression was induced with 0.5 mM IPTG and carried out for 6 hours at 30°C. The expression system employed had an N-terminal histidine tag which was fundamental in the purification of the protein. Following expression, the cells were subjected to sonication and centrifugation to prepare for purification. The resultants of the preparation step were an insoluble fraction (pellet) and a soluble fraction (supernatant). Ni^{2+}-IMAC served as the purification technique where supernatant was passed through the column.

Furthermore, several wash steps were implemented to remove unbound or weakly bound protein. Gradient elution was achieved by increasing the concentration of imidazole to compete with the histidine tag on the recombinant protein. Elution fractions were collected to produce an elution profile (Figure 3.4). A 12% (*w/v*) glycine SDS-PAGE gel was prepared to analyse the quality of the purification (Figure 3.5A). The samples from purification such as the pellet, supernatant, wash steps and eluate were collected, and 5 µL of each sample was loaded onto the gel. The technique showed that recombinant *Kp*NNAT was expressed and purified because of the single thick ~25 kDa band depicted in an orange box on the gel. The predicted molecular weight of the protein using the calibration curve (Figure 3.5B) was estimated to be ~22.7 kDa.

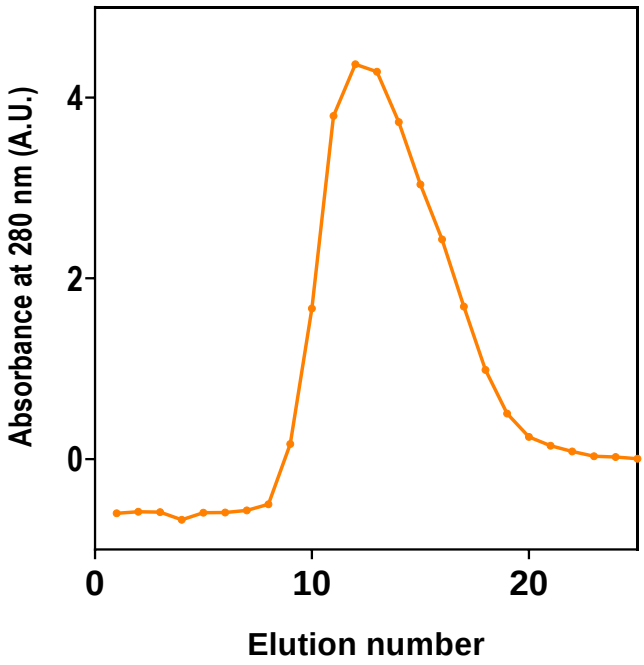

Figure 3.4. Elution profile of KpNNAT following purification with Ni^{2+}-IMAC. Gradient elution was performed with 25 fractions collected at a 1 mL/min flow rate. The absorbance at 280 nm against the elution number was plotted to obtain the fraction with the most concentrated protein and the fraction collected for subsequent characterisation studies, including SDS-PAGE. This correlation between absorbance and concentration stems from the Beer-Lambert equation, which states the direct proportionality between absorbance and concentration. From the relationship between the absorbance and concentration, the concentrated fraction is depicted as the elution profile's peak (elution 13).

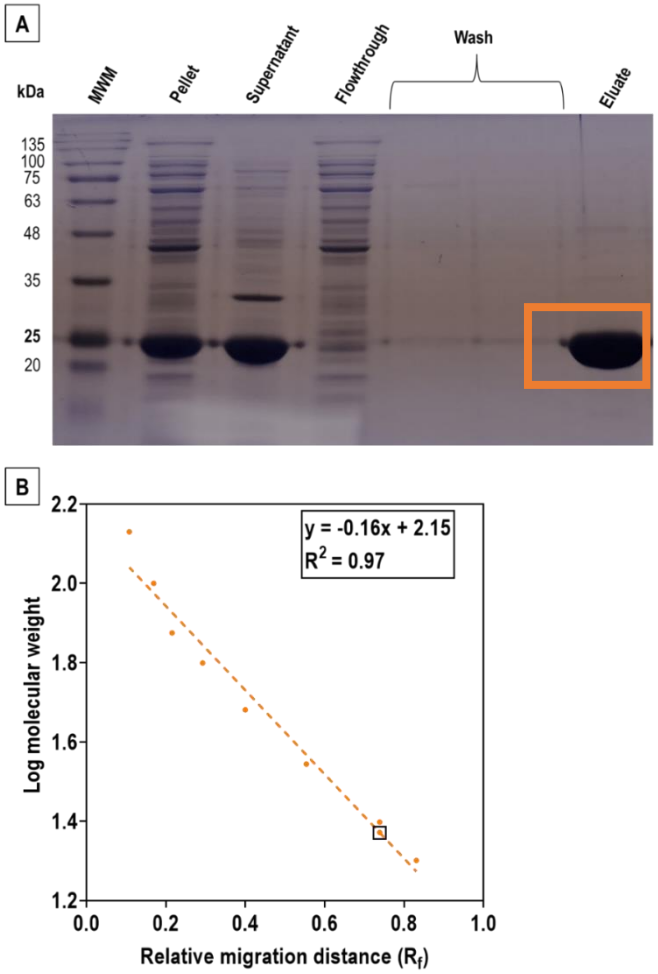

Figure 3.5. SDS-PAGE analysis of *Kp*NNAT expression and purification. (A) Gel image of 12.5% (w/v) glycine SDS-PAGE gel. *E. coli* cells were transformed with the vector construct containing the recombinant protein and expression was induced with 0.5 mM IPTG (30°C, 210 rpm, for 6 h). The cell lysate was centrifuged to separate the insoluble fraction (pellet) from the soluble fraction (supernatant). The supernatant was purified with Ni^{2+}-IMAC thus yielding the flowthrough. The flowthrough constituted of unbound or weakly bound protein. It was subjected to several wash steps to eliminate the contaminants. A gradient elution with 500 mM imidazole was employed to elute the recombinant protein. The coomassie blue stain was employed to visualise the eluate. The purified protein is depicted in an orange box and its predicted molecular weight was ~25 kDa. (B) Calibration curve used to determine the predicted molecular weight of the protein with SDS-PAGE. The molecular weight of the recombinant protein was predicted with a plot of the logarithm molecular weight of the standards against the relative migration distance (R_f) of those standards. The first two molecular weight marker were omitted for the plotting of the calibration curve as their migrations would impact the linear regression curve. The equation from the plot is pivotal in the prediction of the molecular weight of the protein. The predicted molecular weight of the protein was ~22.66 kDa and depicted as a dot in the black box.

3.4.2. Qualitative and quantitative analysis

The quality of the purification was assessed with a UV-absorption spectrum (Figure 3.6). This was achieved by measuring the absorbance from 240-360 nm. This was to observe nucleic acid contamination at 260 nm or protein aggregation at 340 nm. *Kp*NNAT was quantified using a 1:20 fold dilution followed by measuring the absorbance at 280 nm and 340 nm. The corrected absorbance (A.U.) was obtained by subtracting the absorbance at 340 nm from 280 nm and it was plotted against the dilution factor (Figure 3.7). The plot was fitted with a linear regression curve and the gradient was used to determine the concentration of the protein in conjunction with the Beer-Lambert law, refer to supplementary data for the calculation. The concentration was determined to be 5.44 $mg \cdot mL^{-1}$.

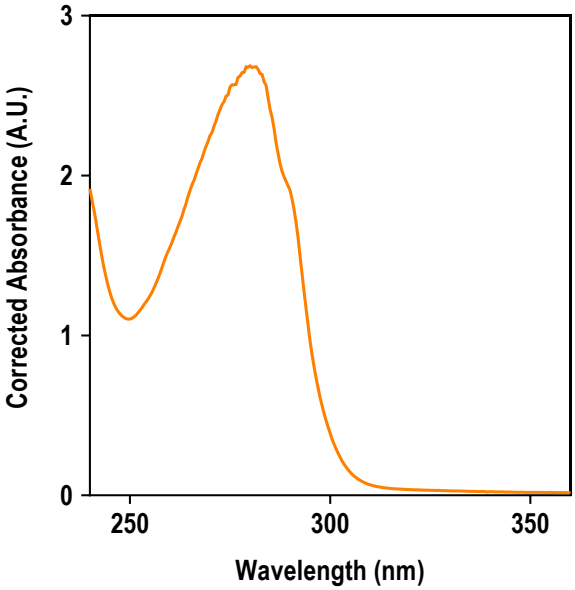

Figure 3.6. Qualitative analysis of *Kp*NNAT with a UV absorption spectrum. The absorbance spectrum was observed between 240-360 nm. The corrected absorbance was achieved by subtracting the absorbance at 280 nm of the blank [10 mM PBS, 0.02% (w/v) NaN_3, 500 mM imidazole, pH 7.2] and the protein sample. Absorbance at 340 nm represents protein aggregation while absorbance at 260 nm indicates DNA contamination. There is no absorbance of light at those wavelengths thus indicating lack of those contaminants. Rather a peak at 280 nm is observed which is indictive of the presence of protein.

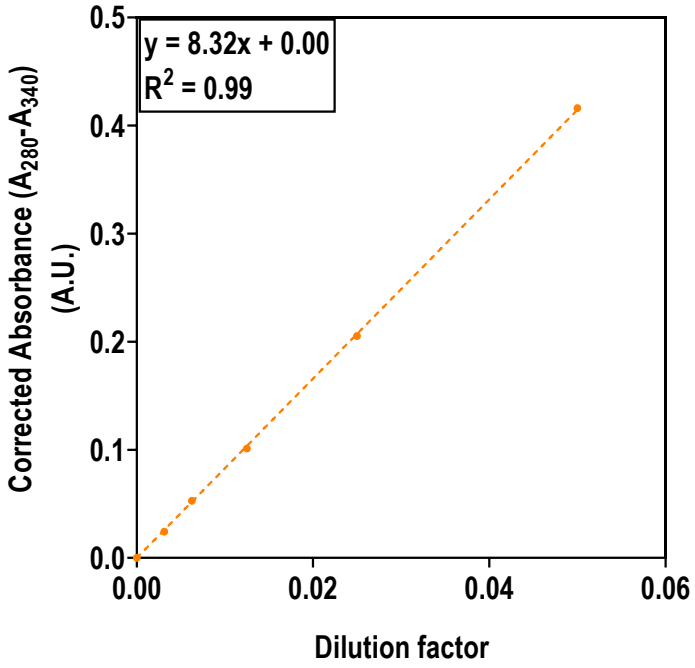

Figure 3.7. Quantitative analysis for the determination of protein concentration. A 1:20 serial dilution was employed to determine the protein concentration. The sample was prepared in 10 mM PBS buffer [137 mM NaCl, 2.7 mM KCl, 10 mM Na_2HPO_4, 2 mM KH_2PO_4, 0.02% (w/v) NaN_3, pH 7.2]. The corrected absorbance was obtained by subtracting the absorbance at 340 nm from absorbance at 280 nm. The linear regression curve of the corrected absorbance against the dilution factor yielded a trendline equation (y = 8.32x + 0.00) from which the slope (8.32) was used to obtain the concentration. The relationship between the absorbance and concentration from the Beer-Lamber law was employed to obtain a concentration of 5.44 mg·mL^{-1}. See supplementary data to obtain the calculation of the concentration.

3.5. Discussion

The recombinant expression of *Kp*NNAT was performed with a pET-28a expression system in *E. coli* T7 cells. Absorbance at 280 nm is monitored to detect the presence of protein due to the ability of protein to absorb UV radiation (Anthis and Clore, 2013). This is a result of intrinsic chromophores such as tryptophan and tyrosine hence improve the specificity of detecting protein using UV-vis spectroscopy. The technique was employed to produce an elution profile (Figure 3.4) as well as an UV absorption spectrum (Figure 3.6). The resulting elution profile following expression with Ni^{2+}-IMAC indicates that the protein was able to be purified. The profile gave insight on which fractions had the most protein, that being the eluates that form part of the peak. SDS-PAGE was further used for the analysis of expression and purification. From the SDS-PAGE gel (Figure 3.5A) it was observed that the protein was successfully expressed, from the pET-28a expression system, and purified. This is displayed as a single ~25 kDa band in the eluate lane.

This is similar to the theoretical molecular weight predicted from ProtParam ExPasy tool and a 2 kDa less deviation as the one reported in literature (Gasteiger *et al.*, 2003; Jeje *et al.*, 2022). The stoichiometry of SDS binding to protein has shown to contribute to the abnormal migration of proteins in SDS-PAGE (Rath *et al.*, 2009). The proposed binding of SDS to protein was 1.4 g of SDS per g of protein but this ratio has been adjusted to 1.5-2 g of SDS per g of protein (Reynolds and Tanford, 1970; Tanford, 1980). Coupled to the stoichiometry of SDS binding to protein is the effect of tertiary structural content such as disulfide bonds to the binding of SDS to protein. It was observed by Pitt-Rivers and Impiombato (1968) that disulfide bonds decrease SDS binding up to 2-folds. And this reduction in SDS binding led to the abnormal migration of protein (Rath *et al.*, 2009). The calibration curve (Figure 3.5B) predicted a molecular weight of ~22.66 kDa. This deviation can be attributed to the accuracy of the calibration curve. Calibration curves are sensitive to outliers as they influence the fit of the regression curve to the raw data and a model fit around the outlier maybe fallacious (Hatch and Prihoda, 1992). With this in mind the information retrieved from the calibration curve may deviate from the natural or true data. Removal of the outlier would eliminate the influence posed by the outlier on the plot but with that is the introduction of data biasness and subsequently queries the validity of the results (Wen *et al.*, 2013). The UV absorption spectrum (Figure 3.6) indicates the purity of *Kp*NNAT. The absence of a peak at 340 nm indicates the absence of protein aggregation. The absorbance at 260 nm indicates the presence of nucleic acid (Gallagher, 1998) thus the absence of a peak at 260 nm indicates the lack of nucleic acid contamination. The $A_{260/280}$ is a ratio of the absorbance at 260 nm to 280 nm and signifies nucleic acid contamination. A ratio of 1.8-2.0 is considered as pure nucleic acid (Kumar *et al.*, 2019). A lower $A_{260/280}$ signifies the lack of nucleic acid contamination (Lucena-Aguilar *et al.*, 2016). An $A_{260/280}$ of 0.58 was recorded in this study thus indicating that there was a lack of nucleic acid contamination in the purified protein. Following purification, the concentration of protein yielded was 218.47 µM (5.44 $mg \cdot mL^{-1}$) and 2 mL of it was obtained. This was sufficient for subsequent studies. It is important to note that the histidine tag was not cleaved thus subsequent studies were performed with *Kp*NNAT that had a histidine tag. The techniques that were used in this chapter were successful in demonstrating the expression and purification of *Kp*NNAT.

Chapter 4

Functional Characterisation of *Kp*NNAT

4.1. Functional characterisation Introduction

A continuous enzyme assay refers to the instantaneous and continuous monitoring of product formation or substrate loss, or activity. Factors that influence enzyme activity include concentration of the constituents in the reaction mixture, detergents or hydrophobic substances that can affect the surface of the protein, ionic strength, metal ions, pH and temperature (Bisswanger, 2014). The activity can be read spectrophotometrically because of the ability of the technique to detect activity in real time. When the product of the desired protein cannot be read spectroscopically a coupled continuous enzyme assay is employed (Scopes, 2001). The reduced form of NAD^+ (NADH) absorbs UV light at 340 nm, while NAD^+ cannot be detected at that wavelength (Walker, 1992). Hence, the activity of the protein can be detected with UV-vis spectrophotometry. Figure 4.1 depicts a coupled continuous enzyme assay that was employed in this study.

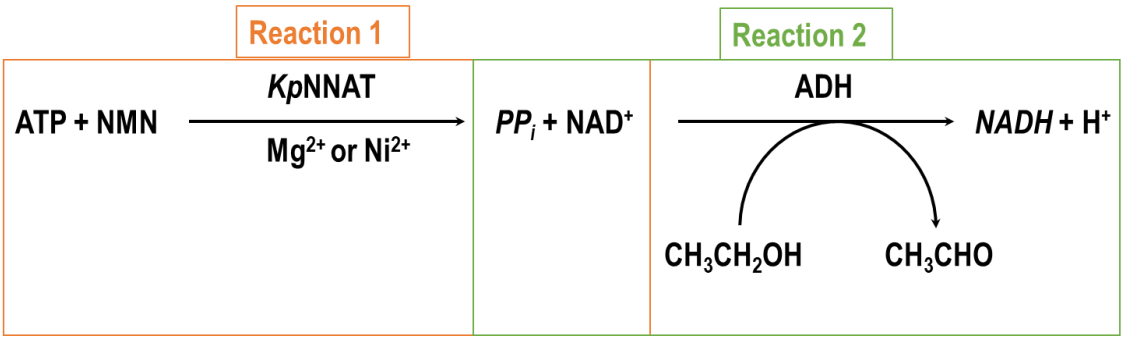

Figure 4.1. A schematic of a coupled continuous enzyme assay. Reaction 1 is catalysed by *Kp*NNAT with substrates NMN and ATP. This reaction produces the initial product, NAD^+, which is the substrate to reaction 2. Reaction 2 is catalysed by ADH with substrates NAD^+ and ethanol it produces NADH and an aldehyde (CH_3CHO).

4.2. Methods

4.2.1. ADH-mediated dual enzyme assay

An ADH-mediated dual enzyme assay was employed to determine the specific activity of *Kp*NNAT. The assay contained a second enzyme, alcohol dehydrogenase (ADH), which was pivotal in the conversion of NAD^+ to NADH. Note that NAD^+ is the product of *Kp*NNAT and the enzyme is the first enzyme in the assay. The absorption of light by NADH was measured at 340 nm. The reaction mixture was prepared with 100 mM Tris-HCl at pH 9. The total volume of the reaction volume was 1 mL and constituted of 1.6 µM of *Kp*NNAT, 1 % (*v/v*) ethanol, 5 mM of metal salts ($MgCl_2$ or $NiCl_2$), 10 U/mL ADH, 0.1 mM ATP, and the reaction was initiated by the addition of 0.5 mM NMN. The reaction was repeated under the same conditions but in the absence of the metal salts. All reactions were performed at 20°C, in triplicates using a Jasco V-630 absorbance spectrophotometer (Jasco, UK).

4.3. Results

4.3.1. ADH-mediated dual enzyme assay

To test the activity of the protein an ADH mediated dual assay was performed at pH 9. This assay was performed in the absence of metal ion as well as the presence of the divalent metal ions Mg^{2+} or Ni^{2+}. The reaction mixture consisted of ATP, ADH, ethanol, and varying concentration of the protein. The reaction was initiated by NMN. The product of the second reaction is NADH. UV-vis spectroscopy was employed to the monitor the increase in absorbance at 340 nm due to the formation of NADH over time (min). The gradient of the resulting linear plots of the enzyme activity ($\mu mole \cdot min^{-1}$) against the amount of protein (mg) (Figure 4.2) is the pseudo specific activity. The value is a representation of the ability of *Kp*NNAT to catalyse the transfer of an adenylyl group from ATP to NMN. It is referred to as pseudo specific activity as the direct quantification of the product formation of the first reaction, catalysed by *Kp*NNAT, could not be achieved through UV-vis spectroscopy. The pseudo specific activity of protein in the presence of Mg^{2+} shows a 3.25-fold increase than Ni^{2+}. The P-value of Mg^{2+} is less than 0.0001, Ni^{2+} 0.0003 and in the absence of metal ion it is 0.0503. Thus, suggesting that Mg^{2+} is more effective than Ni^{2+} in catalsing the reaction of *Kp*NNAT. Though there was some pseudo specific activity observed in the absence of metal ion (0.01 $\mu mole \cdot min^{-1} \cdot mg^{-1}$) it was so low rendering the protein partially active.

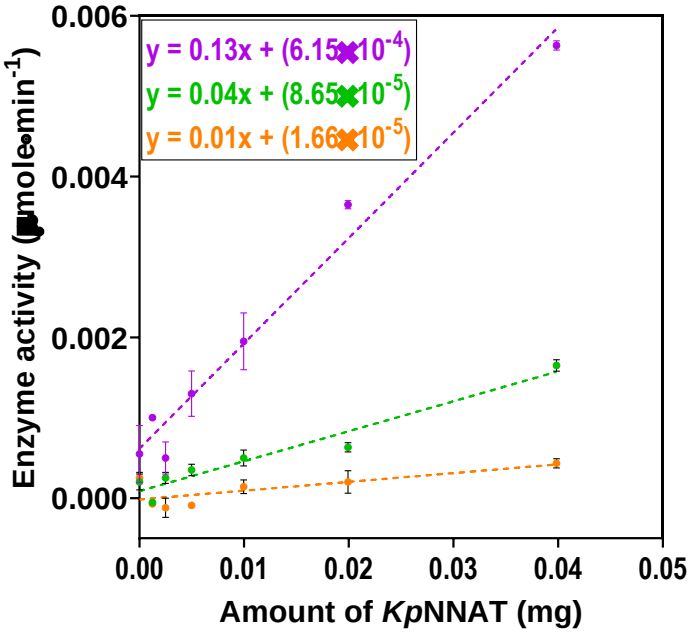

Figure 4.2. Enzyme activity analysis of *Kp*NNAT. The specific enzyme activity was achieved by varying the concentration of KpNNAT in an ADH-mediated dual enzyme assay with ATP and NMN as the initial substrates. The absorbance at 340 nm against time in min was used to obtain the enzyme activity (µmole·min ^{1}). The assay detects NADH formation as it absorbs light at 340 nm. The samples were prepared in 100 mM Tris-HCl, pH 9.0. The linear regression curve of the enzyme activity against the amount of protein (mg) produces a trendline equation and the slope of the equation represents the specific activity of the recombinant protein. In the absence of metal ion (orange) the activity was 0.01 µmole·min^{-1}·mg^{-1}. In the presence of Ni^{2+} (green) the activity was 0.04 µmole·min^{-1}·mg^{-1} and a 0.09 µmole·min^{-1}·mg^{-1} increase in activity was observed for Mg^{2+} (purple).

4.4. Discussion

To further monitor the successful isolation of *Kp*NNAT its function was observed with an ADH-mediated dual enzyme assay. The formation of NADH at an absorbance of 340 nm was monitored, spectrophotometrically, overtime. It was done so either in the holo (presence of metal) or apo (no metal) state of *Kp*NNAT. The activity of the protein was reported as specific activity (Figure 4.2). The specific activity is not an accurate representation of the activity of *Kp*NNAT. The reason is that in order to confirm the activity of *Kp*NNAT a second enzyme was introduced to the assay which was ADH. ADH catalyses the reversible transfer of electrons between NAD^+ and a primary alcohol to produce NADH and an aldehyde (Aquino Neto *et al.*, 2011; Raj *et al.*, 2014). The conversion of NAD^+ and ethanol to its resulting products, by ADH, is optimum at a pH of 9 (Bisswanger, 2014) this is the reason why the reaction in this study was performed at this pH. The

dual enzyme assay is dependent on the second enzyme to confirm the activity of the primary enzyme as the product of the first reaction is the substrate of the second reaction. Hence, the specific activity will be referred to as pseudo specific activity. The psedo-specific activity is dependent on the activity of the enzyme hence it was used to monitor the activity of *Kp*NNAT. The importance of metal ion binding to NNAT has been reported for multiple species of NNAT and it differs across species (Magni *et al.*, 2004). Maximal enzyme activity was observed with Mg^{2+} present as opposed to Ni^{2+}. This preference for Mg^{2+} corroborates with what has been observed in literature for *Kp*NNAT and *h*NNAT isoenzymes 2 and 3 (Jeje *et al.*, 2022; Sorci *et al.*, 2007). The catalytic mechanism is not known for *Kp*NNAT but has been well documented for archaeal NNAT. NNAT catalyses its reaction by cutting the bond between the α-β phosphate of the ATP thus allowing for the nucleophilic substitution of the phosphate group from NMN to subsequently produce NAD^+ (Magni *et al.*, 2004). The solved crystal structure of *Methanococcus jannaschii* NNAT bound to ATP and Mg^{2+} highlights that the catalytic site has positive charges from Mg^{2+}, arginine and the histidine residues, from the conserved motif of nucleotidyltransferases (D'Angelo *et al.*, 2000). The histidine residues bind to the oxygens of the α and β-phosphate of ATP to further produce a positive charge. This positive charge augments the electron deficient character of the α-phosphate of ATP thus allowing for the proficient catalysis of NNAT (D'Angelo *et al.*, 2000). In the absence of metal ion minimal enzyme activity was recorded. This observation solidifies the importance of divalent metal ions in the function of the enzyme. The ability of *Kp*NNAT to be active even with the histidine tag suggests that the tag had negligible effect on the activity. This does not mean that the tag had no absolute effect on the activity of the enzyme. Overall, the technique was effective in assessing the function of *Kp*NNAT.

Chapter 5

Structural characterisation of *Kp*NNAT

5.1 Structural characterisation Introduction

Circular dichroism (CD) is used to assess secondary structural content. It monitors the difference in the absorption of left and right-handed circularly polarised light (Miles and Wallace, 2016). This disparity in absorption of circularly polarised light is denoted as the ellipticity (θ). The amide groups in peptide bond are responsible for the unique CD signals observed in different secondary structural content (Greenfield, 2006). The peptide bond shows UV absorption at 180-250 nm which is known as the far-UV region (Micsonai *et al.*, 2015). The secondary structural content of proteins includes α-helices, β-sheets, and random coils. A protein predominantly α-helical has a two negative CD signals at 222 nm and 208 nm, and a positive CD signal at 193 nm while a predominantly β-sheeted protein has a negative CD signal at 218 nm and a positive CD signal at 195 nm (Greenfield, 2006). Random coiled proteins have a negative CD signal at 195 nm and a small positive CD signal at 210 nm (Greenfield, 2006). This technique gives insight into protein stability and analysing secondary structural content. Fluorescence spectroscopy involves the excitation of a molecule by a photon. The molecule then emits light at a high wavelength and the emission is then detected and referred to as fluorescence. This theory is depicted in Figure 5.1. The energy released during emission is known as non-radiative emission (heat).

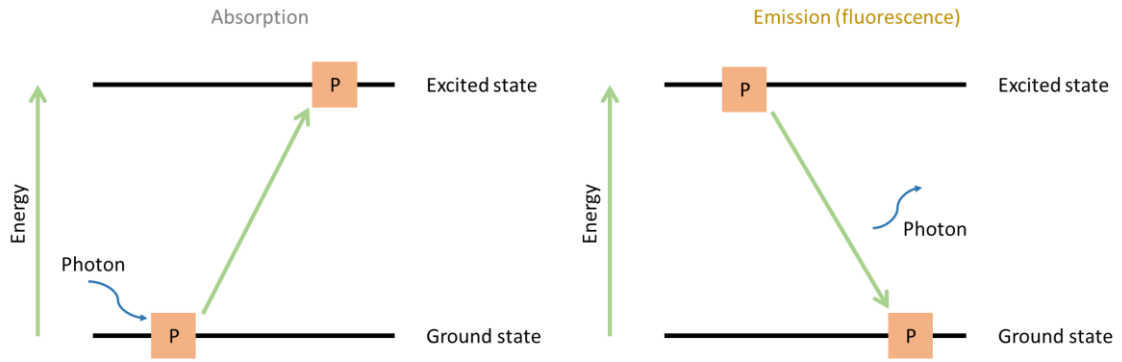

Figure 5.1. A schematic of the principle of fluorescence. Absorption entails the absorption of a photon by a molecule (P). The electrons in the molecule are excited and migrate from ground state to an excited state. Energy is released and electrons migrate from the excited state to a lower energy level, and this is referred to emission.

This technique is used for the tertiary structural analysis of protein through the use of fluorescent substances such as 8-anilino-1-naphthalenesulfonic acid (ANS), 2'/3'-O-(N-Methylanthraniloyl) adenosine-5'-triphosphate (mant-ATP) and SYPRO orange dye. ANS and SYPRO orange dye bind to hydrophobic pockets of a protein thus altering the fluorescent properties of the dye (Oshinbolu *et al.*, 2018). These extrinsic fluorescent dyes are sensitive to the polarity of the solvent and are usually non-fluorescent in aqueous solutions but fluoresce once in contact with hydrophobic pockets (Oshinbolu *et al.*, 2018). This information gives insight on the conformation and stability of the protein. Mant-ATP is an ATP analogue and contains a fluorescent probe bound to the ribose moiety of the nucleotide (Leskovar and Reinstein, 2008). This can yield useful information of ATP binding to the protein. Size exclusion-high performance liquid chromatography (SE-HPLC) is a technique employed for quaternary structural analysis as it separated molecules based on size. The principle is that molecules of different size elute through a column at different rates because of the sieving ability of the porous beads packed into the column (Hong *et al.*, 2012). Large molecules elute first as they cannot enter the pores of the beads and smaller molecules are retarded by the pores of the beads.

5.2. Methods and material

5.2.1. Influence of divalent metal ions on the secondary structure content

The secondary structural content of *Kp*NNAT was examined with Far-UV circular dichroism (CD) using a Jasco J-810 CD spectrophotometer (Jasco, UK). The protein was dialysed against 10 mM sodium phosphate buffer [8 mM Na_2HPO_4, 2 mM NaH_2PO_4, pH 7.4] and stored at 4°C for 16 h. The native samples contained 5 µM *Kp*NNAT, either in the absence or presence of 5 mM of metal salts ($MgCl_2$ or $NiCl_2$). The denatured samples were prepared the same manner as the native samples but with the addition of 8 M urea. A quartz cuvette with a path length of 2 mm was used, and the spectra were measured from 180-255 nm at 20°C. A bandwidth of 2.5 nm and scanning speed of 100 nm/min were used. A total of 3 accumulations were taken from each sample. The CONTIN-LL (Provencher and Gloeckner, 1981) algorithm in Dichroweb (Whitmore and Wallace, 2004) was employed to deconvolute the secondary structural content of native and denatured *Kp*NNAT in the presence and absence of the metal ions. The mean residue ellipticity was determined using the equation 8

$$[\theta] = \frac{100 \times \theta}{\mathrm{Cnl}} \qquad \textbf{(8)}$$

where θ is ellipticity (mdeg), n the number of residues, l the pathlength (cm) and C the protein concentration (mM).

5.2.2. Influence of divalent metal ions and heat on secondary structure

The change in the molar ellipticity signal at 222 nm was observed when the temperature was elevated. This was done to analyse the influence of temperature and divalent metal ions on the secondary structural content of the protein. The experiment was performed in the absence or presence of metal ions. The Jasco J-810 spectrophotometer (Jasco, UK), connected to the Jasco Peltier temperature controller (Jasco, UK), was used to observe the unfolding of the protein. The protein was prepared by dialysing against 10 mM sodium phosphate buffer [8 mM Na_2HPO_4, 2 mM NaH_2PO_4, pH 7.4] and stored at 4°C for 16 h. The samples contained 5 µM *Kp*NNAT, either in the absence or presence of 5 mM metal ions (Mg^{2+} or Ni^{2+}). The temperature was increased from 20-80°C and a 2 mm quartz cuvette was used. The computational settings were a temperature gradient of 1°C·min^{-1}, data pitch of 1°C, bandwidth of 2.5 nm, and a response time of 1 sec.

5.2.3. Extrinsic ANS fluorescence spectroscopy

ANS displacement studies were monitored with a Jasco FP-6300 fluorometer (Jasco, UK). A 1 mM stock of ANS was prepared with 10 mM PBS buffer [137 mM NaCl, 2.7 mM KCl, 10 mM Na_2HPO_4, 2 mM KH_2PO_4, and 0.02 % NaN_3, pH 7.2]. The samples were prepared with either buffer A [10 mM PBS buffer], buffer B [buffer A and 5 mM $MgCl_2$] or buffer C [buffer A and 5 mM $NiCl_2$]. A total of four blank samples were prepared. Samples were prepared as depicted in Table 4.1. Analyte samples were prepared as the aforementioned conditions with the addition of 0.1 mM ANS. The following parameters were used, a data pitch of 0.5 nm, scanning speed of 200 nm/min, and the measurement mode was in emission. The excitation wavelength of 395 nm was used, 3 accumulations were taken, and the spectra were measured from 400-650 nm. All reactions were performed in triplicates (20°C).

Table 5.1. The protein and ATP concentrations were 10 µM and 0.1 mM, respectively.

Sample 1	Sample 2	Sample 3	Sample 4
Buffer	Buffer 10 µM *Kp*NNAT	Buffer 0.1 mM ATP	Buffer 10 µM *Kp*NNAT 0.1 mM ATP

5.2.4. Extrinsic mant-ATP fluorescence spectroscopy

A Jasco FP-6300 fluorometer (Jasco, UK) was employed to monitor the binding of mant-ATP to *Kp*NNAT. The samples were prepared in the same buffers mentioned in Section 5.2.3. A total of three samples were prepared. The parameters used were the same as in Section 5.2.3, except for an excitation wavelength of 355 nm.

5.2.5. SYPRO orange thermal shift assay

The thermal denaturation of *Kp*NNAT was monitored to assess the protein's thermostability by determining the melting temperature (T_m). A CFX96 Touch Real-Time PCR Detection System was used in conjunction with a 96-well PCR plate (Bio-Rad, CA, USA). The wells were loaded according to Figure 5.2. The concentration of protein was 20 µM *Kp*NNAT, 10 × SYPRO Orange fluorescent dye, 5 mM metal salt, 0.1 mM ATP and the thermal shift buffer was [25 mM Tris-HCl, at pH 7.5]. The metal salts used were $MgCl_2$ and $NiSO_4$.The final volume of the reaction was 25 µL and plates were sealed with Microseal 'B' PCR Sealing Film (Bio-Rad, CA, USA). The CFX96 Touch Real-Time PCR Detection System (Bio-Rad, CA, USA) was employed. The parameters were set to a melt curve, with a start temperature of 10-95°C in increments of 0.5°C for 10 sec.

		No metal	Mg^{2+}	Ni^{2+}
		1	2	3
Presence of ATP	A			
	B			
	C			
	D			
Absence of ATP	E			
	F			
	G			
	H			

Figure 5.2. A depiction of a quarter of the 96 well PCR plate which shows the experimental set-up.

5.2.6. Influence of Mg^{2+} and Ni^{2+} ions on the Quaternary structure

A TSKgel SuperSW2000 size exclusion chromatography (SEC) column (Sigma-Aldrich, St Louis, MO, USA) was used in conjunction with a TSKgel SW_{XL} guard column (Sigma-Aldrich, St Louis, MO, USA) to assess the oligomeric state of *Kp*NNAT. The column was connected to a Shimadzu ultrafiltration liquid chromatography (UFLC) SPD-20A HPLC system. The SEC column was equilibrated for 1 h with the SE-HPLC buffer [50 mM Tris-HCl and 500 mM NaCl, pH 7.4]. The flow rate and temperature were kept constant, unless stated otherwise, at 0.2 $mL \cdot min^{-1}$ and 20°C, respectively, and the detection wavelength set to 280 nm. A 20 µL sample of 100 µM *Kp*NNAT, either in the presence or absence of metal ions, was loaded onto the column. With known molecular weights, the protein standards were treated the same as the conditions stated above. Elution times of *Kp*NNAT in the presence or absence of metal ions were compared to the elution times of the protein standards with known molecular weights. The plot was used to determine the approximate molecular weight of *Kp*NNAT, either in the absence or presence of metal ions, using their retention time. The Bio-Rad gel filtration protein standards constituted of thyroglobulin (670 kDa), γ-globulin (158 kDa), ovalbumin (44 kDa), myoglobin (17 kDa), and vitamin B12 (1.5 kDa).

5.3. Results

5.3.1. Far-UV CD

The far-UV CD spectra in the native state of *Kp*NNAT with no metal ion or Mg^{2+} present displayed two negative ellipticity signals at 208 and 220 nm. Without metal ion or when Mg^{2+} is present the positive ellipticity varied, which was 190 nm and 192 nm, respectively. This indicates that the protein is predominantly α-helical under those conditions (Greenfield, 2006). In the presence of Ni^{2+} the distinguishing features of a far-UV CD spectrum of a α-helical protein were lost. The spectrum showed a single negative ellipticity signal at 225 nm and there was no prominent trough at 208 nm. The protein was denatured with 8 M urea, and this is represented as dotted lines on the spectra (Figure 5.3). At that urea concentration, it absorbs far-UV below 210 nm, making the data between 180-210 unreliable (Miles and Wallace, 2016). The experiment was carried out because changes in the spectrum at 222 nm, a distinguishing feature of α-helical protein, can be measured (Kelly *et al.*, 2005). At 220 nm, there was no predominant trough suggesting that the protein was successfully denatured or in its native state.

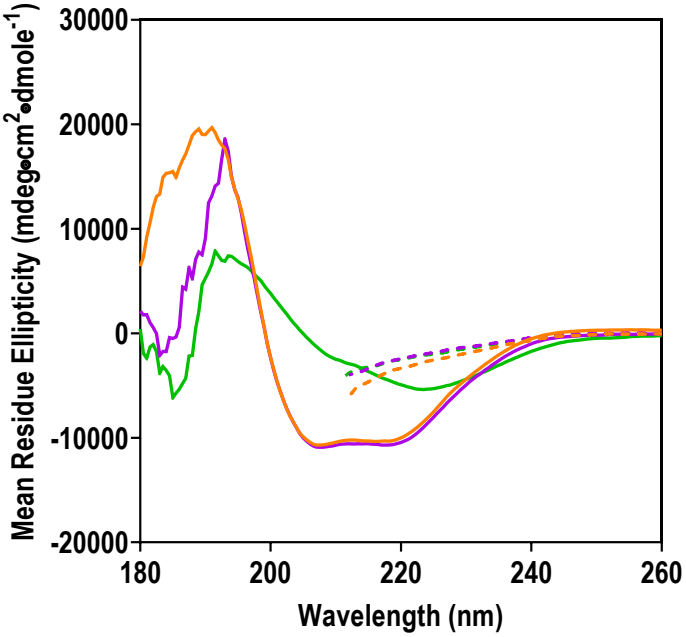

Figure 5.3. Far-UV spectra of *Kp*NNAT. The secondary structural content was determined with Far-UV circular dichroism with 5 µM of protein prepared in 10 mM sodium phosphate buffer [8 mM Na_2HPO_4, 2 mM NaH_2PO_4, pH 7.4] for native samples and 10 mM sodium phosphate buffer [8 mM Na_2HPO_4, 2 mM NaH_2PO_4, pH 7.4] in 8 M urea for denatured samples. The spectra were measured between 180-260 nm. No metal (orange) and Mg^{2+} (purple) display two negative ellipticity signals at 208 and 220 nm. The positive ellipticity signals defer with 190 nm for no metal and 192 nm for magnesium. Ni2+ (green) spectrum is different from the rest, with a loss in α-helical content. This is observed in a spectrum with a positive ellipticity signal at 191 nm and a negative ellipticity at 225 nm. The denatured spectra are represented as dotted lines.

The percentage of secondary structural content was further assessed with Dichweb in conjunction with the CONTIN-ILL algorithm (Table 5.2). The results show that the protein is predominantly α-helical in the absence of metal ion (52%) or when Mg^{2+} (100%) or Ni^{2+} (86%) is present. There were no β-turns or strands observed, but unordered structures were found in the absence of metal ion (48%) and Ni^{2+} (14%). The other important information retrieved from the software was the normalised root-mean-square deviation (NRMSD). The NRMSD depicts the fit of the experimental data to the predicted data; in other words, it shows the best fit of the data. The lower the value, the better the fit. NRMSD values higher than 0.1 indicate the fit is less accurate (Whitmore and Wallace, 2004).

Table 5.2. The analysis of secondary structural content with Dichrowb and the CONTIN-ILL algorithm (Provencher and Gloeckner, 1981), reference set 6 (Sreerama and Woody, 2000).

	α-Helix	β-Strand	β-Turn	Unordered	NRMSD
No metal	0.52	0.00	0.00	0.48	0.80
Mg^{2+}	1.00	0.00	0.00	0.00	0.71
Ni^{2+}	0.86	0.00	0.00	0.14	0.28

*NRMSD: Normalised root mean square deviation is a statistical value that signifies how well the experimental data fits the predicted data. Lower values represent a better fit than higher values.

Thermal stability with far-UV CD was assessed at 222 nm. The resulting melting curves of mean residue ellipticity at 222 nm (mdeg·cm^2·$dmole^{-1}$) against temperature (°C) yielded T_m, which signifies the thermal stability of the protein (Figure 5.4A-C). It was observed that the T_m of apo (without metal ion) and Ni^{2+} had a 7.03°C difference, with apo protein being more stable as opposed to protein Ni^{2+} present. *Kp*NNAT with Mg^{2+} present was the most thermally stable with a T_m of 49.19 ± 0.36°C.

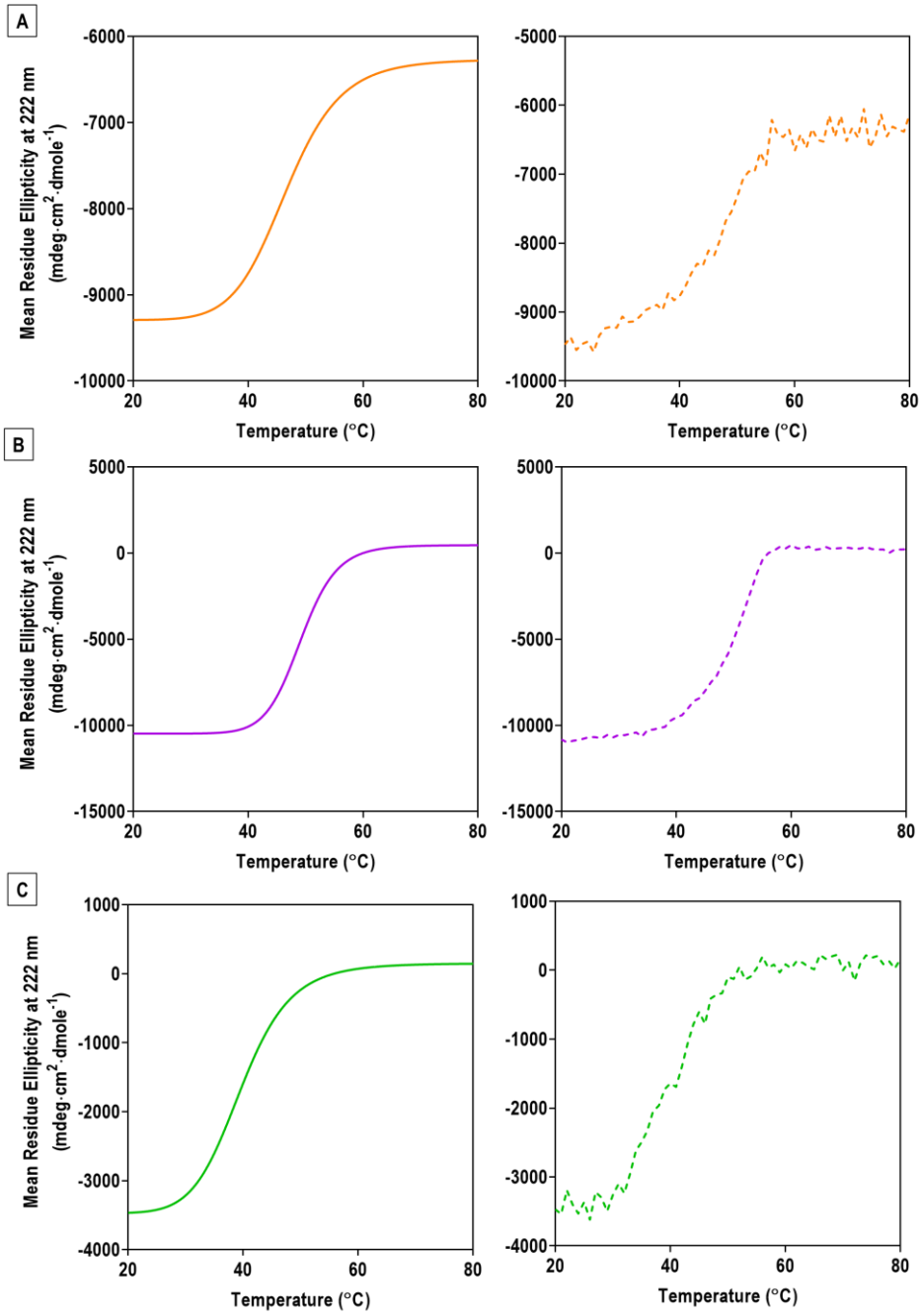

Figure 5.4. CD melting curve to analyse thermal stability of *Kp*NNAT with circular dichroism spectroscopy. The samples were prepared in 10 mM sodium phosphate buffer [8 mM Na_2HPO_4, 2 mM NaH_2PO_4, pH 7.4]. The ellipticity signal was measured at 222 nm for 5 µM *Kp*NNAT and the temperature was observed between 20-80°C. The raw data were fitted to a sigmoid four-parameter model with GraphPad Prism. The fitted data is on the left, while the raw data is on the right. (A) The melting curves of no metal, magnesium and nickel are depicted in A-C, respectively. The T_m for no metal was 46.69 ± 0.80°C and 39.66 ± 0.47°C for nickel. The protein was thermally stable in the presence of magnesium with a T_m of 49.19 ± 0.36°C.

5.3.2. Extrinsic fluorescence emission spectroscopy

Fluorescence emission spectroscopy was utilised to assess the tertiary structure of *Kp*NNAT. Hydrophobic fluorescent dyes such as ANS and SYPRO-orange and a fluorescent nucleotide mant-ATP were used to determine the binding of ATP to the protein. For ANS and mant-ATP the shift in wavelength and the change in emission (quantum yield) were assessed. The fluorescence spectra (Figure 5.5A-C and 5.6A-C) were illustrated as the fluorescence intensity (A.U.) against wavelength (nm), measured from 400-650 nm, for both ANS and mant-ATP emission fluorescence and excitation wavelengths of 395 nm and 355 nm, respectively. Free-ANS and ATP in the presence of ANS show the same trend throughout the conditions. The ANS studies showed an increase of 2.34, 2.91 and 1.65 in fluorescence intensity of protein coupled with ATP compared to apo protein either without or with Mg^{2+} or Ni^{2+} present, respectively. An increase in the fluorescent intensity coupled with a blueshift (decrease in the maximum fluorescence emission) is representative of ANS binding to a hydrophobic site (Gasymov and Glasgow, 2007). A blue shift was observed for Ni^{2+} and a red shift for Mg^{2+} (Table 5.3). Mant-ATP fluorescence shows an increase in fluorescence intensity formant-ATP bound to *Kp*NNAT (relative to free mant-ATP) either in the absence of metal ion, presence of Mg^{2+} or Ni^{2+} to be 53.92, 38.96 and 25.90, respectively. A blueshift in the maximum emission wavelength was observed for Mg^{2+} and Ni^{2+} (Table 5.4). The thermal stability of the *Kp*NNAT was assessed with SYPRO-orange. The thermal denaturation of the protein was monitored at a temperature range of 10-95°C. The T_m of protein in the presence of Mg^{2+} was 52.50°C and 47.50°C for Ni^{2+}, either in the absence or presence of ATP (Figure 5.7A-C and Table 5.5). For no metal, the T_m showed a 0.5°C decrease in the presence of ATP compared to the absence of ATP.

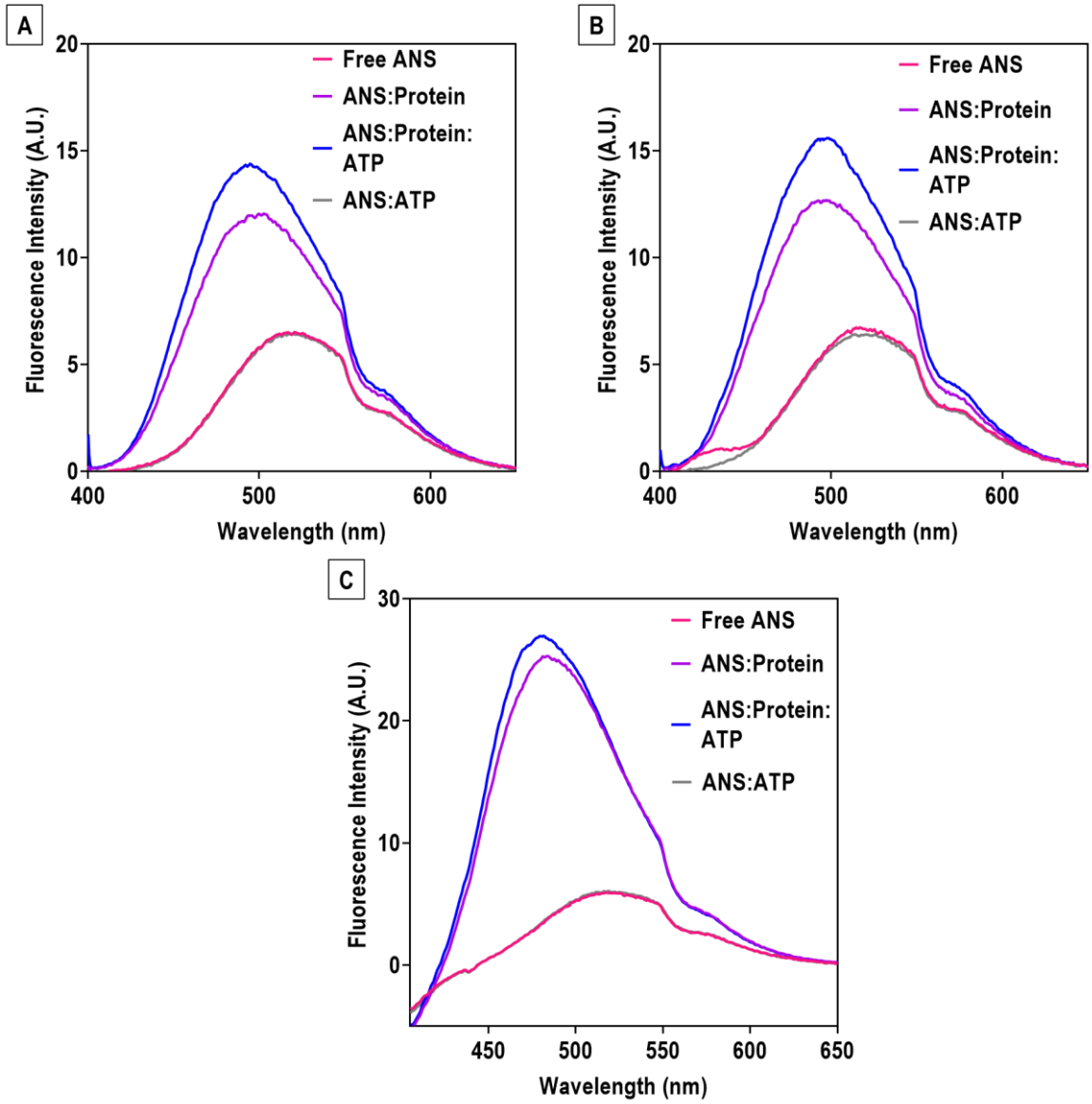

Figure 5.5. Ligandin activity analysis with ANS fluorescence emission spectrometry of *Kp*NNAT in the absence of (A) metal ions, presence of (B) Mg^{2+}, or (C) Ni^{2+}. ANS fluorescence emission spectra of 10 µM of *Kp*NNAT in 10 mM PBS buffer [137 mM NaCl, 2.7 mM KCl, 10 mM Na_2HPO_4, 2 mM KH_2PO_4, and 0.02 % NaN_3, pH 7.2]. The spectra were measured from 400-650 nm with an excitation wavelength of 395 nm. The fluorescence intensity (A.U.) was observed with free 0.1 mM ANS, protein in the presence of ANS, or 0.1 mM ATP bound or unbound to *Kp*NNAT and in the presence of ANS.

Table 5.3. Maximum emission wavelength (λ) nm as well as the shift in the wavelength compared to Apo *Kp*NNAT, either in the presence or absence of metal ions (Mg^{2+} or Ni^{2+})

	Maximum emission wavelength (nm)			Shift compared to Apo *Kp*NNAT		
	No metal	Mg^{2+}	Ni^{2+}	No metal	Mg^{2+}	Ni^{2+}
Free ANS	516	517	517.50	Redshift	Redshift	Redshift
Protein	502.50	497	483.50	Baseline	Baseline	Baseline
Protein with ATP	494.50	498	481.50	Blueshift	Redshift	Blueshift
ATP	520	521	519.50	Redshift	Redshift	Redshift

*Redshift signifies an increase in the maximum emission wavelength relative to Apo protein while a blueshift is its converse.

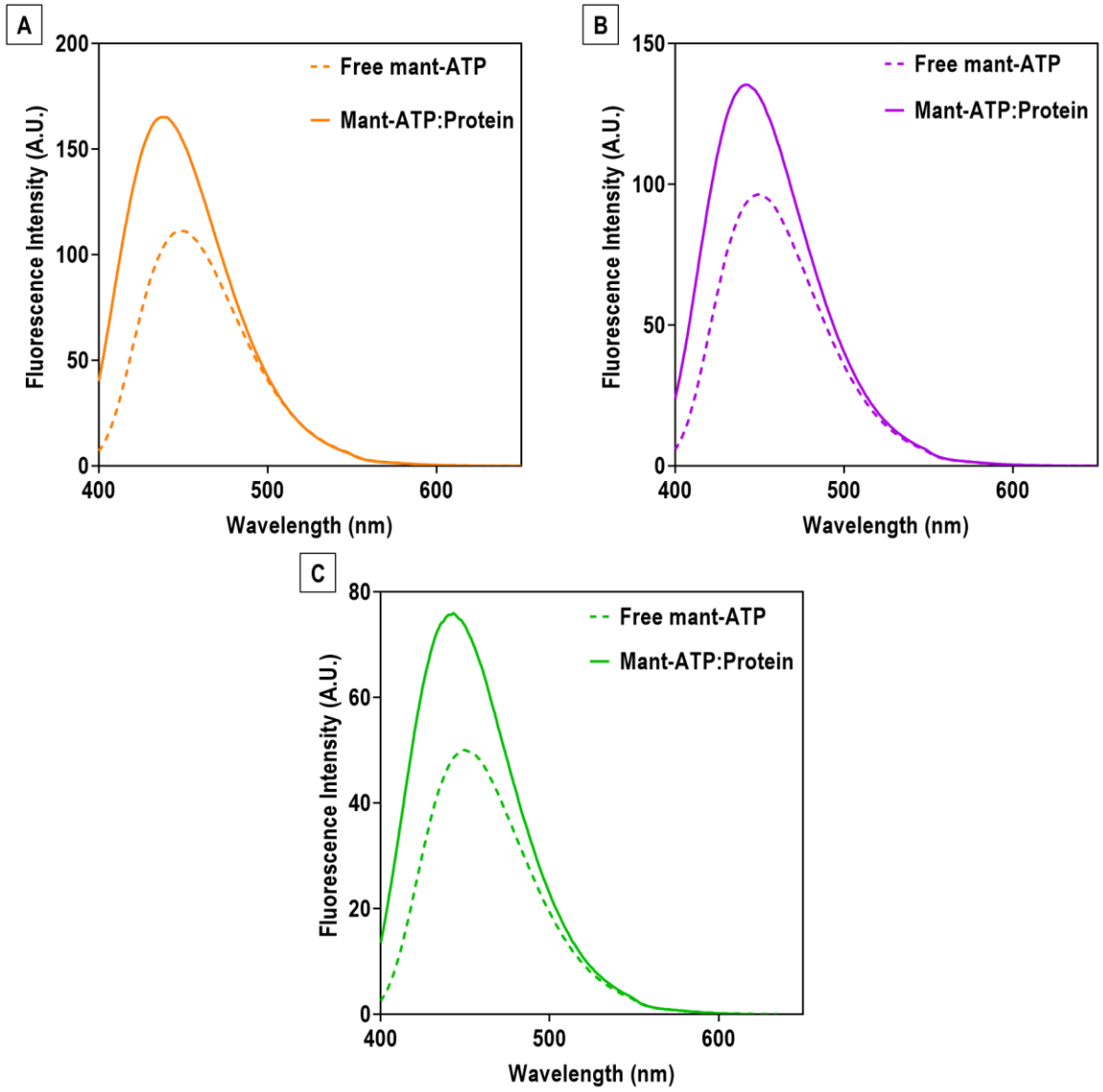

Figure 5.6. Fluorescence emission spectra of mant-ATP binding to *Kp*NNAT in the absence of (A) metal ions, or presence of (B) Mg^{2+} or (C) Ni^{2+}. The mant-ATP fluorescence spectra of 10 µM *Kp*NNAT prepared in 10 mM PBS buffer [137 mM NaCl, 2.7 mM KCl, 10 mM Na_2HPO_4, 2 mM KH_2PO_4, and 0.02 % NaN_3, pH 7.2]. Mant-ATP is excited at 355 nm and the emission was measured from 400-650 nm.

Table 5.4. Maximum emission wavelength (λ) nm as well as the shift in the wavelength of *Kp*NNAT in the presence of Mg^{2+} or Ni^{2+} compared to free mant-ATP.

	Maximum emission wavelength (nm)			Shift compared to No metal *Kp*NNAT		
	No metal	Mg^{2+}	Ni^{2+}	No metal	Mg^{2+}	Ni^{2+}
Protein with mant-ATP	438	442	443	Blueshift	Blueshift	Blueshift

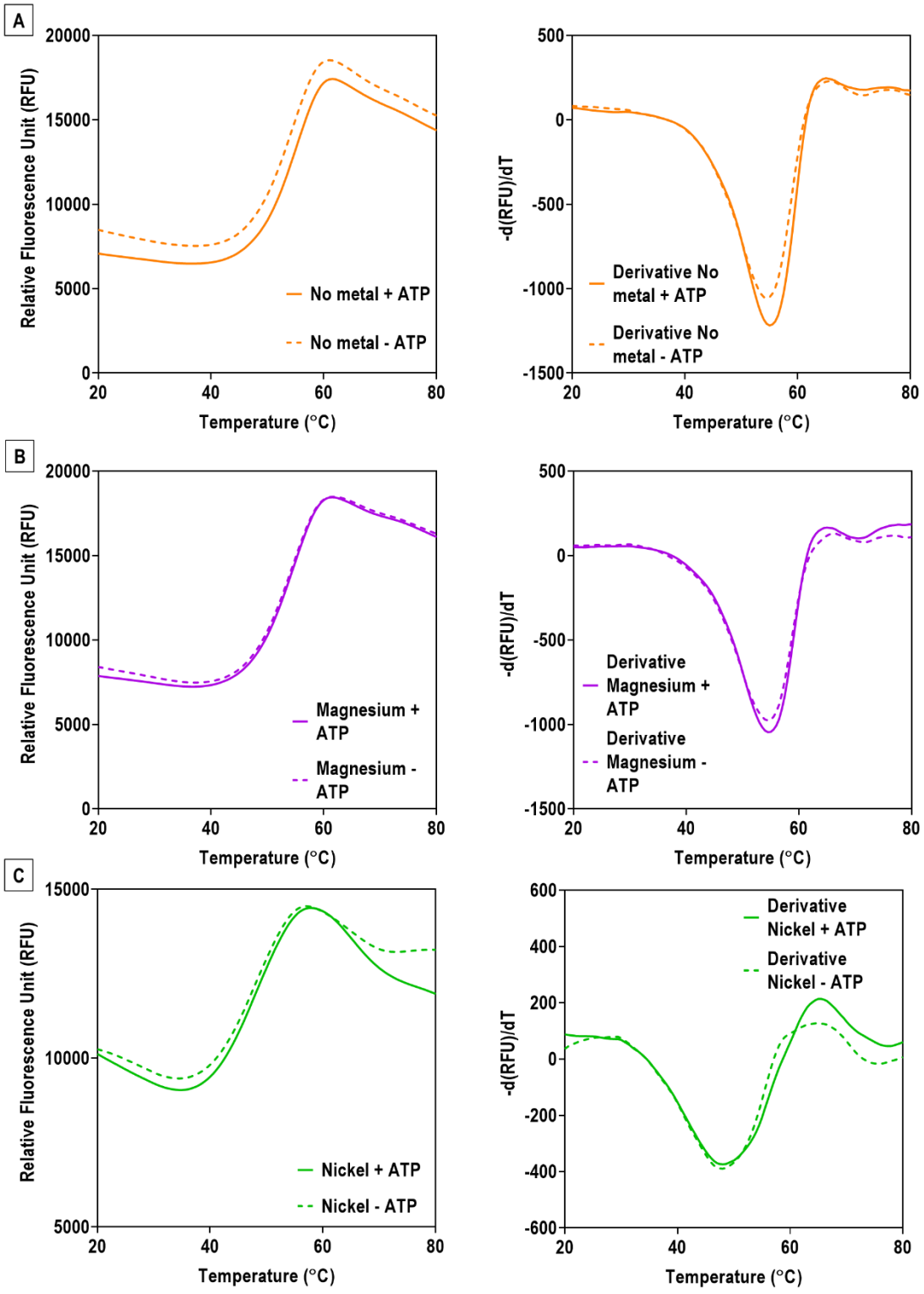

Figure 5.7. Thermal stability of *Kp*NNAT, either in the absence of (A) metal ion, or presence of (B) Mg^{2+} or (C) Ni^{2+}. The thermal shift of 20 µM *Kp*NNAT as it interacts with the SYPRO orange dye and prepared in 25 mM Tris-HCl, at pH 7.5 was monitored. The fluorescence intensity in relative fluorescence unit (RFU) was measured over a temperature range of 20-80°C. The melting curve is depicted on the left while the is the derived –d(RFU)/dT against temperature (°C).

Table 5.5. The melting temperatures (T_m) in °C for *Kp*NNAT in the presence or absence of ATP with, either the presence or absence of metal ions.

	*Kp*NNAT (T_m in °C)	
	No ATP	ATP
No metal	53.00	52.50
Mg^{2+}	52.50	52.50
Ni^{2+}	47.50	47.50

5.3.3. SE-HPLC

The predicted molecular weight and the quaternary structure of the protein were analysed with SE-HPLC. A chromatogram of the absorbance at 280 nm (A.U.) against the retention time (min) yielded distinctive peaks. These peaks represent the time point at which the protein was eluted. The chromatogram constitutes elution profiles of the standard proteins, no metal, protein in the presence of Mg^{2+} or Ni^{2+} (Figure 4.8A). The retention times of the standard proteins were used to produce a calibration curve which is the logarithm molecular weight of the standard proteins against the retention time (Figure 4.8B). The equation from the calibration curve was used to predict the molecular weight of the protein. In the absence of metal ion, the presence of Mg^{2+} or Ni^{2+}, the predicted molecular weight was ~20 kDa, ~18 kDa and ~19 kDa, respectively. It should be noted that there was a peak before and following the larger peak of the chromatograms at ~44 kDa and ~1.5 kDa, respectively.

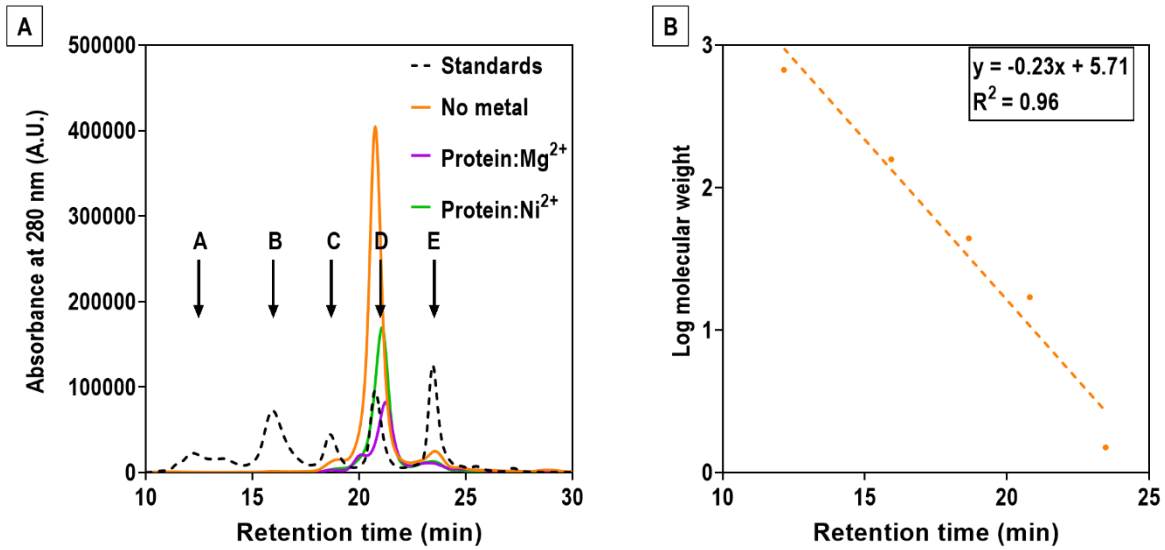

Figure 5.8. Quaternary structural analysis with SE-HPLC. (A) Chromatogram of the standards and 100 µM *Kp*NNAT prepared in 50 mM Tris-HCl and 500 mM NaCl, pH 7.4. A-E represent the peaks of the standards which were thyroglobulin (670 kDa), γ-globulin (158 kDa), ovalbumin (44 kDa), myoglobin (17 kDa), and vitamin B12 (1.5 kDa), respectively. (B) A standard curve of the logarithm molecular weight of the standard proteins against the retention time (min). The equation (y = -0.23x + 5.71) of the plot was used to predict the molecular weight of *Kp*NNAT. The retention time for Mg^{2+} (0.49 min) and Ni^{2+} (0.32 min) is more than no metal ion.

5.4. Discussion

The conserved motif (T/H)XGH is presumed to be involved in ATP binding and catalysis. The histidine residues interact with the α and β-phosphates of the ligand ATP, respectively (D'Angelo *et al.*, 2000). Furthermore, this motif is located in the active site of NNATs (Saridakis and Pai, 2003). The crystal structure NNAT reveal that Mg^{2+} is located close to the α-phosphorous of ATP. The function of this divalent metal ion in conjunction with the histidine residues in the conserved motif is assumed to augment the electrophilic nature of the α-phosphorous of ATP thus facilitating the nucleophilic substitution on the α-phosphorus (D'Angelo *et al.*, 2000). This results in the incision of the α-β phosphodiester bond of ATP and the transfer of the adenylyl group to a mononucleotide such as NMN (Lowe and Tansley, 1983; Saridakis and Pai, 2003). The varied preference for divalent metal ions by NNATs has been detailed in literature (Jeje *et al.*, 2022; Magni *et al.*, 2004). The use of far-UV cd, fluorescence spectroscopy and SE-HPLC gave insight on the influence the metal ions Mg^{2+} or Ni^{2+} have on the structural properties of *Kp*NNAT.

A secondary structure of a protein is stabilised by hydrogen bonds. These hydrogen bonds are between a negatively charged carbonyl oxygen and positively charged amide nitrogen of a polypeptide backbone (Gromiha, 2010; Rehman *et al.*, 2022). These polypeptides fold or coil to produce shapes that contribute the protein's 3D structure. Recurring secondary structural elements in proteins are α-helices and β-pleated sheets (Rehman *et al.*, 2022). A β-sheet is made of elongated and adjacent β-strands that are linked by hydrogen bonds (Nowick, 2008). NNATs are part of the nucleotidyltransferase family characterised by a presence of a Rossmann fold which is a nucleotide binding fold (Stancek *et al.*, 2005a). This fold is described as a core β-sheet, fashioned by six β-strands, flanked by two to three α-helices (Huang *et al.*, 2010). The use of far-UV circular dichroism is used to analyse secondary structural elements. The CD spectra of *Kp*NNAT without metal ion and Mg^{2+} present show that the protein is predominantly α-helical. This is elucidated due to the presence of troughs at 208 and 220 nm and a positive peak at around 190 nm (Figure 5.3). These are distinguishing features of a protein that is predominantly α-helical (Greenfield, 2006). Dichroweb in conjunction with the CONTIN-LL algorithm the percentage of secondary structural content were calculated and from this information it was suggested that the protein is predominantly α-helical (Table 5.2). This predominance in α-helical content is observed in most bacterial NNATs (Jeje *et al.*, 2022; Zhang *et al.*, 2002). In the presence of Ni^{2+} the protein lost its troughs at 208 and 220 thus suggesting a loss in the α-helical content. There was a positive ellipticity at 191 nm showing that UV was absorbed at this wavelength and a high signal to noise was observed as a result of high optical transparency of the sample. This means that protein aggregation may not be the case of a change in the spectrum due to the high signal to noise ratio. This loss in secondary structure of the protein and in the presence of Ni^{2+} has been reported in literature (Jeje *et al.*, 2022). This may suggest that metal ions, especially Ni^{2+}, do influence the secondary structure of *Kp*NNAT. At the concentration of urea, used in the study, it absorbs far-UV below 210 nm making the data between 180-210 unreliable (Miles and Wallace, 2016). The experiment was carried out because changes in the spectrum at 222 nm, a distinguishing feature of α-helical protein, can be measured (Kelly *et al.*, 2005). At 220 nm there was no predominant trough suggesting that the protein was successfully denatured and suggests that *Kp*NNAT was in its native conformation. The thermal denaturation of the *Kp*NNAT was monitored at 222 nm as it is a wavelength that marks α-helical content. From the melt curves (Figure 5.4) it was observed that in the presence of Mg^{2+} the protein was thermally stable while in the presence of Ni^{2+} showed to be least thermally stable. This data corroborates with the thermal shift assay (Figure 5.7 and Table 5.5) performed with the SYPRO orange dye. These results suggest that in the

presence of Ni^{2+} there is a decrease in the thermostability of the protein compared to Mg^{2+}. The results from the thermal shift assay also suggest that the protein's thermal stability is no affected in the presence of ATP as there is no difference in the T_m in the presence of Mg^{2+} or Ni^{2+} but a 0.5°C decrease in the presence of ATP. Factors such as hydrogen bonds, hydrophobic interactions, salt bridges and ionic interactions improve the thermostability of a protein (Kumar *et al.*, 2000). These intermolecular forces contribute to increasing the rigidity of the protein. With increased rigidity the function of the protein can be reduced (Vogt *et al.*, 1997). Upon ligand binding the site of binding may become flexible or rigid (Clark *et al.*, 2019). The rigidity assists in the specificity and increased tautness in the binding of the ligand. The higher the stability of the protein the more rigid the protein is (Vihinen, 1987). This suggests that when Mg^{2+} is present, *Kp*NNAT is rigid to a state where it allows for an increase in thermostability, this is seen in the increase in T_m. The thermal unfolding with far-UV cd was irreversible due to the aggregation of protein caused by elevated temperature. Thermodynamic parameters can be obtained from unfolding studies but the reaction has to be reversible (Benjwal *et al.*, 2006). With that information in mind, thermodynamic parameters could not be obtained because the unfolding was irreversible.

ANS and mant-ATP fluorescence was used to analyse the tertiary structure of *Kp*NNAT. They are both fluorescent probes that characterise the binding sites of protein. An increase in the fluorescence intensity and a blueshift in the maximum emission wavelength indicate an increase in the hydrophobicity or decrease in the polarity of *Kp*NNAT in solution (Gasymov and Glasgow, 2007; Szulc *et al.*, 2013). This is characteristic of the ability of the fluorescent probe to bind to a hydrophobic pocket of a protein. A blueshift and increase in fluorescence intensity is discerned for protein bound to ATP, probed with ANS and without metal ion or with Ni^{2+} present. This suggests that when ATP is present and either without metal ion or with the presence of Ni^{2+}, the protein assumes a conformation that exposes the binding site or a hydrophobic pocket for ANS binding. *Kp*NNAT in the presence of Mg^{2+} shows a slight (1 nm) increase in the maximum emission wavelength upon ATP binding and an increase in the fluorescence intensity. This increase in the maximum emission wavelength is a redshift. This indicates an increase in the polarity thus suggesting that the binding site is uncovered to the water solvent which does not favour binding of ANS. This led to the postulation that Mg^{2+} creates a polar environment in the hydrophobic pocket of *Kp*NNAT. Assuming that the hydrophobic pocket is the nucleotide binding site the polar environment promotes the electrophilic nature of ATP to promote NMN binding which corroborates with what has been

alluded in literature (D'Angelo *et al.*, 2000). This maybe the reason the activity of the protein with Mg^{2+} present is greater than with Ni^{2+} present. While *Kp*NNAT without metal ion or presence of Ni^{2+} promotes a less polar environment in the hydrophobic pocket thus it does not stimulate a favoured environment for the binding of NMN. Hence, the observed minimum enzyme activity with Ni^{2+} present. A blueshift and an increase in the fluorescence intensity is observed for *Kp*NNAT in the absence or presence of metal ion when probed with mant-ATP. This indicates that mant-ATP binds to the nucleotide binding site of the protein. The ANS and mant-ATP data agrees with what has been observed in literature (Jeje *et al.*, 2022).

The SE-HPLC was utilised to predict the molecular weight of *Kp*NNAT and its oligomeric state. The resulting chromatograms (Figure 5.8A) showed the retention times of *Kp*NNAT in the absence of metal ion, presence of Mg^{2+} or Ni^{2+} were 20.75 min, 21.24 min, and 21.07 min, respectively. The predicted molecular weights of *Kp*NNAT in the absence of metal ion, presence of Mg^{2+} or Ni^{2+} were ~20 kDa, ~18 kDa, and ~19 kDa, respectively. This information was obtained by using the equation from the calibration curve (Figure 5.8B). The principle of SE-HPLC infer that larger molecules elute first as they are excluded from the pores of the beads, in the stationary phase (Hong *et al.*, 2012). With this concept in mind and taking into account the retention times and predicted molecular weights of *Kp*NNAT under varying conditions it is proposed that the protein conforms into a compacted globular structure in the presence of metal ions. This is because the retention time and predicted molecular weight decreases in the presence of metal ion. Furthermore, *Kp*NNAT in the presence of Mg^{2+} has the least retention time thus suggesting that it assumes the smallest conformation, or the most compacted conformation compared to *Kp*NNAT in the presence of Ni^{2+}. The technique also showed that *Kp*NNAT in the absence or presence of metal ion was in its monomeric state and no other oligomeric states were observed from the chromatograms. This monomeric state is also observed in other bacterial NNATs (Daya *et al.*, 2022; Zhang *et al.*, 2002). The predicted molecular weight of the protein with SE-HPLC (~20 kDa) differs with the theoretical molecular weight (25 kDa). The deviation in the predicted molecular weight compared to the theoretical molecular weight has been observed in *Plasmodium falciparum* conjugated to a six membered histidine tag (Contreras-Rodríguez *et al.*, 2018). This deviation could be attributed to multiple factors including protein concentration, buffer used, pH and the gel matrix. Another contribution documented is the pore size of the beads in the gel matrix. The pore size of beads affects the range of the molecular weight and also the gradient of the calibration curve thus affecting the validity of the predicted molecular weight (Hong *et al.*, 2012). The adsorption of

protein to the gel matrix, as a result of electrostatic interactions between the protein and the functional group (silanol) on the silicon, was postulated to influence the retention time of proteins (Arakawa *et al.*, 2010; Kopaciewicz and Regnier, 1982). The peaks that are at ~44 kDa and ~1.5 kDa maybe a result of the column being contaminated by the standards. The reason for this is that the standards were ran before the protein solution thus the thorough cleaning of the standards off the column prior to the injection of the protein was not successful. Future studies should consider loading the protein before the standards or adopting alternative and effective cleaning techniques.

To corroborate the assumptions made from the observations obtained the structural techniques X-ray crystallography studies should be considered in the future. It will give a better insight into the conformation and binding of substrates in the active site of *Kp*NNAT.

Chapter 6

Isothermal titration calorimetry

6.1. Isothermal Titration Calorimetry Introduction

Isothermal titration calorimetry (ITC) is employed for interaction studies. It measures the heat absorbed or released when the desired protein binds to a substrate (Freire *et al.*, 1990). It yields thermodynamic parameters such as stoichiometry (n), enthalpy, and the binding affinity (Freyer and Lewis, 2008). From the information obtained directly from ITC, the Gibbs free energy and the entropy can be derived (Liang, 2008). This technique does not require altering a protein or its substrate by either immobilisation or the addition of fluorescent markers (Freyer and Lewis, 2008). The ITC instrument consists of a reference and sample cell and a syringe or burette attached to the sample cell, refer to Figure 6.1. It involves the titration usually of a substrate, in a syringe, into a protein, in the sample cell. This causes a binding reaction to occur, resulting in either the release or absorption of heat, which is directly proportional to the amount of binding (Liang, 2008). When heat is absorbed from the surrounds, the reaction is considered to be endothermic conversely, when heat is released to the surrounds, the reaction is exothermic (Freyer and Lewis, 2008). ITC can also be used for enzyme kinetics. It is advantageous over spectrophotometry techniques as it measures activity in real-time, does not need the alteration of substrate or protein with fluorescent dyes and measures the product of the desired protein thus eliminating the use of secondary enzymes such as in a coupled assay (Wang *et al.*, 2020a).

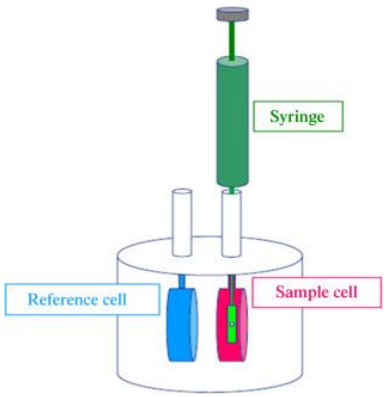

Figure 6.1. The instrumental design of an Isothermal titration calorimeter (Srivastava and Yadav, 2019).

6.2. Methods and material

6.2.1. Influence of Mg^{2+} and Ni^{2+} on ATP binding to *Kp*NNAT using ITC

A Nano ITC Standard Volume instrument (TA Instruments, USA) was employed to analyse the thermodynamic parameters of *Kp*NNAT binding ATP in the absence or presence of divalent metal ions (Mg^{2+} or Ni^{2+}). *Kp*NNAT was dialysed against 10 mM PBS buffer [137 mM NaCl, 2.7 mM KCl, 10 mM Na_2HPO_4, 2 mM KH_2PO_4, and 0.02 % NaN_3, pH 7.2] at 4°C for 16 h. The substrate containing 5 mM ATP, 5 mM metal salts ($MgCl_2$ and $NiCl_2$), and 1 mM TCEP were prepared with PBS dialysate. The sample cell was loaded with 40 µM *Kp*NNAT, and 1 mM TCEP, either in the absence or presence of 5 mM metal ion or no metal ion. A 250 µL syringe was loaded with 5 mM ATP, either in the absence or presence of 5 mM metal ions. The heats of dilutions were determined as aforementioned in the absence of *Kp*NNAT. The experimental conditions constituted a stirring rate of 300 rpm, 30 injections, 5 µL injection volume, 300-sec injection intervals at 25°C. The NanoAnalyze software was used to analyse the data, which was fitted using an independent model. The data was used to determine the $\Delta H°$, K_d and stoichiometry (n). Using the aforementioned parameters, the $\Delta G°$ and $\Delta S°$ were calculated using the following equations

$$\Delta G° = RT \ln \left(\frac{1}{K_d}\right) \quad \textbf{(9)}$$

$$\Delta G° = \Delta H° - T\Delta S° \quad \textbf{(10)}$$

where R is the gas constant 8.3145 $J \cdot mol^{-1} \cdot K^{-1}$ and T the absolute temperature in K.

6.2.2. Influence of Mg^{2+} and Ni^{2+} on the kinetics of *Kp*NNAT

A multiple injection method was employed to determine the impact of divalent metal ions on *Kp*NNAT kinetics in the native state. The metal salts ($MgCl_2$ or $NiCl_2$), ATP, NMN, TCEP, and *Kp*NNAT were prepared the same as stated in 6.2.1. The sample cell was loaded with 10 nM *Kp*NNAT, 0.1 mM ATP, and 1 mM TCEP, either in the absence or presence of 5 mM metal ions. The substrate 100 mM NMN with 0.1 mM ATP, and 1 mM TCEP, either in the absence or presence of 5 mM metal ions, was titrated into the sample cell. The heats of dilutions were determined as aforementioned in the absence of *Kp*NNAT. The experimental conditions constituted a stirring rate of 300 rpm, 15 injections 5 µL injection volume, 400-sec injection intervals, at 25°C. The ΔH_{app} was determined with a separate reaction. The reaction contained 10 mM *Kp*NNAT, 0.1 mM ATP, and 1 mM TCEP, either in the absence or presence of 5 mM

metal ions. The substrate 1 mM of NMN with 0.1 mM ATP, and 1 mM TCEP, either in the absence or presence of 5 mM metal ions, was titrated into the sample cell. The experimental conditions were a stirring rate of 300 rpm, 3 injections, 4 µL injection volume, and 400-sec injection intervals, at 25°C. The ΔH_{app} is calculated from the integrated peak value divided by the amount of injected substrate. Three injections were made to monitor production inhibition.

6.3. Results

6.2.1. Influence of Mg^{2+} and Ni^{2+} on ATP binding to *Kp*NNAT using ITC

The thermodynamic parameters associated with the binding of ATP to *Kp*NNAT were determined with isothermal titration calorimetry. ATP was injected into the sample cell containing *Kp*NNAT until the protein's binding sites were saturated. The interaction between the protein and the substrate yielded isotherms. An independent model was used to fit the data. The isotherm and fitted data of the interaction between *Kp*NNAT and ATP in the presence of Mg^{2+} is exothermic reaction ($\Delta H° < 0$) Furthermore, the reaction was entropically favourable ($\Delta S° > 0$), spontaneous ($\Delta G° < 0$) and had a stoichiometry of ~5 molecules of ATP per mole of *Kp*NNAT (Figure 6.2 and Table 6.1). In the absence of cations and presence of Ni^{2+} the reaction was endothermic ($\Delta H° > 0$); there seemed to be no interaction between ATP and *Kp*NNAT thus, thermodynamic parameters could not be obtained (Figure 6.3 and 6.4).

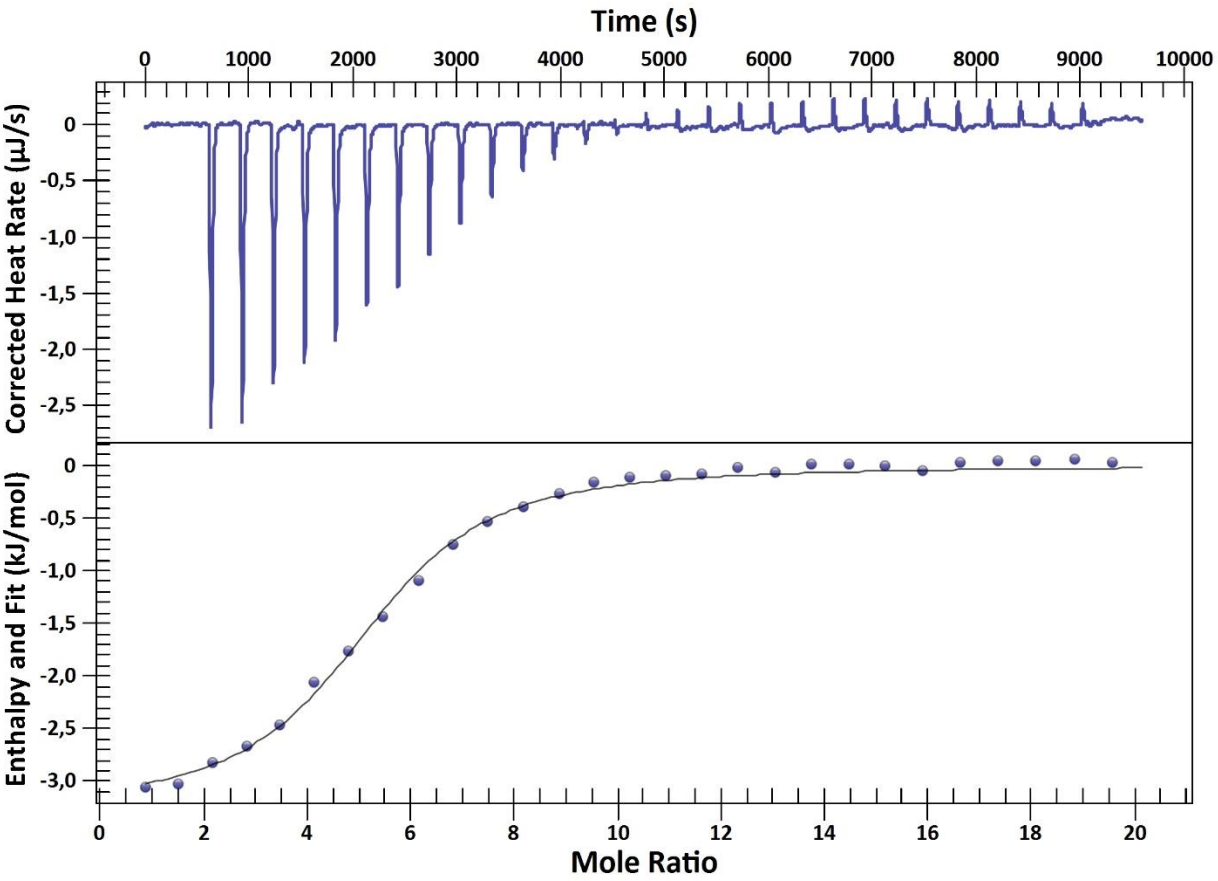

Figure 6.2. Thermogram of the interaction between ATP and *Kp*NNAT in the presence of Mg^{2+}. ITC was used to monitor the binding of 5 mM ATP to 40 µM recombinant protein prepared in 10 mM PBS buffer [137 mM NaCl, 2.7 mM KCl, 10 mM Na_2HPO_4, 2 mM KH_2PO_4, and 0.02% NaN_3, 1 mM TCEP, pH 7.2]. The data were fitted to an independent model and analysed with the NanoAnalyze software.

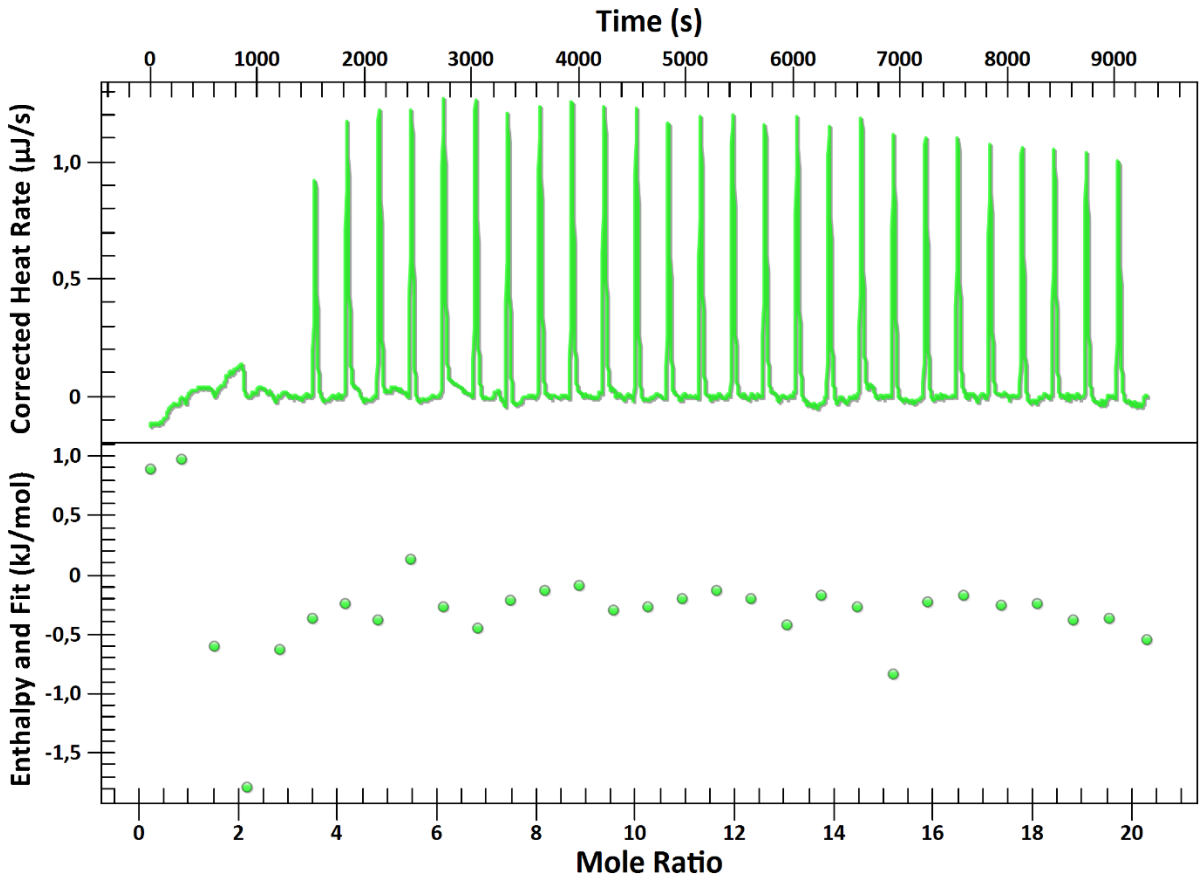

Figure 6.3. Thermogram of the interaction between ATP and *Kp*NNAT in the presence of Ni^{2+}. ITC was used to monitor the binding of 5 mM ATP to 40 µM recombinant protein prepared in 10 mM PBS buffer [137 mM NaCl, 2.7 mM KCl, 10 mM Na_2HPO_4, 2 mM KH_2PO_4, and 0.02% NaN_3, 1 mM TCEP, pH 7.2]. The data was fitted to an independent model and analysed with the NanoAnalyze software.

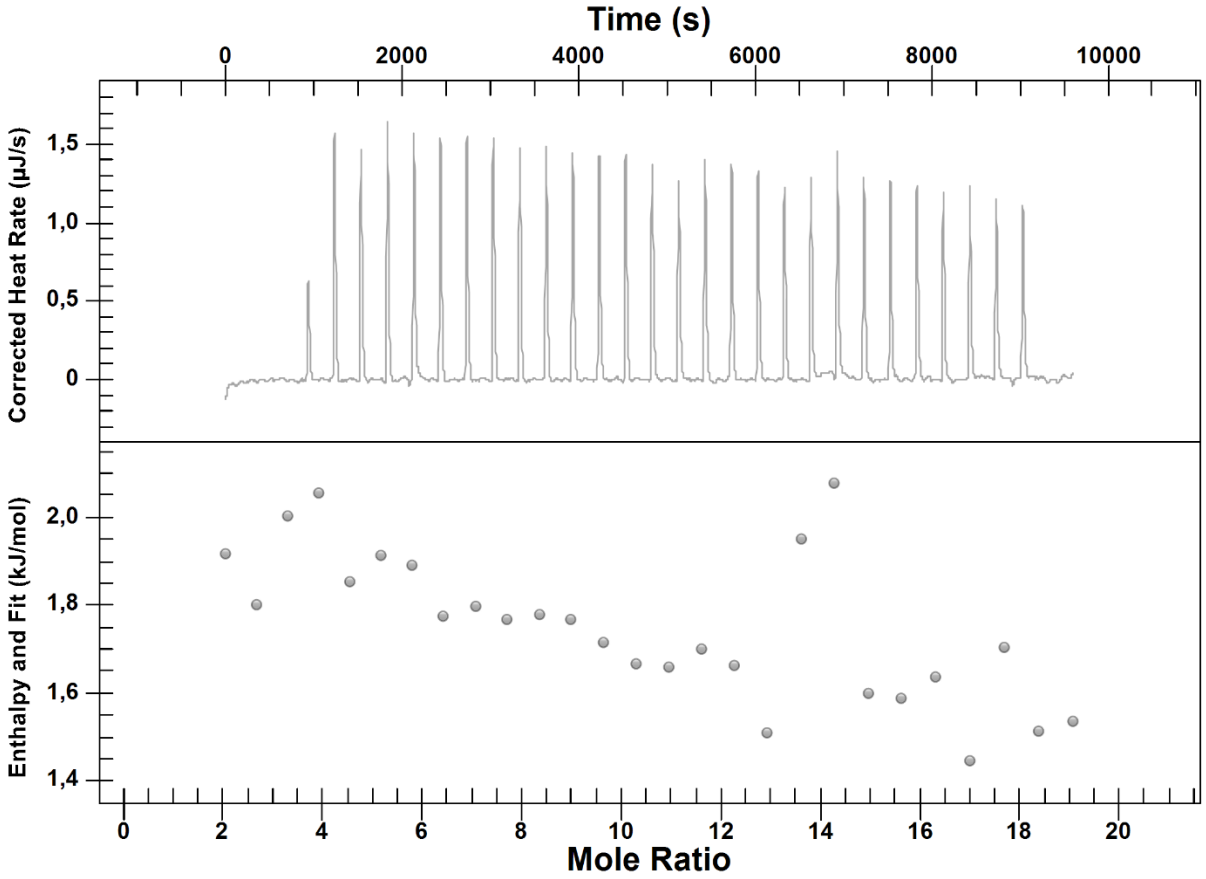

Figure 6.4. Thermogram of the interaction between ATP and *Kp*NNAT in absence of metal ion. ITC was used to monitor the binding of 5 mM ATP to 40 µM recombinant protein prepared in 10 mM PBS buffer [137 mM NaCl, 2.7 mM KCl, 10 mM Na_2HPO_4, 2 mM KH_2PO_4, and 0.02% NaN_3, 1 mM TCEP, pH 7.2]. The data was fitted to an independent model and analysed with the NanoAnalyze software.

Table 6.1. Thermodynamic parameters of *Kp*NNAT binding to ATP in the presence of Mg^{2+}. The samples were buffered by 10 mM PBS and 1 mM Tris(2-carboxyethyl) phosphine (TCEP), pH 7.2, at 25°C. The independent model site binding was used to fit the binding isotherm.

Enzyme	$\Delta G°$	$\Delta H°$	$-T\Delta S°$	K_d
		(kJ·mole^{-1})		(µM)
*Kp*NNAT + Mg^{2+}	-27.87	-3.27	- 24.60	13.10

6.3.2. Influence of Mg^{2+} and Ni^{2+} on *Kp*NNAT kinetics

The multiple injection method with isothermal titration calorimetry was employed to determine enzyme kinetic parameters. NMN was titrated into *Kp*NNAT while ATP saturated the ATP binding sites of the protein. The reaction rate was monitored by observing a change in heat rate with each titration of NMN over time. With each injection, a new baseline or steady-state was achieved (Figure 6.5A). The ΔH_{app} cannot be obtained directly from this experiment, so a separate experiment was performed with increased protein concentration and reduced substrate concentration (Inset). The calculated ΔH_{app} (-1.01 $kJ \cdot mole^{-1}$) was determined by averaging and dividing the integrated peak from each injection by the concentration of substrate and reaction volume (See supplementary data for the calculation). The change in heat rate over time for each injection relative to the initial baseline is directly proportional to the rate of enzyme activity (Equation 1). The calculated ΔH_{app} in conjunction with the heat rate was used to determine the enzyme activity at each injection. With the enzyme activity against the substrate concentration, a Michaelis-Menten curve was plotted (Figure 6.5B) and from the plot the kinetic parameters were obtained. The k_{cat} was 0.02 s^{-1} and the k_{cat}/K_m was 6122.45 $M^{-1} \cdot s^{-1}$ (See supplementary data for the calculation).

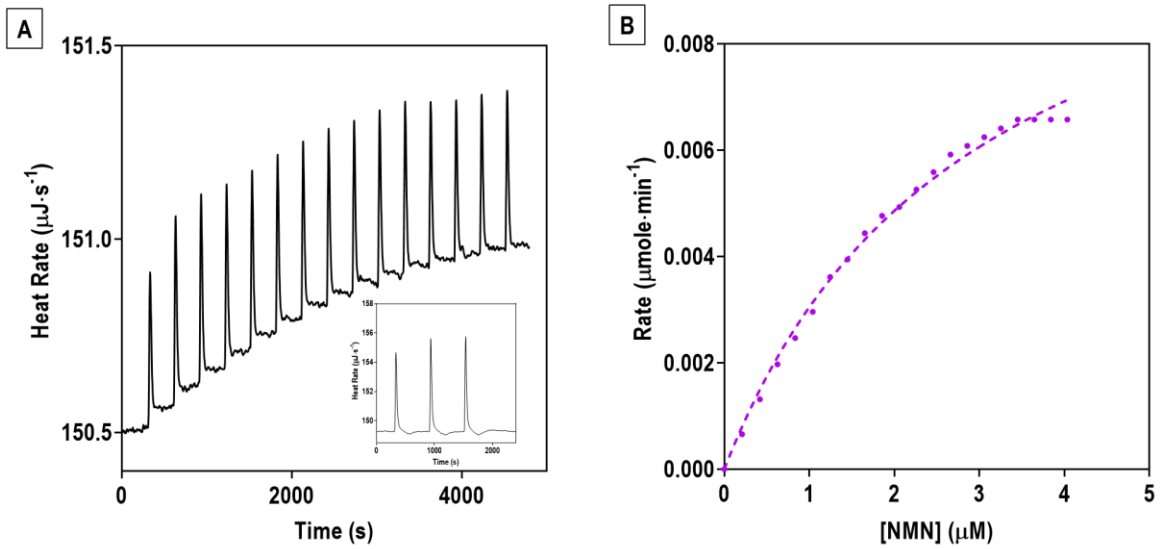

Figure 6.5. Isothermal titration calorimetry for the determination of the kinetics of *Kp*NNAT. (A) A thermogram achieved from the multiple injection method were 100 mM NMN, in the syringe, was injected to 10 nM *Kp*NNAT prepared in 10 mM PBS buffer [137 mM NaCl, 2.7 mM KCl, 10 mM Na_2HPO_4, 2 mM KH_2PO_4, 0.02% NaN_3, and 1 mM TCEP, pH 7.2]. A total of 15 injections were measured with an injection volume of 5 µL. (Inset) ΔH_{app} determination were 1 mM of NMN was titrated to 10 mM *Kp*NNAT prepared in 10 mM PBS buffer [137 mM NaCl, 2.7 mM KCl, 10 mM Na_2HPO_4, 2 mM KH_2PO_4, 0.02% NaN_3, and 1 mM TCEP, pH 7.2]. Three injections were taken with an injection volume of 4 µL. (B) Michaelis-Menten plot the enzyme activity (µmole·min^{-1}) against the substrate concentration (µM). The raw data was fitted to a non-linear regression curve analysed with GraphPad prism. The V_{max} is 7.15×10^{-3} µmole·min^{-1} while the K_m is 2.94 µM. The kinetic parameters were obtained from the fitted plot produced by GraphPad prism.

6.4. Discussion

ITC was employed to assess the thermodynamic parameters upon ATP binding to *Kp*NNAT. The resulting isotherm (Figure 6.2) for *Kp*NNAT in the presence of Mg^{2+} show that the reaction is exothermic and enthalpically favourable. These results corroborate with what has been observed upon ATP, in the presence of Mg^{2+}, binding to bacterial NNAT (Daya *et al.*, 2022; Sershon *et al.*, 2009). The independent binding model was used to fit the raw data. This model assumes that a ligand binds to a single binding site thus suggesting that ATP binds to a single site on NNAT. Furthermore, the reaction is spontaneous and entropically favourable thus suggesting that the reaction did not require the input of external energy to drive ATP binding. When ligand binds to a protein the contribution of the enthalpy is that it facilitates in the formation of non-covalent interactions (Du *et al.*, 2016). Theses interactions include hydrogen bonds, van de Waals forces and ionic interactions. The binding entropy (ΔS) is influenced by

the solvation entropy ((ΔS_{solv}), conformational entropy (ΔS_{conf}) and the loss of motion ($\Delta S_{r/t}$). The solvation entropy marks the influence of the solvent upon ligand binding. The conformational entropy represents the conformation of both the ligand and protein when the ligand binds to protein it maybe entropically favourable or unfavourable. And the loss of motion contributes to the binding entropy as it takes into account the rotation and translation of the protein or ligand. A loss in the motion is entropically unfavourable (Du *et al.*, 2016). *Ec*NNAT has shown to be conformationally flexible and this is favoured in ligand binding (Zhang *et al.*, 2002). X-ray crystallography results of archaeal NNAT indicate that the first histidine in the conserved motif ((T/H)XGH) is involved in hydrogen bonding with ATP and two water molecules are hydrogen bonded to the binding site of ATP (D'Angelo *et al.*, 2000). The role of solvent (water) in protein-ligand complexes is multifactorial. NNATs have shown to have water molecules in their active site (D'Angelo *et al.*, 2000; Zhang *et al.*, 2002). The role of solvent (water) is to assist or partake in hydrogen bonding of substituents involved in the binding process (Schiebel *et al.*, 2018). Water displacement in the binding pocket of the protein as a result of ligand binding affects the affinity and the enthalpy or entropy (Schiebel *et al.*, 2018). The binding affinity can be augmented by the displacement of thermodynamically unfavourable water molecules upon protein-ligand complex formation (Wang *et al.*, 2011). Hydrophobic interactions are associated with entropy and are important as they are the thermodynamic driving force of protein-ligand complex formation (Holdgate, 2017; Young *et al.*, 2007). The orientation of water molecules in the binding site tend to be ordered when exposed to nonpolar molecules and this results in the decrease of entropy which is entropically unfavourable (Frank and Evans, 1945). The favourable entropy may be a result of the water molecules being exposed to a less hydrophobic environment which is created by the Mg^{2+} and the conserved binding motif. This corroborates with the ANS binding studies and what has been proposed in literature. Hydrogen bonds are considered to be enthalpically favourable (Holdgate, 2017). This suggests that the favourable enthalpy is a result of hydrogen bonds in the ATP binding site. In the absence of metal ion or presence of Ni^{2+} there seems to be no binding of ATP to the protein thus thermodynamic parameters could not be obtained. This may be the reason that the activity of the protein was minimal. A crystal structure and molecular modelling can be employed to better understand the binding site of *Kp*NNAT. This should be a consideration for future work on the protein.

The Wiseman constant (c) is a value that dictates the shape of the titration curve or the isotherm. Its equation is depicted as

$$c = \frac{n[P]}{K_d} \quad \textbf{(11)}$$

where n is the number of binding sites, [P] is the protein concentration in the sample cell (Dutta *et al.*, 2015). The value does not have units. A c-value of 1 to 1000 indicate moderate binding while values less than 1 or more than 1000 represent weak or tight ligand binding, respectively (Wiseman *et al.*, 1989). Furthermore, isotherms that display a c-value of 1-1000 yield accurate binding or dissociation constants (Wiseman *et al.*, 1989). The c-value for *Kp*NNAT in the presence of Mg^{2+} was 3.05. While it would suggest moderate binding according to Wiseman *et al.* (1989) but this is not the case according to current information (Ge *et al.*, 2021). To obtain a sigmoidal isotherm that represents a good fit of the data the c-value should be 20-100 (Dutta *et al.*, 2015). Furthermore, if the c-value is less than 5 then the shape of the titration curve does not allow the accurate estimation of the thermodynamic parameters (Dutta *et al.*, 2015). The value obtained from this study is far less than what is proposed. This means that the fit of the data is not the best to fully represent the accurate estimation of the thermodynamic parameters. The high dissociation constant (Table 5.1) shows low binding affinity. This means that there is weak binding between ATP and *Kp*NNAT in the presence of Mg^{2+}. Future studies should focus on improving the ratio of concentration of protein to substrate.

A novel approach in determining the enzyme kinetic parameters with ITC was employed. This was achieved with the use of the multiple injection method. The advantages of the multiple injection method are that low enzyme concentration is used, less substrate is converted to product as a result product inhibition is negligible, (Wang *et al.*, 2020b). This technique was not successful in yielding kinetic parameters for *Kp*NNAT in the absence of metal ion or presence of Ni^{2+} but the results are displayed in the supplementary section. The protein did not reach a point of saturation even at high NMN concentration. This may be attributed to the inability for ATP to bind to the protein, documented in the binding studies, as a result the transfer of the adenylyl group to NMN was not achieved rendering the protein nonfunctional under those conditions. In the presence of Mg^{2+} the protein was functional, and the technique was able to yield kinetic parameters. The Michaelis-Menten constant (K_m) signifies the affinity of the enzyme to the substrate and represents the minimum substrate concentration required for catalysis to occur (Robinson, 2015). The lower the value the higher the higher the affinity. The maximum velocity and k_{cat} give insight into the turnover of the protein which is the maximum

amount of substrate converted to product per active site of the protein per second, when the protein is saturated by substrate (Choi *et al.*, 2017). Additionally, the v_{max} signifies the rate of the reaction when the active site of a protein is saturated with substrate. The catalytic efficiency (k_{cat}/K_m) represents the specificity constant of an enzyme which is a measure of how proficient an enzyme is in converting substrate to product (Eisenthal *et al.*, 2007). The enzyme showed to have a v_{max} of 7.15×10^{-3} μmole·min^{-1} while the K_m is 2.94 μM, k_{cat} was 0.02 s^{-1} and the k_{cat}/K_m was 6122.45 M^{-1}·s^{-1}. The results suggest that the binding affinity of NMN to *Kp*NNAT, in the presence of Mg^{2+}, is low thus a high concentration of substrate is required to attain the v_{max}. Furthermore, the catalytic efficiency and K_m suggests that the enzyme is not effective in converting NMN into product. The K_m observed is far less than the ones reported in literature (Balducci *et al.*, 1995; Raffaelli *et al.*, 1999a; Raffaelli *et al.*, 1999b). It should be mentioned that a K_m value of the same enzyme across different species differs (Robinson, 2015). The low affinity for NMN by *Kp*NNAT is expected as bacterial NNAT have a higher preference for NaMN as opposed to NMN (Mehl *et al.*, 2000). The nicotinate ring of the substrate is involved in stacking interactions with tryptophan-117 and histidine-45 (Zhang *et al.*, 2002). A carboxylate group of the ring interacts with the amides of tyrosine-118 and threonine-85, the oxygen on the carboxylate group forms a hydrogen bond with water molecules which then interact with alanine-86 of *Ec*NNAT An anion binding pocket is attained from the conditions stated creates a suitable environment for NaMN binding as opposed to NMN binding (Magni *et al.*, 2004; Zhang *et al.*, 2002). The shape of the graph does affect the kinetic parameters obtained (Robinson, 2015). The rate of the reaction where the substrate saturates the active site of the protein is displayed as the v_{max} in Michaelis-Menten plot. This point is achieved at high substrate concentration though a plateau was achieved but future work should include increasing the number of injections to get a better plateau of the graph which may improve the validity of the results.

Chapter 7

Conclusion

The overexpression, purification and confirmation of *Kp*NNAT activity was successful. It is important to highlight that the study was based on the influence of metal ion, Ni^{2+} being one of the metals being studied, on the protein. With affinity chromatography the influence of Ni^{2+} on the histidine was detailed. Although, the protein was functional in the presence of the histidine tag thus suggesting that the tag had negligible effect on the function. The effect of the histidine tag on the function of the protein should not be completely ruled out. Future work can aim on the removal of the histidine tag, with thrombin cleavage. Exploration of other expression systems should be implemented if thrombin cleavage poses as a challenge. The pGEX expression system could be an alternate to the pET expression system. Although the purification protocol is cumbersome, three step purification, the vector construct is designed in a way that promotes the cleavage of the tag. SE-HPLC in tandem with dynamic light scattering (DLS) could be used in the prediction of the molecular weight of the protein. This technique couples the hydrodynamic volume of a protein (SE-HPLC) and considers the influence of the solution on the size of a molecule (DLS). This technique can improve the predicted molecular weight of the protein in solution. Alternative thermal stability studies can be used to monitor ATP binding, with mant-ATP as the fluorescent probe. Mant-ATP is specific in its binding compared to ANS hence monitoring its binding to the protein at increasing temperature will give insight onto the thermostability and can be used to corroborate the thermal shift assay results. Overall, this study was successful in identifying the preferred metal ion (Mg^{2+}) for *Kp*NNAT catalysis. Ni^{2+} induces conformational changes to the protein that does not favour ATP binding thus prevents maximum enzyme activity. A crystal structure of *Kp*NNAT, either apo or complexed with metal ion and substrate, would give insight on the binding site, conformation and catalysis of the enzyme. It would probe further studies aimed at docking the protein with ligands and this would give a clear understanding to the catalytic mechanism of the protein. So, it goes without saying that future work should aim at obtaining a crystal structure of the protein.

References

Abd El-Hamid El-Kady, R., Waggas, D., AkL, A., 2021. Microbial Repercussion on Hemodialysis Catheter-Related Bloodstream Infection Outcome: A 2-Year Retrospective Study. Infect Drug Resist 14, 4067-4075.

Allegranzi, B., Bagheri Nejad, S., Combescure, C., Graafmans, W., Attar, H., Donaldson, L., Pittet, D., 2011. Burden of endemic health-care-associated infection in developing countries: systematic review and meta-analysis. Lancet 377, 228-241.

Anthis, N.J., Clore, G.M., 2013. Sequence-specific determination of protein and peptide concentrations by absorbance at 205 nm. Protein Sci 22, 851-858.

Aquino Neto, S., Forti, J.C., Zucolotto, V., Ciancaglini, P., De Andrade, A.R., 2011. The kinetic behavior of dehydrogenase enzymes in solution and immobilized onto nanostructured carbon platforms. Process Biochemistry 46, 2347-2352.

Arakawa, T., Ejima, D., Li, T., Philo, J.S., 2010. The critical role of mobile phase composition in size exclusion chromatography of protein pharmaceuticals. Journal of Pharmaceutical Sciences 99, 1674-1692.

Aravind, L., Koonin, E.V., 1999. DNA polymerase beta-like nucleotidyltransferase superfamily: identification of three new families, classification and evolutionary history. Nucleic Acids Res 27, 1609-1618.

Babor, M., Greenblatt, H.M., Edelman, M., Sobolev, V., 2005. Flexibility of metal binding sites in proteins on a database scale. Proteins: Structure, Function, and Bioinformatics 59, 221-230.

Bagheri-Nejad, S., Allegranzi, B., Syed, S.B., Ellis, B., Pittet, D., 2011. Health-care-associated infection in Africa: a systematic review. Bull World Health Organ 89, 757-765.

Balducci, E., Orsomando, G., Polzonetti, V., Vita, A., Emanuelli, M., Raffaelli, N., Ruggieri, S., Magni, G., Natalini, P., 1995. NMN adenylyltransferase from bull testis: purification and properties. Biochem J 310 (Pt 2), 395-400.

Baneyx, F., 1999. Recombinant protein expression in Escherichia coli. Current Opinion in Biotechnology 10, 411-421.

Bartholomew, J.W., Mittwer, T., 1952. The Gram stain. Bacteriol Rev 16, 1-29.

Beggs, J.D., 1978. Transformation of yeast by a replicating hybrid plasmid. Nature 275, 104-109.

Benjwal, S., Verma, S., Röhm, K.-H., Gursky, O., 2006. Monitoring protein aggregation during thermal unfolding in circular dichroism experiments. Protein science : a publication of the Protein Society 15, 635-639.

Berger, F., Ramírez-Hernández, M.H., Ziegler, M., 2004. The new life of a centenarian: signalling functions of NAD(P). Trends Biochem Sci 29, 111-118.

Bicknell, R., Cullis, P.M., Jarvest, R.L., Lowe, G., 1982. The stereochemical course of nucleotidyl transfer catalyzed by ATP sulfurylase. J Biol Chem 257, 8922-8927.

Bisswanger, H., 2014. Enzyme assays. Perspectives in Science 1, 41-55.

Block, H., Maertens, B., Spriestersbach, A., Brinker, N., Kubicek, J., Fabis, R., Labahn, J., Schäfer, F., 2009. Chapter 27 Immobilized-Metal Affinity Chromatography (IMAC): A Review, in: Burgess, R.R., Deutscher, M.P. (Eds.), Methods Enzymol. Academic Press, pp. 439-473.

Bojer, M., Krogfelt, K.A., Struve, C., 2011. The newly discovered ClpK protein strongly promotes survival of Klebsiella pneumoniae biofilm subjected to heat shock. Journal of medical microbiology 60, 1559-1561.

Bojer, M.S., Struve, C., Ingmer, H., Krogfelt, K.A., 2013. ClpP-dependent and-independent activities encoded by the polycistronic clpK-encoding locus contribute to heat shock survival in Klebsiella pneumoniae. Research in microbiology 164, 205-210.

Bush, K., 2018. Past and present perspectives on β-lactamases. Antimicrobial agents and chemotherapy 62, e01076-01018.

Caselli, E., Brusaferro, S., Coccagna, M., Arnoldo, L., Berloco, F., Antonioli, P., Tarricone, R., Pelissero, G., Nola, S., La Fauci, V., Conte, A., Tognon, L., Villone, G., Trua, N., Mazzacane, S., for the,

S.A.N.I.C.A.S.G., 2018. Reducing healthcare-associated infections incidence by a probiotic-based sanitation system: A multicentre, prospective, intervention study. PLOS ONE 13, e0199616.
Chen, A.Y., Adamek, R.N., Dick, B.L., Credille, C.V., Morrison, C.N., Cohen, S.M., 2019. Targeting Metalloenzymes for Therapeutic Intervention. Chem Rev 119, 1323-1455.
Chi, S.Y., Kim, T.O., Park, C.W., Yu, J.Y., Lee, B., Lee, H.S., Kim, Y.I., Lim, S.C., Kwon, Y.S., 2012. Bacterial pathogens of ventilator associated pneumonia in a tertiary referral hospital. Tuberc Respir Dis (Seoul) 73, 32-37.
Choi, B., Rempala, G.A., Kim, J.K., 2017. Beyond the Michaelis-Menten equation: Accurate and efficient estimation of enzyme kinetic parameters. Sci Rep 7, 17018-17018.
Clark, J.J., Benson, M.L., Smith, R.D., Carlson, H.A., 2019. Inherent versus induced protein flexibility: Comparisons within and between apo and holo structures. PLOS Computational Biology 15, e1006705.
Contreras-Rodríguez, L.E., Marin-Mogollon, C.Y., Sánchez-Mejía, L.M., Ramírez-Hernández, M.H., 2018. Structural insights into Plasmodium falciparum nicotinamide mononucleotide adenylyltransferase: oligomeric assembly. Mem Inst Oswaldo Cruz 113, e180073-e180073.
D'Angelo, I., Raffaelli, N., Dabusti, V., Lorenzi, T., Magni, G., Rizzi, M., 2000. Structure of nicotinamide mononucleotide adenylyltransferase: a key enzyme in NAD+ biosynthesis. Structure 8, 993-1004.
Davis, B.J., 1964. DISC ELECTROPHORESIS. II. METHOD AND APPLICATION TO HUMAN SERUM PROTEINS. Ann N Y Acad Sci 121, 404-427.
Daya, T., Jeje, O., Maake, R., Aloke, C., Khoza, T., Achilonu, I., 2022. Expression, Purification, and Biophysical Characterization of Klebsiella Pneumoniae Nicotinate Nucleotide Adenylyltransferase. The Protein Journal.
Di Trani, J.M., De Cesco, S., O'Leary, R., Plescia, J., do Nascimento, C.J., Moitessier, N., Mittermaier, A.K., 2018. Rapid measurement of inhibitor binding kinetics by isothermal titration calorimetry. Nature Communications 9, 893.
Du, X., Li, Y., Xia, Y.-L., Ai, S.-M., Liang, J., Sang, P., Ji, X.-L., Liu, S.-Q., 2016. Insights into Protein-Ligand Interactions: Mechanisms, Models, and Methods. Int J Mol Sci 17, 144.
Ducel, G., Fabry, J., Nicolle, L., 2002. Prevention of hospital acquired infections: a practical guide. Prevention of hospital acquired infections: a practical guide.
Dutta, A.K., Rösgen, J., Rajarathnam, K., 2015. Using isothermal titration calorimetry to determine thermodynamic parameters of protein-glycosaminoglycan interactions. Methods Mol Biol 1229, 315-324.
Eisenthal, R., Danson, M.J., Hough, D.W., 2007. Catalytic efficiency and kcat/KM: a useful comparator? Trends in Biotechnology 25, 247-249.
El-Mahallawy, H.A., Hassan, S.S., El-Wakil, M., Moneer, M.M., 2016. Bacteremia due to ESKAPE pathogens: An emerging problem in cancer patients. Journal of the Egyptian National Cancer Institute 28, 157-162.
Ferreira, R.L., da Silva, B.C.M., Rezende, G.S., Nakamura-Silva, R., Pitondo-Silva, A., Campanini, E.B., Brito, M.C.A., da Silva, E.M.L., Freire, C.C.d.M., Cunha, A.F.d., Pranchevicius, M.-C.d.S., 2019. High Prevalence of Multidrug-Resistant Klebsiella pneumoniae Harboring Several Virulence and β-Lactamase Encoding Genes in a Brazilian Intensive Care Unit. Frontiers in Microbiology 9.
Frank, H.S., Evans, M.W., 1945. Free volume and entropy in condensed systems III. Entropy in binary liquid mixtures; partial molal entropy in dilute solutions; structure and thermodynamics in aqueous electrolytes. The Journal of chemical physics 13, 507-532.
Freire, E., Mayorga, O.L., Straume, M., 1990. Isothermal titration calorimetry. Analytical chemistry 62, 950A-959A.
Freyer, M.W., Lewis, E.A., 2008. Isothermal Titration Calorimetry: Experimental Design, Data Analysis, and Probing Macromolecule/Ligand Binding and Kinetic Interactions, Methods in Cell Biology. Academic Press, pp. 79-113.
Gallagher, S., 1998. Quantitation of Nucleic Acids with Absorption Spectroscopy. Current Protocols in Protein Science 13, A.4K.1-A.4K.3.

Gasteiger, E., Gattiker, A., Hoogland, C., Ivanyi, I., Appel, R.D., Bairoch, A., 2003. ExPASy: the proteomics server for in-depth protein knowledge and analysis. Nucleic acids research 31, 3784-3788.
Gasymov, O.K., Glasgow, B.J., 2007. ANS fluorescence: potential to augment the identification of the external binding sites of proteins. Biochim Biophys Acta 1774, 403-411.
Gazzaniga, F., Stebbins, R., Chang, S.Z., McPeek, M.A., Brenner, C., 2009. Microbial NAD metabolism: lessons from comparative genomics. Microbiol Mol Biol Rev 73, 529-541, Table of Contents.
Ge, X., Chen, L., Li, D., Liu, R., Ge, G., 2021. Estimation of non-constant variance in isothermal titration calorimetry using an ITC measurement model. PLOS ONE 15, e0244739.
Glover, S.D., Tommos, C., 2019. A Quick and Colorful Method to Measure Low-Level Contaminations of Paramagnetic Ni(2+) in Protein Samples Purified by Immobilized Metal Ion Affinity Chromatography. Methods Enzymol 614, 87-106.
Goh, S., Good, L., 2008. Plasmid selection in Escherichia coli using an endogenous essential gene marker. BMC Biotechnology 8, 61.
Greenfield, N.J., 2006. Using circular dichroism spectra to estimate protein secondary structure. Nat Protoc 1, 2876-2890.
Gromiha, M.M., 2010. Chapter 1 - Proteins, in: Gromiha, M.M. (Ed.), Protein Bioinformatics. Academic Press, Singapore, pp. 1-27.
Hassoun, A., Linden, P.K., Friedman, B., 2017. Incidence, prevalence, and management of MRSA bacteremia across patient populations-a review of recent developments in MRSA management and treatment. Crit Care 21, 211-211.
Hatch, J.P., Prihoda, T.J., 1992. The effect of influential outliers on parameter estimation in regression analysis. Biofeedback and Self-regulation 17, 153-156.
Herceg, Z., Wang, Z.-Q., 2001. Functions of poly(ADP-ribose) polymerase (PARP) in DNA repair, genomic integrity and cell death. Mutation Research/Fundamental and Molecular Mechanisms of Mutagenesis 477, 97-110.
Heux, S., Cachon, R., Dequin, S., 2006. Cofactor engineering in Saccharomyces cerevisiae: Expression of a H2O-forming NADH oxidase and impact on redox metabolism. Metabolic Engineering 8, 303-314.
Hinnen, A., Hicks, J.B., Fink, G.R., 1978. Transformation of yeast. Proceedings of the National Academy of Sciences 75, 1929-1933.
Hochuli, E., Döbeli, H., Schacher, A., 1987. New metal chelate adsorbent selective for proteins and peptides containing neighbouring histidine residues. J Chromatogr 411, 177-184.
Holdgate, G.A., 2017. 2.07 - Kinetics, Thermodynamics, and Ligand Efficiency Metrics in Drug Discovery, in: Chackalamannil, S., Rotella, D., Ward, S.E. (Eds.), Comprehensive Medicinal Chemistry III. Elsevier, Oxford, pp. 180-211.
Hong, P., Koza, S., Bouvier, E.S.P., 2012. Size-Exclusion Chromatography for the Analysis of Protein Biotherapeutics and their Aggregates. J Liq Chromatogr Relat Technol 35, 2923-2950.
Hoskins, J.R., Sharma, S., Sathyanarayana, B.K., Wickner, S., 2001. Clp ATPases and their role in protein unfolding and degradation. Advances in Protein Chemistry 59, 413-429.
Huang, N., Kolhatkar, R., Eyobo, Y., Sorci, L., Rodionova, I., Osterman, A.L., MacKerell, A.D., Zhang, H., 2010. Complexes of Bacterial Nicotinate Mononucleotide Adenylyltransferase with Inhibitors: Implication for Structure-Based Drug Design and Improvement. Journal of Medicinal Chemistry 53, 5229-5239.
Hughes, K.T., Ladika, D., Roth, J.R., Olivera, B.M., 1983. An indispensable gene for NAD biosynthesis in Salmonella typhimurium. Journal of Bacteriology 155, 213-221.
Hunter, J., 2006. Ventilator associated pneumonia. Postgraduate medical journal 82, 172-178.
Hunter, J.D., 2012. Ventilator associated pneumonia. Bmj 344.
Jeje, O., Maake, R., van Deventer, R., Esau, V., Iwuchukwu, E.A., Meyer, V., Khoza, T., Achilonu, I., 2022. Effect of Divalent Metal Ion on the Structure, Stability and Function of Klebsiella pneumoniae Nicotinate-Nucleotide Adenylyltransferase: Empirical and Computational Studies. International Journal of Molecular Sciences 23, 116.

Jørgensen, S.B., Bojer, M.S., Boll, E.J., Martin, Y., Helmersen, K., Skogstad, M., Struve, C., 2016. Heat-resistant, extended-spectrum β-lactamase-producing Klebsiella pneumoniae in endoscope-mediated outbreak. Journal of Hospital Infection 93, 57-62.
Kelly, S.M., Jess, T.J., Price, N.C., 2005. How to study proteins by circular dichroism. Biochimica et Biophysica Acta (BBA)-Proteins and Proteomics 1751, 119-139.
Khan, H.A., Baig, F.K., Mehboob, R., 2017. Nosocomial infections: Epidemiology, prevention, control and surveillance. Asian Pacific Journal of Tropical Biomedicine 7, 478-482.
Koenig, S.M., Truwit, J.D., 2006. Ventilator-associated pneumonia: diagnosis, treatment, and prevention. Clinical microbiology reviews 19, 637-657.
Kopaciewicz, W., Regnier, F.E., 1982. Nonideal size-exclusion chromatography of proteins: Effects of pH at low ionic strength. Analytical Biochemistry 126, 8-16.
Kuchta, K., Knizewski, L., Wyrwicz, L.S., Rychlewski, L., Ginalski, K., 2009. Comprehensive classification of nucleotidyltransferase fold proteins: identification of novel families and their representatives in human. Nucleic Acids Res 37, 7701-7714.
Kumar, A., Singh, M., Bhatia, P., Singh, A., 2019. Audit of Quality and Quantity of Nucleic Acid Yield from Pediatric Acute Leukemia Cases Following a Bio-banking Initiative. Indian J Hematol Blood Transfus 35, 77-82.
Kumar Panigrahi, S., Kumar Mishra, A., 2019. Inner filter effect in fluorescence spectroscopy: As a problem and as a solution. Journal of Photochemistry and Photobiology C: Photochemistry Reviews 41, 100318.
Kumar, S., Tsai, C.J., Nussinov, R., 2000. Factors enhancing protein thermostability. Protein Eng 13, 179-191.
Laemmli, U.K., 1970. Cleavage of structural proteins during the assembly of the head of bacteriophage T4. Nature 227, 680-685.
Laity, J.H., Lee, B.M., Wright, P.E., 2001. Zinc finger proteins: new insights into structural and functional diversity. Curr Opin Struct Biol 11, 39-46.
Lau, C., Niere, M., Ziegler, M., 2009. The NMN/NaMN adenylyltransferase (NMNAT) protein family. Front Biosci 14, 410-431.
Laurino, P., Toth-Petroczy, A., Meana-Pañeda, R., Lin, W., Truhlar, D., Tawfik, D., 2016. An Ancient Fingerprint Indicates the Common Ancestry of Rossmann-Fold Enzymes Utilizing Different Ribose-Based Cofactors. PLOS Biology 14, e1002396.
Lee, C.-H., Su, L.-H., Tang, Y.-F., Liu, J.-W., 2006. Treatment of ESBL-producing Klebsiella pneumoniae bacteraemia with carbapenems or flomoxef: a retrospective study and laboratory analysis of the isolates. Journal of Antimicrobial Chemotherapy 58, 1074-1077.
Leskovar, A., Reinstein, J., 2008. Photophysical properties of popular fluorescent adenosine nucleotide analogs used in enzyme mechanism probing. Archives of Biochemistry and Biophysics 473, 16-24.
Liang, Y., 2008. Applications of isothermal titration calorimetry in protein science. Acta Biochimica et Biophysica Sinica 40, 565-576.
Lin, D.M., Koskella, B., Lin, H.C., 2017. Phage therapy: An alternative to antibiotics in the age of multi-drug resistance. World J Gastrointest Pharmacol Ther 8, 162-173.
Lobdell, K.W., Stamou, S., Sanchez, J.A., 2012. Hospital-acquired infections. Surgical Clinics 92, 65-77.
Lowe, G., Tansley, G., 1983. The Stereochemical Course of Nucleotidyl Transfer Catalysed by NAD Pyrophosphorylase. European Journal of Biochemistry 132, 117-120.
Lucena-Aguilar, G., Sánchez-López, A.M., Barberán-Aceituno, C., Carrillo-Ávila, J.A., López-Guerrero, J.A., Aguilar-Quesada, R., 2016. DNA Source Selection for Downstream Applications Based on DNA Quality Indicators Analysis. Biopreserv Biobank 14, 264-270.
Magni, G., Amici, A., Emanuelli, M., Orsomando, G., Raffaelli, N., Ruggieri, S., 2004. Structure and Function of Nicotinamide Mononucleotide Adenylyltransferase. Current Medicinal Chemistry 11, 873-885.

Maki, D.G., Kluger, D.M., Crnich, C.J., 2006. The risk of bloodstream infection in adults with different intravascular devices: a systematic review of 200 published prospective studies, Mayo Clinic Proceedings. Elsevier, pp. 1159-1171.
Maki, D.G., Tambyah, P.A., 2001. Engineering out the risk for infection with urinary catheters. Emerg Infect Dis 7, 342-347.
Medina, C., Santos-Martinez, M.J., Radomski, A., Corrigan, O.I., Radomski, M.W., 2007. Nanoparticles: pharmacological and toxicological significance. Br J Pharmacol 150, 552-558.
Mehl, R.A., Kinsland, C., Begley, T.P., 2000. Identification of the Escherichia coli nicotinic acid mononucleotide adenylyltransferase gene. J Bacteriol 182, 4372-4374.
Mendonça, A., Rocha, A.C., Duarte, A.C., Santos, E.B., 2013. The inner filter effects and their correction in fluorescence spectra of salt marsh humic matter. Anal Chim Acta 788, 99-107.
Micsonai, A., Wien, F., Kernya, L., Lee, Y.-H., Goto, Y., Réfrégiers, M., Kardos, J., 2015. Accurate secondary structure prediction and fold recognition for circular dichroism spectroscopy. Proceedings of the National Academy of Sciences 112, E3095-E3103.
Mierendorf, R.C., Morris, B.B., Hammer, B., Novy, R.E., 1998. Expression and Purification of Recombinant Proteins Using the pET System. Methods Mol Med 13, 257-292.
Miles, A.J., Wallace, B.A., 2016. Circular dichroism spectroscopy of membrane proteins. Chemical Society Reviews 45, 4859-4872.
Miller, W.R., Munita, J.M., Arias, C.A., 2014. Mechanisms of antibiotic resistance in enterococci. Expert Rev Anti Infect Ther 12, 1221-1236.
Monegro, A.F., Muppidi, V., Regunath, H., 2020. Hospital acquired infections. Statpearls [Internet].
Mulani, M.S., Kamble, E.E., Kumkar, S.N., Tawre, M.S., Pardesi, K.R., 2019. Emerging Strategies to Combat ESKAPE Pathogens in the Era of Antimicrobial Resistance: A Review. Frontiers in Microbiology 10.
Nieborak, A., Schneider, R., 2018. Metabolic intermediates - Cellular messengers talking to chromatin modifiers. Molecular Metabolism 14.
Nikiforov, A., Kulikova, V., Ziegler, M., 2015. The human NAD metabolome: Functions, metabolism and compartmentalization. 50, 284-297.
Nordmann, P., Cuzon, G., Naas, T., 2009. The real threat of Klebsiella pneumoniae carbapenemase-producing bacteria. The Lancet. Infectious diseases 9, 228-236.
Nowakowski, A.B., Wobig, W.J., Petering, D.H., 2014. Native SDS-PAGE: high resolution electrophoretic separation of proteins with retention of native properties including bound metal ions. Metallomics 6, 1068-1078.
Nowick, J.S., 2008. Exploring beta-sheet structure and interactions with chemical model systems. Acc Chem Res 41, 1319-1330.
Oliveira, J., Reygaert, W.C., 2022. Gram Negative Bacteria, StatPearls. StatPearls Publishing

Ornstein, L., 1964. DISC ELECTROPHORESIS. I. BACKGROUND AND THEORY. Ann N Y Acad Sci 121, 321-349.
Ortega, J., Lee, H.S., Maurizi, M.R., Steven, A.C., 2004. ClpA and ClpX ATPases bind simultaneously to opposite ends of ClpP peptidase to form active hybrid complexes. Journal of Structural Biology 146, 217-226.
Oshinbolu, S., Shah, R., Finka, G., Molloy, M., Uden, M., Bracewell, D.G., 2018. Evaluation of fluorescent dyes to measure protein aggregation within mammalian cell culture supernatants. J Chem Technol Biotechnol 93, 909-917.
Owens, C.D., Stoessel, K., 2008. Surgical site infections: epidemiology, microbiology and prevention. Journal of Hospital Infection 70, 3-10.
Pandey, N., Cascella, M., 2022. Beta Lactam Antibiotics, StatPearls. StatPearls Publishing

Papazian, L., Klompas, M., Luyt, C.-E., 2020. Ventilator-associated pneumonia in adults: a narrative review. Intensive Care Med 46, 888-906.
Parsell, D.A., Kowal, A.S., Singer, M.A., Lindquist, S., 1994. Protein disaggregation mediated by heat-shock protein Hspl04. Nature 372, 475-478.
Perrin, K., Vats, A., Qureshi, A., Hester, J., Larson, A., Felipe, A., Sleiman, A., Baron-Lee, J., Busl, K., 2021. Catheter-Associated Urinary Tract Infection (CAUTI) in the NeuroICU: Identification of Risk Factors and Time-to-CAUTI Using a Case-Control Design. Neurocrit Care 34, 271-278.
Pitt-Rivers, R., Impiombato, F.S.A., 1968. The binding of sodium dodecyl sulphate to various proteins. Biochemical Journal 109, 825-830.
Porath, J., Carlsson, J., Olsson, I., Belfrage, G., 1975. Metal chelate affinity chromatography, a new approach to protein fractionation. Nature 258, 598-599.
Prasad, S., Mandal, I., Singh, S., Paul, A., Mandal, B., Venkatramani, R., Swaminathan, R., 2017. Near UV-Visible electronic absorption originating from charged amino acids in a monomeric protein. Chem Sci 8, 5416-5433.
Prelich, G., 2012. Gene overexpression: uses, mechanisms, and interpretation. Genetics 190, 841-854.
Provencher, S.W., Gloeckner, J., 1981. Estimation of globular protein secondary structure from circular dichroism. Biochemistry 20, 33-37.
Raffaelli, N., Lorenzi, T., Amici, A., Emanuelli, M., Ruggieri, S., Magni, G., 1999a. Synechocystis sp. slr0787 protein is a novel bifunctional enzyme endowed with both nicotinamide mononucleotide adenylyltransferase and 'Nudix' hydrolase activities. FEBS Letters 444, 222-226.
Raffaelli, N., Lorenzi, T., Mariani, P.L., Emanuelli, M., Amici, A., Ruggieri, S., Magni, G., 1999b. The Escherichia coli NadR regulator is endowed with nicotinamide mononucleotide adenylyltransferase activity. Journal of bacteriology 181, 5509-5511.
Raffaelli, N., Sorci, L., Amici, A., Emanuelli, M., Mazzola, F., Magni, G., 2002. Identification of a novel human nicotinamide mononucleotide adenylyltransferase. Biochemical and Biophysical Research Communications 297, 835-840.
Raj, S.B., Ramaswamy, S., Plapp, B.V., 2014. Yeast alcohol dehydrogenase structure and catalysis. Biochemistry 53, 5791-5803.
Rana, H., Moussatche, P., Rocha, L.S., Abdellaoui, S., Minteer, S.D., Moomaw, E.W., 2016. Isothermal titration calorimetry uncovers substrate promiscuity of bicupin oxalate oxidase from Ceriporiopsis subvermispora. Biochemistry and Biophysics Reports 5, 396-400.
Rath, A., Glibowicka, M., Nadeau, V.G., Chen, G., Deber, C.M., 2009. Detergent binding explains anomalous SDS-PAGE migration of membrane proteins. Proceedings of the National Academy of Sciences 106, 1760-1765.
Rehman, I., Farooq, M., Botelho, S., 2022. Biochemistry, Secondary Protein Structure, StatPearls. StatPearls Publishing

Reynolds, J.A., Tanford, C., 1970. Binding of dodecyl sulfate to proteins at high binding ratios. Possible implications for the state of proteins in biological membranes. Proc Natl Acad Sci U S A 66, 1002-1007.
Rice, L.B., 2008. Federal funding for the study of antimicrobial resistance in nosocomial pathogens: no ESKAPE. The University of Chicago Press, pp. 1079-1081.
Rizzi, M., Schindelin, H., 2002. Structural biology of enzymes involved in NAD and molybdenum cofactor biosynthesis. Current Opinion in Structural Biology 12, 709-720.
Robinson, P.K., 2015. Enzymes: principles and biotechnological applications. Essays Biochem 59, 1-41.
Rosano, G.L., Ceccarelli, E.A., 2014. Recombinant protein expression in Escherichia coli: advances and challenges. Frontiers in Microbiology 5.
Rothe, C., Schlaich, C., Thompson, S., 2013. Healthcare-associated infections in sub-Saharan Africa. J Hosp Infect 85, 257-267.
Roussin, M., Salcedo, S.P., 2021. NAD+-targeting by bacteria: an emerging weapon in pathogenesis. FEMS Microbiology Reviews.

Saleem, Z., Godman, B., Azhar, F., Kalungia, A.C., Fadare, J., Opanga, S., Markovic-Pekovic, V., Hoxha, I., Saeed, A., Al-Gethamy, M., Haseeb, A., Salman, M., Khan, A.A., Nadeem, M.U., Rehman, I.U., Qamar, M.U., Amir, A., Ikram, A., Hassali, M.A., 2022. Progress on the national action plan of Pakistan on antimicrobial resistance (AMR): a narrative review and the implications. Expert Review of Anti-infective Therapy 20, 71-93.
Santajit, S., Indrawattana, N., 2016. Mechanisms of Antimicrobial Resistance in ESKAPE Pathogens. Biomed Res Int 2016, 2475067-2475067.
Santos, A.R.S., Gerhardt, E.C.M., Parize, E., Pedrosa, F.O., Steffens, M.B.R., Chubatsu, L.S., Souza, E.M., Passaglia, L.M.P., Sant'Anna, F.H., de Souza, G.A., Huergo, L.F., Forchhammer, K., 2020. NAD(+) biosynthesis in bacteria is controlled by global carbon/nitrogen levels via PII signaling. J Biol Chem 295, 6165-6176.
Saridakis, V., Pai, E.F., 2003. Mutational, structural, and kinetic studies of the ATP-binding site of Methanobacterium thermoautotrophicum nicotinamide mononucleotide adenylyltransferase. J Biol Chem 278, 34356-34363.
Scherbaum, M., Kösters, K., Mürbeth, R.E., Ngoa, U.A., Kremsner, P.G., Lell, B., Alabi, A., 2014. Incidence, pathogens and resistance patterns of nosocomial infections at a rural hospital in Gabon. BMC Infectious Diseases 14, 124.
Schiebel, J., Gaspari, R., Wulsdorf, T., Ngo, K., Sohn, C., Schrader, T.E., Cavalli, A., Ostermann, A., Heine, A., Klebe, G., 2018. Intriguing role of water in protein-ligand binding studied by neutron crystallography on trypsin complexes. Nat Commun 9, 3559-3559.
Schmid, F.-X., 2001. Biological Macromolecules: UV-visible Spectrophotometry, eLS.
Scopes, R.K., 2001. Enzyme Activity and Assays, eLS.
Sershon, V.C., Santarsiero, B.D., Mesecar, A.D., 2009. Kinetic and X-Ray Structural Evidence for Negative Cooperativity in Substrate Binding to Nicotinate Mononucleotide Adenylyltransferase (NMAT) from Bacillus anthracis. Journal of Molecular Biology 385, 867-888.
Sezonov, G., Joseleau-Petit, D., D'Ari, R., 2007. Escherichia coli Physiology in Luria-Bertani Broth. Journal of Bacteriology 189, 8746-8749.
Shapiro, A.L., Maizel, J.V., Jr., 1969. Molecular weight estimation of polypeptides by SDS-polyacrylamide gel electrophoresis: further data concerning resolving power and general considerations. Anal Biochem 29, 505-514.
Shilling, P.J., Mirzadeh, K., Cumming, A.J., Widesheim, M., Köck, Z., Daley, D.O., 2020. Improved designs for pET expression plasmids increase protein production yield in Escherichia coli. Communications Biology 3, 214.
Sizar, O., Unakal, C.G., 2022. Gram Positive Bacteria, StatPearls. StatPearls Publishing

Copyright © 2022, StatPearls Publishing LLC., Treasure Island (FL).
Soltani, S., Hammami, R., Cotter, P.D., Rebuffat, S., Said, L.B., Gaudreau, H., Bédard, F., Biron, E., Drider, D., Fliss, I., 2021. Bacteriocins as a new generation of antimicrobials: toxicity aspects and regulations. FEMS Microbiology Reviews 45, fuaa039.
Sorci, L., Cimadamore, F., Scotti, S., Petrelli, R., Cappellacci, L., Franchetti, P., Orsomando, G., Magni, G., 2007. Initial-Rate Kinetics of Human NMN-Adenylyltransferases: Substrate and Metal Ion Specificity, Inhibition by Products and Multisubstrate Analogues, and Isozyme Contributions to NAD+ Biosynthesis. Biochemistry 46, 4912-4922.
Sørensen, H.P., Mortensen, K.K., 2005. Advanced genetic strategies for recombinant protein expression in Escherichia coli. J Biotechnol 115, 113-128.
Sreerama, N., Woody, R.W., 2000. Estimation of protein secondary structure from circular dichroism spectra: comparison of CONTIN, SELCON, and CDSSTR methods with an expanded reference set. Anal Biochem 287, 252-260.
Srivastava, V.K., Yadav, R., 2019. Chapter 9 - Isothermal titration calorimetry, in: Misra, G. (Ed.), Data Processing Handbook for Complex Biological Data Sources. Academic Press, pp. 125-137.
Stancek, M., Schnell, R., Rydén-Aulin, M., 2005a. Analysis of Escherichia coli nicotinate mononucleotide adenylyltransferase mutants in vivo and in vitro. BMC Biochemistry 6, 16.

Stancek, M., Schnell, R., Rydén-Aulin, M., 2005b. Analysis of Escherichia coli nicotinate mononucleotide adenylyltransferase mutants in vivo and in vitro. BMC biochemistry 6, 16.
Stiller, A., Schröder, C., Gropmann, A., Schwab, F., Behnke, M., Geffers, C., Sunder, W., Holzhausen, J., Gastmeier, P., 2017. ICU ward design and nosocomial infection rates: a cross-sectional study in Germany. J Hosp Infect 95, 71-75.
Szulc, A., Appelhans, D., Voit, B., Bryszewska, M., Klajnert, B., 2013. Studying Complexes Between PPI Dendrimers and Mant-ATP. Journal of Fluorescence 23, 349-356.
Tamma, P.D., Cosgrove, S.E., Maragakis, L.L., 2012. Combination therapy for treatment of infections with gram-negative bacteria. Clin Microbiol Rev 25, 450-470.
Tanford, C., 1980. The hydrophobic effect: formation of micelles and biological membranes 2d ed. J. Wiley.
Teklu, D.S., Negeri, A.A., Legese, M.H., Bedada, T.L., Woldemariam, H.K., Tullu, K.D., 2019. Extended-spectrum beta-lactamase production and multi-drug resistance among Enterobacteriaceae isolated in Addis Ababa, Ethiopia. Antimicrobial Resistance & Infection Control 8, 39.
Todd, M.J., Gomez, J., 2001. Enzyme kinetics determined using calorimetry: a general assay for enzyme activity? Analytical biochemistry 296, 179-187.
Tripathi, N., Sapra, A., 2022. Gram Staining, StatPearls. StatPearls Publishing

Tripathi, N.K., Shrivastava, A., 2019. Recent Developments in Bioprocessing of Recombinant Proteins: Expression Hosts and Process Development. Frontiers in Bioengineering and Biotechnology 7.
Valenti, L., De Pauli, C., Giacomelli, C., 2006. The binding of Ni(II) ions to hexahistidine as a model system of the interaction between nickel and His-tagged proteins. Journal of inorganic biochemistry 100, 192-200.
Vihinen, M., 1987. Relationship of protein flexibility to thermostability. Protein Eng 1, 477-480.
Vivas, R., Barbosa, A.A.T., Dolabela, S.S., Jain, S., 2019. Multidrug-Resistant Bacteria and Alternative Methods to Control Them: An Overview. Microbial Drug Resistance 25, 890-908.
Vogt, G., Woell, S., Argos, P., 1997. Protein thermal stability, hydrogen bonds, and ion pairs11Edited by F. E. Cohen. Journal of Molecular Biology 269, 631-643.
Walker, J.R.L., 1992. Spectrophotometric determination of enzyme activity: Alcohol dehydrogenase (ADH). Biochemical Education 20, 42-43.
Wang, J.-T., Chang, S.-C., Wang, H.-Y., Chen, P.-C., Shiau, Y.-R., Lauderdale, T.-L., 2013. High rates of multidrug resistance in Enterococcus faecalis and E. faecium isolated from inpatients and outpatients in Taiwan. Diagnostic Microbiology and Infectious Disease 75, 406-411.
Wang, L., Berne, B.J., Friesner, R.A., 2011. Ligand binding to protein-binding pockets with wet and dry regions. Proc Natl Acad Sci U S A 108, 1326-1330.
Wang, Y., Wang, G., Moitessier, N., Mittermaier, A.K., 2020a. Enzyme Kinetics by Isothermal Titration Calorimetry: Allostery, Inhibition, and Dynamics. Frontiers in Molecular Biosciences 7.
Wang, Y., Wang, G., Moitessier, N., Mittermaier, A.K., 2020b. Enzyme Kinetics by Isothermal Titration Calorimetry: Allostery, Inhibition, and Dynamics. Frontiers in Molecular Biosciences 7.
Wangler, M., Bellen, H., 2017. In Vivo Animal Modeling, pp. 211-234.
Wen, Y.-W., Tsai, Y.-W., Wu, D.B.-C., Chen, P.-F., 2013. The Impact of Outliers on Net-Benefit Regression Model in Cost-Effectiveness Analysis. PLoS One 8, e65930-e65930.
Whitmore, L., Wallace, B.A., 2004. DICHROWEB, an online server for protein secondary structure analyses from circular dichroism spectroscopic data. Nucleic Acids Res 32, W668-W673.
Wilkinson, A., Day, J., Bowater, R., 2001. Bacterial DNA ligases. Molecular Microbiology 40, 1241-1248.
Wiseman, T., Williston, S., Brandts, J.F., Lin, L.N., 1989. Rapid measurement of binding constants and heats of binding using a new titration calorimeter. Anal Biochem 179, 131-137.
Worth, L.J., Brett, J., Bull, A.L., McBryde, E.S., Russo, P.L., Richards, M.J., 2009. Impact of revising the National Nosocomial Infection Surveillance System definition for catheter-related bloodstream

infection in ICU: reproducibility of the National Healthcare Safety Network case definition in an Australian cohort of infection control professionals. American journal of infection control 37, 643-648.
Worthington, R.J., Melander, C., 2013. Combination approaches to combat multidrug-resistant bacteria. Trends Biotechnol 31, 177-184.
Young, T., Abel, R., Kim, B., Berne, B.J., Friesner, R.A., 2007. Motifs for molecular recognition exploiting hydrophobic enclosure in protein–ligand binding. Proceedings of the National Academy of Sciences 104, 808-813.
Zaidi, A.K., Huskins, W.C., Thaver, D., Bhutta, Z.A., Abbas, Z., Goldmann, D.A., 2005. Hospital-acquired neonatal infections in developing countries. The Lancet 365, 1175-1188.
Zeng, X., Lin, J., 2013. Beta-lactamase induction and cell wall metabolism in Gram-negative bacteria. Frontiers in Microbiology 4.
Zhang, H., Zhou, T., Kurnasov, O., Cheek, S., Grishin, N.V., Osterman, A., 2002. Crystal structures of E. coli nicotinate mononucleotide adenylyltransferase and its complex with deamido-NAD. Structure 10, 69-79.
Ziegler, M., 2000. New functions of a long-known molecule. Emerging roles of NAD in cellular signaling. Eur J Biochem 267, 1550-1564.

Supplementary Data

Calculation of Protein concentration

$$Protein\ concentration\ = \frac{Slope \times Molecular\ weigth\ (daltons)}{Molar\ extinction\ coefficient}$$

$$= \frac{8.32 \times 24900\ Da}{38\ 055\ M^{-1} \cdot cm^{-1}}$$

$$= 5.44\ mg \cdot mL^{-1}$$

Calculation of ΔH_{app} for ITC Kinetics

$$\Delta H_{app} = \frac{1}{[S] * v} * Integrated\ peak$$

where v is the total volume, and [S] substrate concentration.

$$\Delta H_{app} = \frac{1}{[0.2 * 10^{-3}\text{mol}.L^{-1}] * (9.6473 * 10^{-4}L)} * (195.7 * 10^{-6}J)$$

$$\Delta H = -1014 J.mol^{-1}$$

$$OR$$

$$\Delta H = -1.014\ \text{kJ}.mol^{-1}\ or\ J.mmol^{-1}.$$

Conversions:

- v = 950 µL+ (4.91 µL Injection volume × 3 number of injections) = 964.73 µL
  Convert to L = 964.73 × 10^{-6} L = $9.6473 \times 10^{-4} L$
- [S] = 0.2 mM convert to M = 0.2 × 10^{-3} M or 0.2 × 10^{-3} mole·L^{-1}
- $Integrated\ peak$ -195.7 µJ convert to J = 195.7 × 10^{-6} J

Calculation of Kinetic parameters

$$k_2 = \frac{v_{max}}{[E_T]}$$

$k_2 = k_{cat}$

$$k_{cat} = \frac{v_{max}}{[E_T]}$$

$$k_{cat} = \frac{0.0007135\ mM \cdot s^{-1}}{0.04\ mM}$$

$$k_{cat} = 0.018\ s^{-1}$$

$$\frac{k_{cat}}{K_m} = \frac{0.018\ s^{-1}}{0.00000294\ M}$$

$$\frac{k_{cat}}{K_m} = 6122.45\ M^{-1} \cdot s^{-1}$$

Conversions:

$$M \cdot s^{-1} = \frac{v_{max} \times 60}{10^6 \times (V \times 10^{-3})}$$

where V is the total reaction volume.

$$M \cdot s^{-1} = \frac{0.01201\ \mu mole \cdot min^{-1} \times 60}{10^6 \times (1010 \times 10^{-3} L)}$$

$$= 0.0000007134$$

$$mM \cdot s^{-1} = 0.0000007135\ M \cdot s^{-1} \times 10^3$$

$$= 0.0007135$$

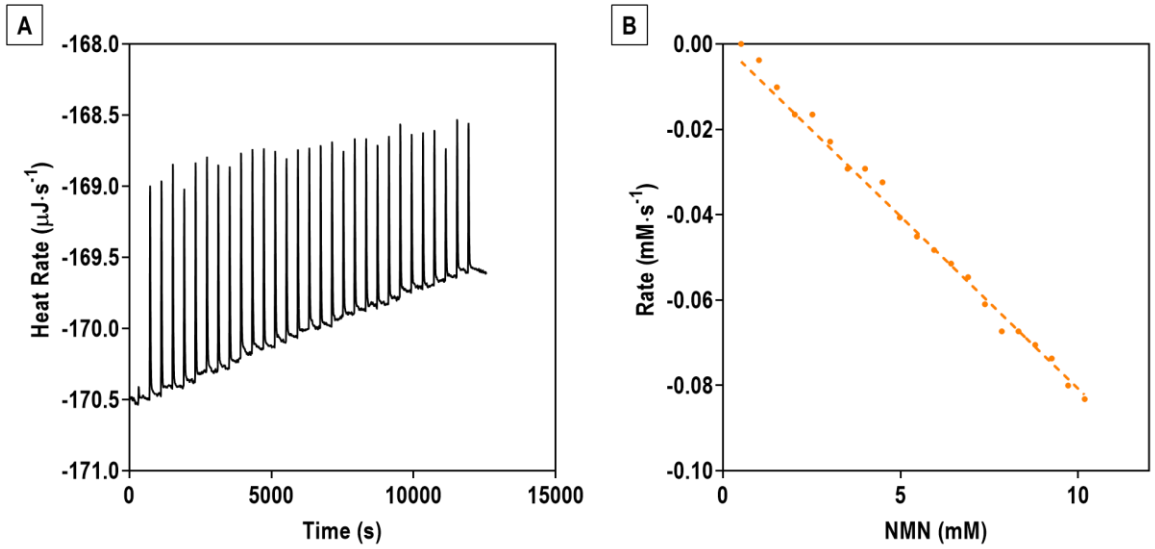

Figure S.1. Isothermal titration calorimetry for the determination of the kinetics of *Kp*NNAT. (A) A thermogram achieved from the multiple injection method of *Kp*NNAT in the absence of metal ion. (B) The resulting enzyme kinetics plot. It is supposed to resemble the Michaelis-Menten kinetics but instead shows a negative linear plot of the rate ($mM \cdot s^{-1}$) against substrate concentration (mM).

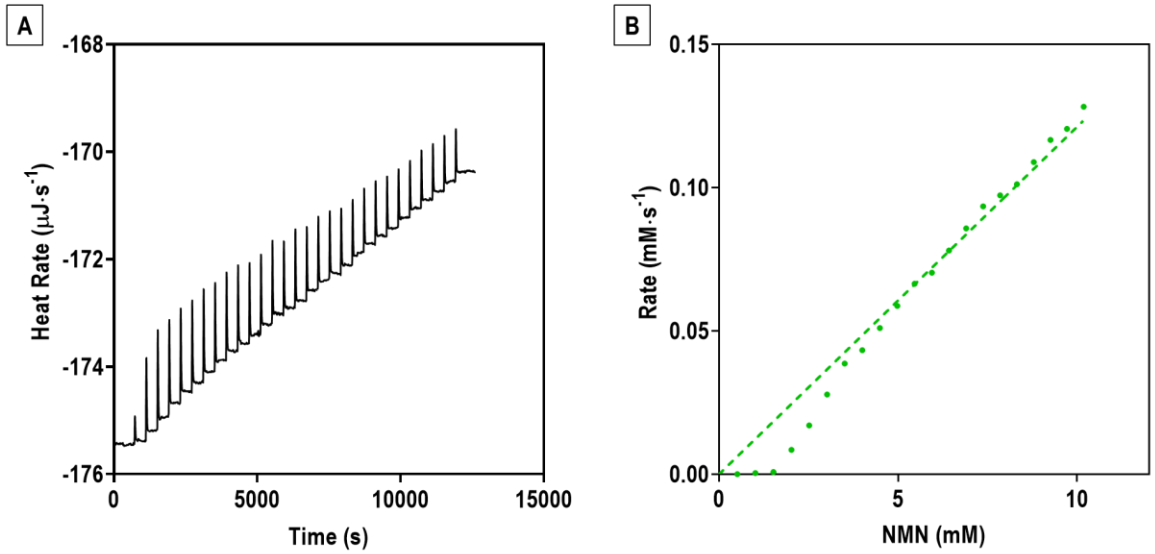

Figure S.2. Isothermal titration calorimetry for the determination of the kinetics of *Kp*NNAT. (A) A thermogram achieved from the multiple injection method of *Kp*NNAT in the absence of metal ion. (B) The resulting enzyme kinetics plot. It is supposed to resemble the Michaelis-Menten kinetics but instead shows a positive linear plot of the rate ($mM \cdot s^{-1}$) against substrate concentration (mM).

Inner filter effect (IFE)

The inner filter effect (IFE) is the reduction of fluorescence intensity due to the attenuation of emission beam or the reabsorption of the emitted light by the solution. The former is known as primary IFE and the latter is known as secondary IFE (Kumar Panigrahi and Kumar Mishra, 2019). The correction for IFE includes the dilution or reduction of the concentration of constituents in the solution, changing a cuvette or mathematical formulars (Kumar Panigrahi and Kumar Mishra, 2019; Mendonça *et al.*, 2013).

A UV-Scan of the ligands was performed with a Jasco V-630 (Jasco, UK). The spectrum was measured from 240-350 nm. The samples were IFE buffers which were buffer A [10 mM PBS, pH 7.2], buffer B [10 mM PBS, 5 mM $MgCl_2$, pH 7.2] and buffer C [10 mM PBS, 5 mM $NiCl_2$, pH 7.2]. The ligands that were used were 100 µM of ATP, and NMN. A concentration of 10 µM of protein was used. A total of 500 µL of samples were prepared according to Table S1.

Table S.1. Sample preparation for IFE

Sample 1	Sample 2	Sample 3	Sample 4	Sample 5
Buffer	Protein NMN	Protein ATP	NMM	ATP

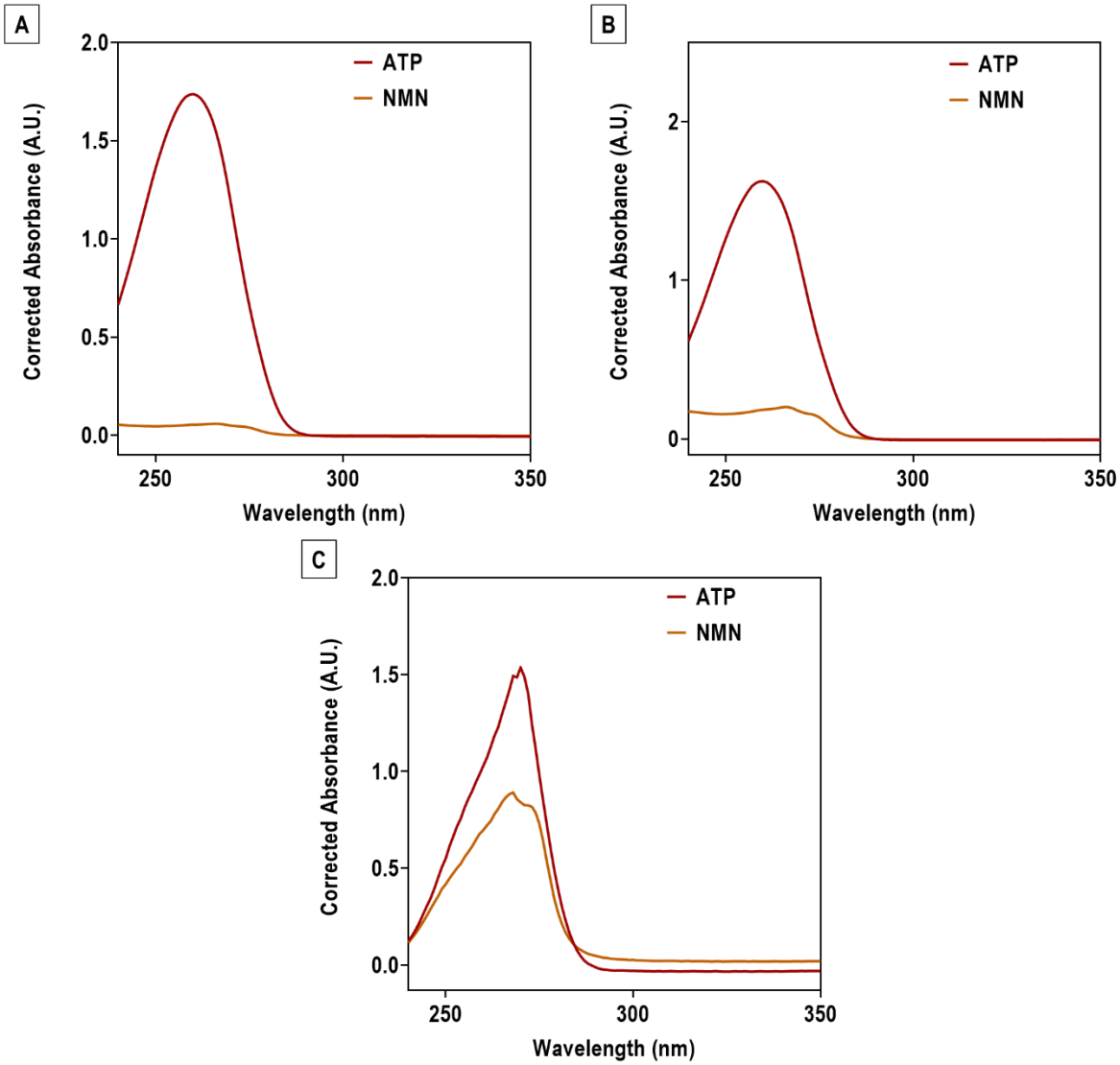

Figure S.3. UV absorbance spectra to monitor the inner filter effect of substrates ATP and NMN. The absorbance was measured from 240-350 nm. UV spectra in the absence of (A) metal ion, presence of (B) Mg^{2+}, or (C) Ni^{2+}.